RUPRECHT-KARLS-UNIVERSITÄT HEIDELBERG

Matthias C. Walter

Ultrastructural Characterization of Tissue Ablations by Laser with Multiphoton - Microscopy and Atomic - Force - Microscopy

Civil Service Examination / Staatsexamensarbeit

HD-KIP-03-04

KIRCHHOFF-INSTITUT FÜR PHYSIK

Ultrastructural Characterization of Tissue Ablations by Laser with Multiphoton - Microscopy and Atomic - Force - Microscopy

Civil Service Examination / Staatsexamen

vorgelegt von Matthias C. Walter

Betreuer :
Prof. Dr. J. Bille

30. Mai 2003

Kirchhoff - Institut für Physik
Ruprecht - Karls - Universität Heidelberg

Contents

CHAPTER 1

Introduction / Motivation

Sight is one of the most important senses for a human being. We rely heavily on this sense so every little defect has a big effect for our live. How far this goes can be seen at the saying "*To see is to believe*". So it is only natural to search for possibilities to repair this sense and even try to improve it. Figure 1.0.1 shows some of the possible aberrations in a human eye.

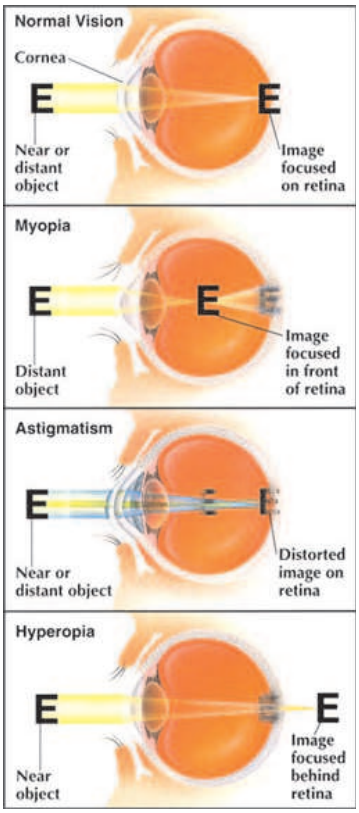

FIGURE 1.0.1. These diagrams show some of the most common differences between "normal" and defective eyes. **[23]**

Glasses were the first method to correct the vision but they have disadvantages. If the aberration of the eye is big the glasses are getting very heavy and thick. Also the field of view is defined by the size of the glasses and the correct position in front of the eye is not given all the time (heavy glasses start sliding down the back of the nose easily). The next evolutionary step were contact lenses in the 1940's. The field of view with this device is as big as it is for a "normal" eye. But as with the glasses there are some disadvantages. First of all is the problem with putting something into the eye, so the normal gas flow is disturbed and germs can be introduced to

the eye. Also the eye is deformed by the pressure exerted in the process of moving the eye lids.

So people started searching for other possibilities to correct the vision. Some methods were described as early as in 1869 but the results were not very encouraging. In 1973 Dr. Svyatoslav Fyodorov performed an operation now a days known as Radial Keratotomy (RK).

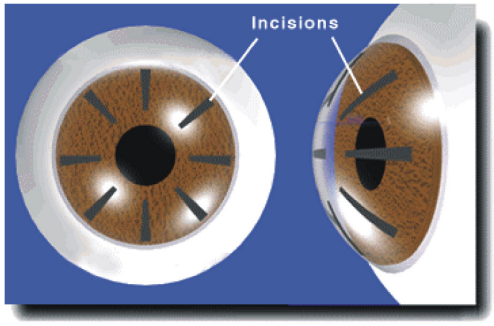

FIGURE 1.0.2. The picture shows where the incisions are placed performing Radial Keratotomy. [**23**]

The concept was simple: four to eight radial incisions with a scalpel were placed from the mid to the peripheral zone of the cornea, outside the line of vision (see figure 1.0.2). The cornea was flattened by these incisions and so it was possible to correct mild to moderate amounts of nearsightedness and astigmatism. With the introduction of the laser as a surgical tool better methods were developed. In 1976 IBM developed the excimer laser. It was used at first to etch intricate patterns on computer chips. The excimer laser is often described as a "cold" laser because its ultraviolet radiation breaks molecular bonds without producing heat that could damage the surroundings. This is one important thing for its surgical use. Another is the possibility to control the ablation depth and size very precisely. With this tool a new operation form called Photorefractive Keratectomy (PRK) was born (figure 1.0.3).

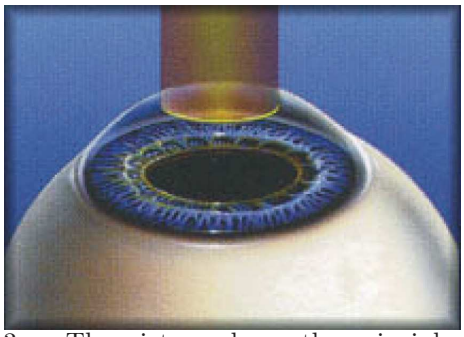

FIGURE 1.0.3. The picture shows the principle way of Photorefractive Keratectomy. An excimer laser is used to ablate the corneal tissue from the top.[**23**]

The principle is to gather information about the eye with preoperative measurements first. This data is then entered into a computer which calculates the

sculpting pattern and guides the laser. The excimer laser starts from the top of the cornea and removes tissue due to the sculpting pattern. (Figure 1.0.4 shows a picture of such a laser system).

FIGURE 1.0.4. Visx Laser System which uses an excimer laser.[**23**]

The next evolutionary step was the Laser In-Situ Keratomileusis (LASIK). The surgeon starts by creating a flap (thickness about 160 μm) of the cornea with a microkeratome. The flap remains attached to the cornea via a small hinge. In the next step the flap is opened and an excimer laser is used to sculpt the internal of the cornea to the desired shape. Then the flap is carefully placed back on its former place (figure 1.0.5). The advantage of this method is that the upper cornea layers (see chapter 2 for more information) are not disturbed as much as with PRK.

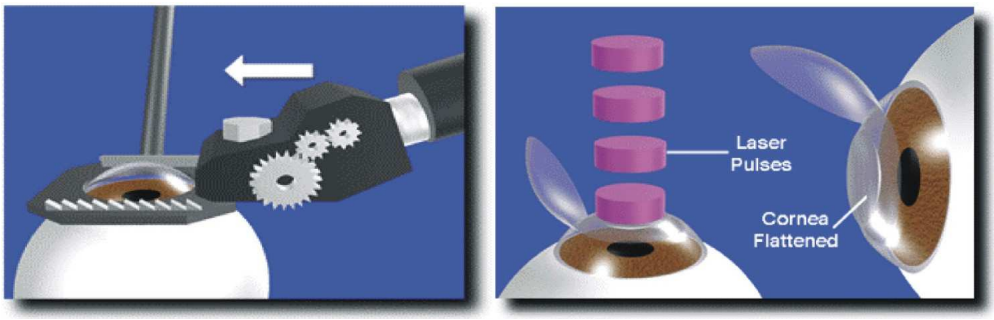

FIGURE 1.0.5. Laser In-Situ Keratomileusis. By mechanical means a flap is created. Then an excimer laser is used to sculpt the flap bed in that way that the refractive change which was determined prior to the operation is achieved.[**23**]

The newest method, Femtosecond Laser Intrastromal Vision Correction (FLIVC), is a form of LASIK.

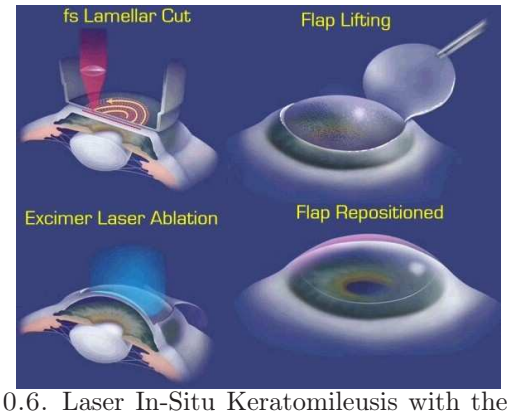

FIGURE 1.0.6. Laser In-Situ Keratomileusis with the use of a fs infrared laser to create the flap. The fs laser is first scanned in a planar fashion at a constant depth (between 160 and 200 microns) to create a lamellar cut. Side cuts are made to the surface to allow the flap to be lifted. After reflecting the flap back, the stromal bed is ablated to a new shape with an excimer laser. The flap is then repositioned. [**47**]

The flap is cut by a laser which results in even smaller damage to the tissue layers of the cornea. The rest is the same as in the LASIK process with one difference. The laser that cuts the flap is not an excimer laser but a Nd:Glass laser which emits radiation in fs-pulses and in the near infrared so that they can penetrate the cornea. (figure 1.0.6) The tissue – laser interaction is another than that of the excimer laser and is described later in this work.

The next step may be the following: With the fs-laser an intrastromal cut is applied to create a lenticule that is removed and by this way the change in the topography of the cornea is achieved. (figures 1.0.7 and 1.0.8)

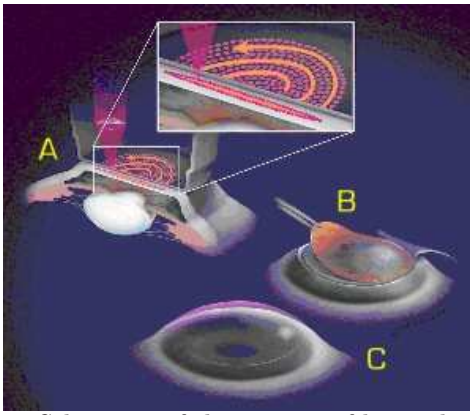

FIGURE 1.0.7. Schematic of the process of lenticule cutting . (A) A lenticule is cut inside the cornea, defining the lenticule posterior surface. A second cut is made to define the anterior surface of the lenticule. This cut may be integrated with a flap cut to allow access. (B) After the flap is lifted, the lenticule is removed with handinsturments. (C) Finally, the flap is replaced, resulting in a direct refractive change. [**46**]

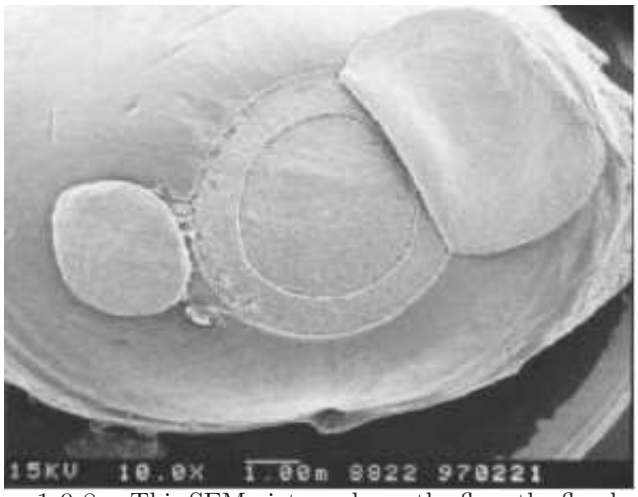

FIGURE 1.0.8. This SEM picture shows the flap, the flap bed and (on the left side of the surface of the cornea) the removed lenticule. [**46**]

Another possible approach will be to try and do the sculpting of the cornea by means of intrastromal cutting without opening a flap or cutting a lenticule. (figure 1.0.9)

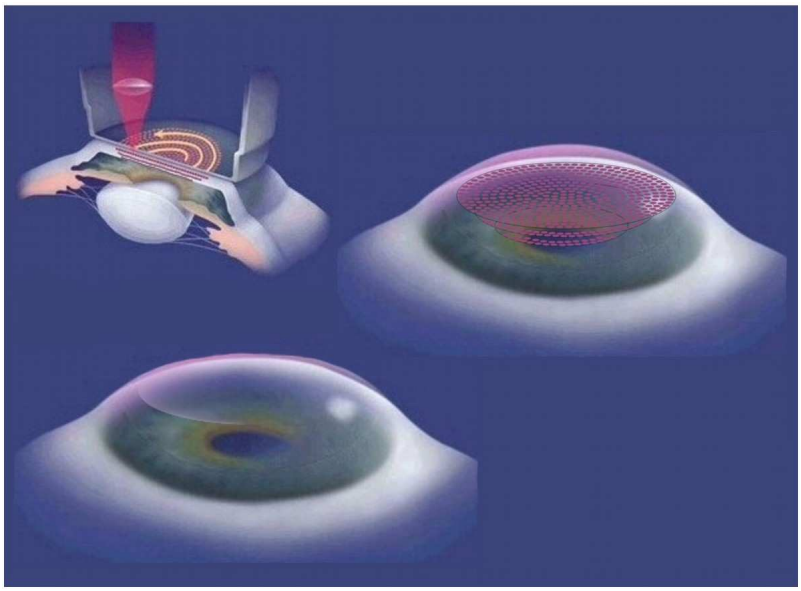

FIGURE 1.0.9. Schematic of a intrastromal cut. At different depth (beginning with the greatest depth and smallest spiral pattern) a spiral pattern is "burned" into the cornea. After some time the cavities produced by the laser will collapse and the cornea will become clear again. The refractive change is then due to amount of ablated tissue.

The refractive change is due to the ablation of the tissue by the fs laser.

Because this is a new way of treatment the main part in this work was to find preparation methods and ways to measure the samples with the different microscopes for evaluation of the laser treatment. Also the possibility of second harmonic generation is long known, the use for microscopy is a new branch in research so we had very few sources of information about this available. The same applies even more for the *A*tomic *F*orce *M*icroscope (AFM). AFM measurements were performed only on the outer side or on inner surfaces revealed by excimer laser treatment of the cornea until now. So we had to find ways to make our intrastromal cuts accessible to the AFM. This work emphasizes more the methodical part than the evaluation of the laser treatment method.

CHAPTER 2

The Human Eye

As written before in chapter one the eyes play a major role in the live of a human being. Some properties of the structure of the human eye that are of interest for this work will be discussed now.

2.1. Structural Constitution of the Eye

In general the eye is approximately a sphere with a diameter of 2.5 cm and a volume of about 6.5 ml [in reality the eye consists of two spheres, a smaller one anteriorly, the cornea which has a greater curvature than the sclera which constitutes a larger sphere]. The cornea forms one sixth of the circumference of the eye globe and has a radius of 7.8 mm, the remaining $\frac{5}{6}$ of the eye is formed by the sclera which has a radius of 11.5 mm. The size varies between individuals but the average axial length of the eye is 24 mm (it ranges from 21 to 26 mm). [**42**]

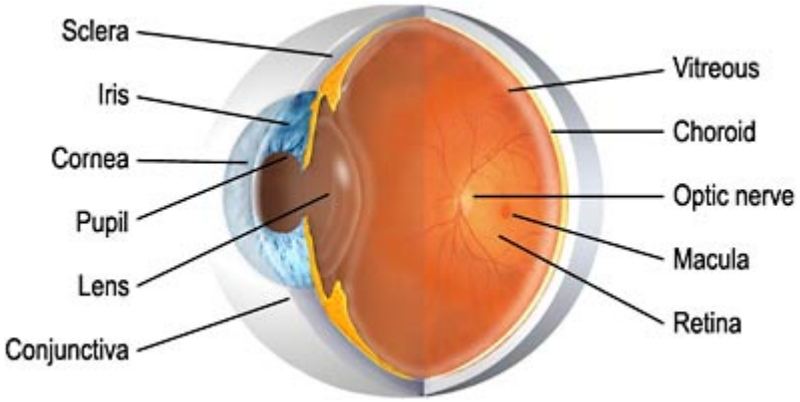

FIGURE 2.1.1. Cross section of the human eye with labels for the different components that constitute an eye. [**10**]

Figure 2.1.1 shows a cross section of a human eye. An eye can be made up of three basic layers or coats and three spaces. The three spaces are the anterior and the posterior chamber of the eye which are filled with liquid and the third space which is filled with the vitreous body. The layers can be discerned in [**42**]

- the fibrous (corneo - scleral) coat
- the uvea or uveal tract - composed of choroid, ciliary body and iris
- the neural layer (retina)

From these components the cornea is of the most interest because it contributes between 65 - 75 percent of the total focusing power of the eye and it is easy to access. The focusing power is caused by the difference in refractive indices between air ($n \simeq 1$) and the corneal tissue ($n = 1.376$). This results in a refraction power of about +43 diopters given by summing up the effects of the front surface of the cornea which works as a convex lens and the back surface which works a concave

lens. So by changing the form of the cornea it is possible to correct the refractive index of the eye very efficiently.

2.2. Structure of the Cornea

The cornea is the eye's outermost layer. It is the clear, dome-shaped surface that covers the front of the eye. Like a watch crystal that protects the inner parts of the watch, the cornea protects the interior of the eye. (figure 2.2.1)

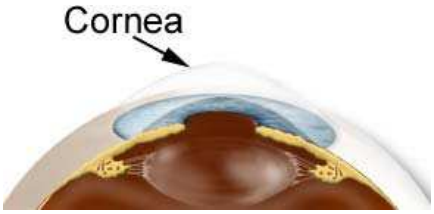

FIGURE 2.2.1. Picture of the position of the cornea. [**10**]

The cornea has 5 layers (listed outside to inside) [**42**]:

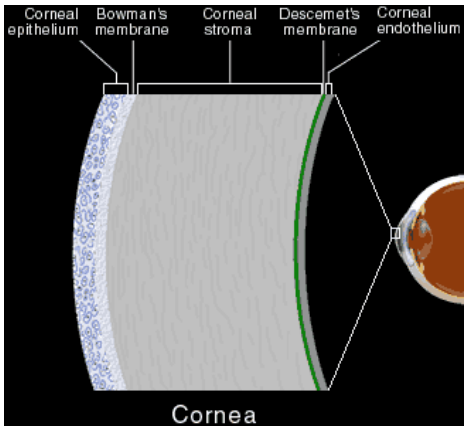

FIGURE 2.2.2. Schematic of the setup of the human cornea tissue. [**11**]

(1) The **Epithelium** is a stratified (5-6 layers), squamous non-keratinised epithelium (the superficial cells are flattened, nucleated and non-keratinised). It is 50-60 μm in thickness and adjacent cells are held together by numerous desmosomes and to the underlying basal lamina by hemidesmosomes and anchoring filaments. The anterior surface of the corneal epithelium is characterized by numerous microvilli and microplicae (ridges) whose glycocalyx coat interacts with, and helps stabilize, the precorneal tear film. New cells are derived from mitotic activity in the limbal basal cell layer and these displace existing cells both superficially and centripetally. The corneal epithelium responds very rapidly to repair disruptions in its integrity by amoeboid sliding movements of cells on the wound margin followed by cell replication. The basal epithelial cells rest upon a thin, but prominent basal lamina (lamina lucida, 25 nm; lamina densa, 50 nm). Corneal epithelial adhesion is maintained by a basement membrane complex which anchors the epithelium to Bowman's layer via a complex mesh of anchoring fibrils (type VII collagen) and anchoring plaques (type VI

collagen) which interact with the lamina densa and the collagen fibrils of Bowman's layer. Central corneal epithelium is effectively devoid of melanocytes and immunocompetent cells including MHC class II-bearing dendritic cells (Langerhans cells). The absence of the latter cell type and the avascular nature of the cornea are of crucial importance to the success of corneal grafting.

(2) **Bowman's layer** : (a modified acellular region of the stroma) (8-12 μm thick) consists of fine, randomly arranged collagen fibrils (20-30 nm diameter, types I, III, V and VI). The anterior surface is well delineated and is separated from the epithelium by the thin basal lamina, whilst the posterior boundary merges with the stroma. It terminates abruptly at the limbus.

(3) The **corneal stroma** is a dense connective tissue of remarkable regularity. It makes up the vast majority of the cornea and consists predominantly of 2 μm thick flattened collagenous lamellae (200-250 layers) orientated parallel to the corneal surface and continuous with the sclera at the limbus. Between the lamellae lie extremely flattened, modified fibroblasts known as keratocytes. These cells are stellate in shape with thin cytoplasmic extensions containing conspicuously few distinctive organelles. The collagenous lamellae form a highly organized orthogonal ply, adjacent lamellae being orientated at right angles (see figure 2.2.3), with the exception of the anterior third in which the lamellae display a more oblique orientation (see figure 2.2.4).
The collagen fibers are predominantly of Type I (30 nm diameter, 64-70 nm banding) with some type III, V and VI. The transparency of the cornea is highly dependent upon the regular spacing of the collagen fibers (interfibrillary distance) which in turn is regulated by glycosaminoglycans (GAG) and proteoglycans forming bridges between the collagen fibrils. The GAGs in the human cornea are predominantly keratan sulphate and chondroitin (dermatan) sulphates. The corneal stroma normally contains no blood or lymphatic vessels but sensory nerve fibers are present in the anterior layers 'en route' to the epithelium.

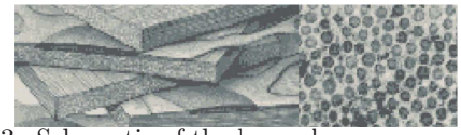

FIGURE 2.2.3. Schematic of the layered arrangement of the collagen lamellae in the stroma. [**1**]

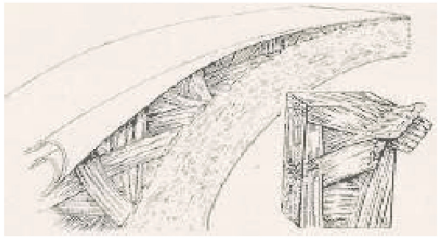

FIGURE 2.2.4. Schematic drawing of the arrangement of the collagen fibrils in the anterior third of the stroma. [**1**]

(4) **Descemet's Membrane**: This is a thin, homogeneous, discrete, PAS-positive layer between the posterior stroma and the endothelium, from which it can become detached. It is 8-12 μm in thickness and represents the modified basement membrane of the corneal endothelium. It consists of two parts, an anterior third which is banded and homogeneous or non-banded posterior two-thirds.
It is rich in basement membrane glycoproteins, laminin and type IV collagen. The anterior banded region is reported to contain type VIII collagen. Types V and VI collagen may be involved in maintaining adherence at the interface of Descemet's membrane with the most posterior lamellae of the stroma.
Descemet's membrane is continuous peripherally with the cortical zone of the trabeculae in the trabecular meshwork. Microscopic wart-like protuberances (Hassal-Henle bodies or peripheral guttatae) containing 'long banded (100 nm)' deposits of unknown nature appear in the periphery of Descemet's membrane with age. It is frequently thickened at its peripheral termination (Schwalbe's line at the anterior limit of the trabecular meshwork). If disrupted the Descemet's membrane tends to curl inwards towards the anterior chamber.

(5) **Corneal Endothelium**: Fluid is constantly being lost via evaporation at the ocular surface, a fact illustrated by increased corneal thickness after a night of lid closure and if an impermeable lens is placed over the epithelium.
The corneal endothelium, a simple squamous epithelium on the posterior surface of the cornea, has a critical role in maintaining corneal hydration and thus transparency. The endothelial cells rest upon Descemet's membrane and form a regular uninterrupted polygonal or hexagonal array or mosaic which can be clearly seen in vivo with the aid of specular microscopy, which is also used to assess cell density (see below). The cells are 5-6 μm in height and 18-20 μm in diameter (250 μm surface area). Their lateral surfaces are highly interdigitated and possess apical junctional complexes which together with the cytoplasmic organelles such as very large numbers of mitochondria, are indicative of their crucial role in active fluid transport.
The endothelium in the normal human cornea has low regenerative capacity and lost cells are quickly replaced by spreading of adjacent cells. There are approximately 350000 cells per cornea (approximately 3000-4000 cells/mm^2 at birth, falling to 2500/mm^2 in mid-age and 2000/mm^2 in old age. Consequently, with age the dense regular hexagonal arrangement typical of young corneas is replaced by fewer cells of more heterogeneous sizes and shapes. Damage to corneal endothelial cells and densities of below 800/mm^2 leads rapidly to oedema and swelling of the stroma with resultant loss of transparency. A density of below 1500/mm^2 is considered too low for consideration for corneal transplantation.

After these informations it should have become clear why any damage to the cornea should be reduced to the absolute minimum. So the intrastromal surgery without flap-cutting would be a big step in this direction.

2.3. Collagen

Collagen is the major structural protein in the human body. About one quarter of all the protein in the human body is collagen. It is nearly everywhere and it is a relatively simple molecule. There are many different types of collagen which

perform different duties in the body. Some collagen forms molecular cables to strengthen the tendons or vast, resilient sheets that support the skin and internal organs. Even the bones and teeth are made of collagen by adding mineral crystals. So one can say that collagen provides the shape for our body.

The structure of collagen is, as mentioned before, not very complicated. Collagen is composed of three chains that are wound together in a tight triple helix (see figure 2.3.1).

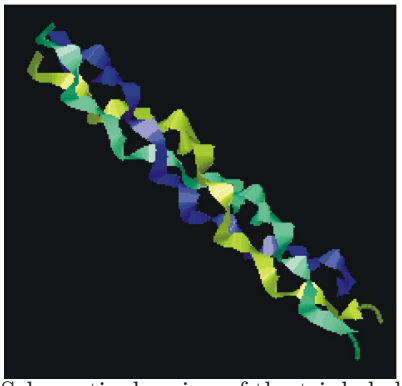

FIGURE 2.3.1. Schematic drawing of the triple helical structure of collagen **[3]**

A repeated sequence of three amino acids is the base for the collagen structure. Every third amino acid is glycine, a small amino acid that fits perfectly inside the helix. Many of the remaining positions in the chain are filled by two other amino acids : proline and hydroxyproline. The following figure shows the chemical structure of the three main amino acids in collagen. (figure 2.3.2)

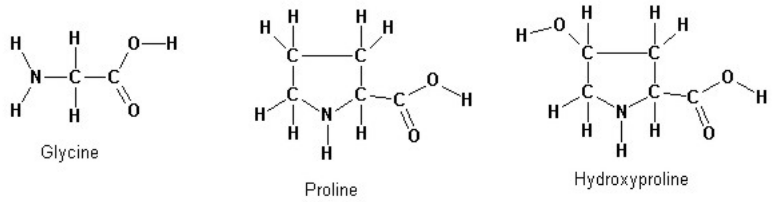

FIGURE 2.3.2. Chemical structures of Glycine, Proline and Hydroxyproline (pictures in this order)

In figure 2.3.3 you can see a small cutout of the chains with labels for the different amino acids.

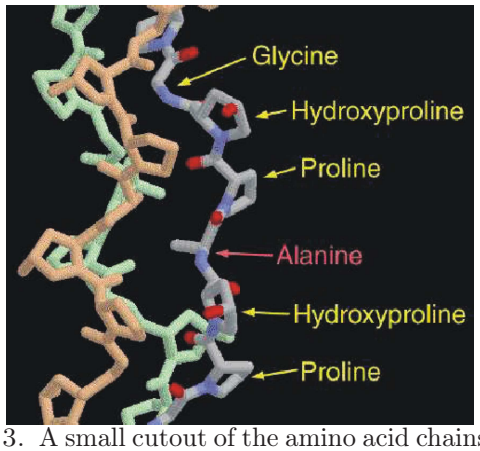

FIGURE 2.3.3. A small cutout of the amino acid chains which form collagen fibers. The main amino acids that make up the collagen molecule are labeled. [**2**]

In figure 2.3.4 a stick model and a sphere model can be seen. Collagen is

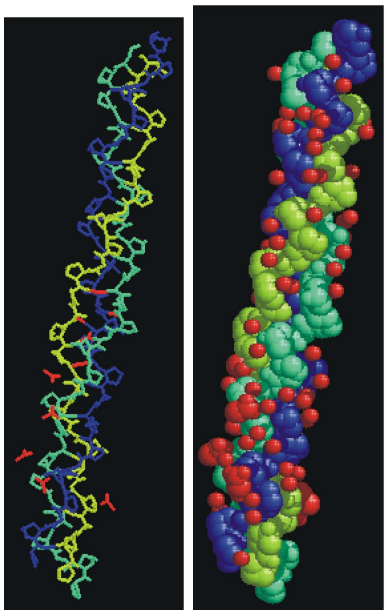

FIGURE 2.3.4. Structure of the collagen molecular chain (Stick-Model) [left picture] and the same molecule shown as a sphere model [right picture]. [**3**]

reported to show native autofluorescence at 390 nm.

There is also another property of collagen: it is able to generate second harmonics (*S*econd *H*armonic *G*eneration : SHG). This will be described in more detail in chapter 4. For now we will just say that it is a result of the non-centrosymmetric build up of the collagen fibrils (see Figure 2.3.5).

Table 1 shows some details about the different types of collagen. In the human eye there can be found 7 different types. These types are **I**, **III**, **IV**, **V**, **VI**, **VII**, **VIII**. For the most part it is type **I** collagen that can be found in the eye and especially in the cornea.

Types	Chains	Molecular Structure	Supermolecular Structure	Localization
I	$[\alpha 1\,(\mathbf{I})]_2\ [\alpha 2\,(\mathbf{I})]$	$300nm$	$67nm$ banded fibrils	skin, tendon, bone, etc.
II	$[\alpha 1\,(\mathbf{II})]_3$	$300nm$	small $67nm$ fibrils	cartilage, vitreous humor
III	$[\alpha 1\,(\mathbf{III})]_3$	$300nm$	small $67nm$ fibrils	skin, muscle frequently with type **I**
IV	$[\alpha 1\,(\mathbf{IV})]_2\ [\alpha 2\,(\mathbf{IV})]$	$390nm$, C-term. globular domain	Nonfibrillar network	all basal lamina
V	$[\alpha 1\,(\mathbf{V})][\alpha 2\,(\mathbf{V})][\alpha 3\,(\mathbf{V})]$	$390nm$, N-term. globular domain	small fibers	most interstitial tissue, assoc. with type **I**
VI	$[\alpha 1\,(\mathbf{VI})][\alpha 2\,(\mathbf{VI})][\alpha 3\,(\mathbf{VI})]$	$150nm$, N+C-term. globular domain	Microfibrils, $100nm$ banded fibrils	most interstitial tissue, assoc. with type **I**
VII	$[\alpha 1\,(\mathbf{VII})]_3$	$450nm$	Dimer	epithelia
VIII	$[\alpha 1\,(\mathbf{VIII})]_3$	?	?	some endothelial cells
IX	$[\alpha 1\,(\mathbf{IX})][\alpha 2\,(\mathbf{IX})][\alpha 3\,(\mathbf{IX})]$	$200nm$, N-term. globular domain	bound proteoglycan	cartilage, assoc. with type **II**
X	$[\alpha 1\,(\mathbf{X})]_3$	$150nm$, C-term. globular domain	?	hypertrophic and mineralizing cartilage
XI	$[\alpha 1\,(\mathbf{XI})][\alpha 2\,(\mathbf{XI})][\alpha 3\,(\mathbf{XI})]$	$300nm$	small fibers	cartilage
XII	$[\alpha 1\,(\mathbf{XII})]_3$	?	?	interacts with types **I** and **II**

TABLE 1. A list of the different types of collagen and their respective localization in the human body. **[34, 36]**

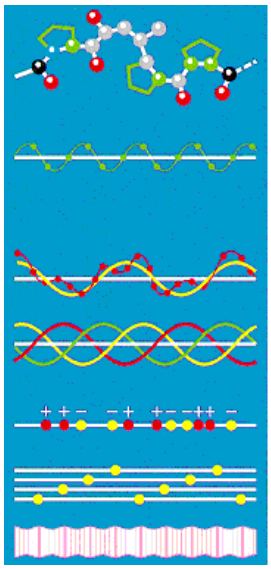

FIGURE 2.3.5. Schematic of the collagen structure. Starting at the top with the molecular structure and ending in a schematic drawing of a collagen fibril how it can be seen in electron microscope pictures.

2.4. Gelatin

Because of the limited resources of high quality porcine corneas we were looking for a possible substitute. We thought we found one in gelatin. Gelatin consists mostly of collagen type I so it should exhibit similar properties as the collagen in the cornea. The figure 2.4.1 shows the manufacturing process of gelatin from the raw materials.

As can be seen in figure 2.4.1 the collagen is treated with alkaline or acid to yield a product that is solvable in warm water. Because of this treatment the original helical structure is only partially regained after cooling down (see figure 2.4.2). The amount of fibers that regain their nearly original structure can be influenced by the type of gelatin that is used as well as by the conditions in the cool down process.

To get as many fibers in their original state as possible the cool down conditions were set as follows: A negative temperature gradient with about 3 degrees centigrade per hour was used and the starting point was 37 degrees centigrade and the cool down process was also performed under humidified conditions.

The gelatine was dissolved in a beaker with distilled water in a water bath at about 40 degrees centigrade in that way that the concentration of gelatin was about 30%. To yield a solution without air bubbles, which appear because of stirring the gelatin/water mixture while the gelatin is melting, the beaker was left in the water bath for about 24 hours at 40 degrees centigrade. After that the now clear solution was poured on a glass plate covered with a plastic foil, which helped to remove the gelatin film more easily later on and with a special spatula the gelatin was formed to a band that was about 6.5 cm broad and 0.5 mm thick. Thereafter these bands were cooled down under the conditions written above, dried and removed from the plastic foil. Small samples were cut from these bands for further experiments. For the later use they have to be re-hydrated so that they have a water content of about 80%, which is nearly the same as that of the human cornea. We tried to image such pieces in the same way as we did with the corneas but no SHG seemed to occur.

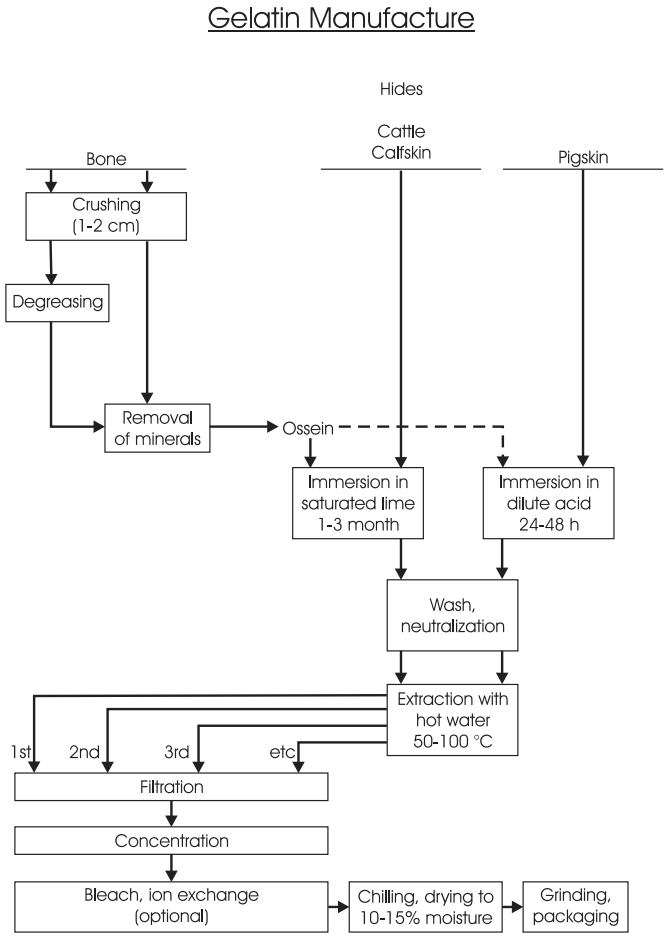

FIGURE 2.4.1. Diagram of the production process of gelatin

An autofluorescence signal was detectable. The lack of a detectable SHG may have three causes:

- The microscope setup was not able to detect a signal because it was to weak. A more sensitive setup may have a chance to get an image.
- As a result of the manufacturing process most of the fibers internal bonds are broken and the length of the helical parts is reduced to render a soluble product. So even with the conditions written above which were specially designed to maximize the size of the helical structures we were not able to regain enough of the original structure to generate second harmonic signals.
- Because of the random order of the helical parts the SH signal, which is a coherent signal, is not enhanced by constructive interference.

Because of this "negative" result we were now able to use gelatin as a coating material for microscope slides on which we could put sectioned corneas. We should than be able to use these microscope slides for both microscopes the AFM and the LSM. By putting the slides with the adhering cornea sections into PFA or Glutaraldehyde we could also limit the growth of the gelatin, which was due to incorporation of water while measuring in PBS.

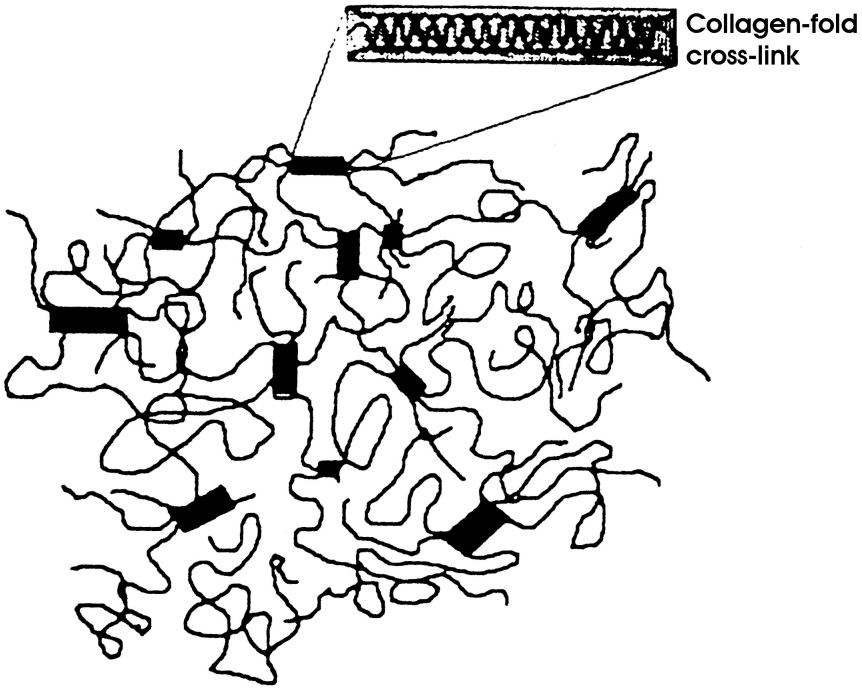

FIGURE 2.4.2. Collagen-fold aggregates forming gel-network junctions in a gelatin gel

CHAPTER 3

Microscopes

In the following sections the microscopes which were used and their technical details are documented.

3.1. Light Microscopes

The light microscopes are located at the Max Planck Institute for medical research in Heidelberg and were used by the courtesy of Prof. Dr. Denk and Dr. Giese. Two different microscopes were available for usage there. A confocal microscope and a multiphoton microscope.
Most of the time we put the samples upside down in a chamber filled with PBS. The chamber had a glass bottom with a thickness of $1\,mm$, which was optimal for the oil condenser of the multiphoton microscope. By choosing the upside down orientation of the sample we wanted to minimize the number of changes in refractive indices. In the schematic picture in figure 3.1.1 it should become clear why we chose this orientation.

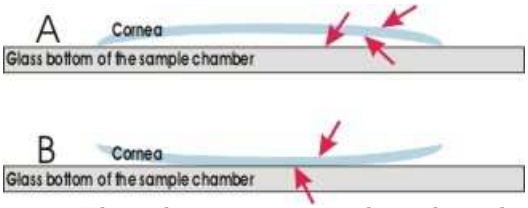

FIGURE 3.1.1. This schematic picture shows how the change in orientation affects the number of refractive index changes. The different surfaces are marked with arrows. The surfaces between dipping lens – PBS and chamber bottom – condenser are not taken into account because these interfaces can not be avoided. (The PBS is not shown in the picture with color)

The interfaces in picture A in figure 3.1.1 could be reduced by applying force to the cornea to flatten it but by doing this also stress induced delocalization of the collagen fibers could occur. So the orientation that is shown in picture B in figure 3.1.1 is used for the measurements. The method of fixating the samples in the microscope chamber depended on thickness of the samples. For the flap samples some pieces of platinum wire, which were bend, were enough to keep it from floating around. The thicker samples were weighted down by using a washer of appropriate size and weight. We always tried to use as little weight as possible. The wires and the washers also gave us a good point to focus at for a starting point in the search of the surface of the sample.

3.1.1. Leica TCS SP2 confocal microscope. Equipped with:

- Ar UVLaser (532, 364 nm)
- Ar Laser (457, 467, 488, 514 nm)
- HeNe Laser (543 nm)
- HeNe Laser (633 nm)
- Acousto Optical Beam Splitter (AOBS) as main beam splitter for free selection of and rapid switching between reflected / transmitted wavelengths
- Spectral windows / filters for any fluorochrome (blue to dark red fluorescence) and different Green Fluorescent Protein Variants (CFP,GFP,YFP and dsRed)
- 4 PMT's (epifluorescence and reflection mode)]
- One PMT (transmission mode)
- Software for sequential / simultaneous / time lapse / spectral recording / and for photobleaching experiments

The Leica microscope was used to make some confocal pictures of the cornea.

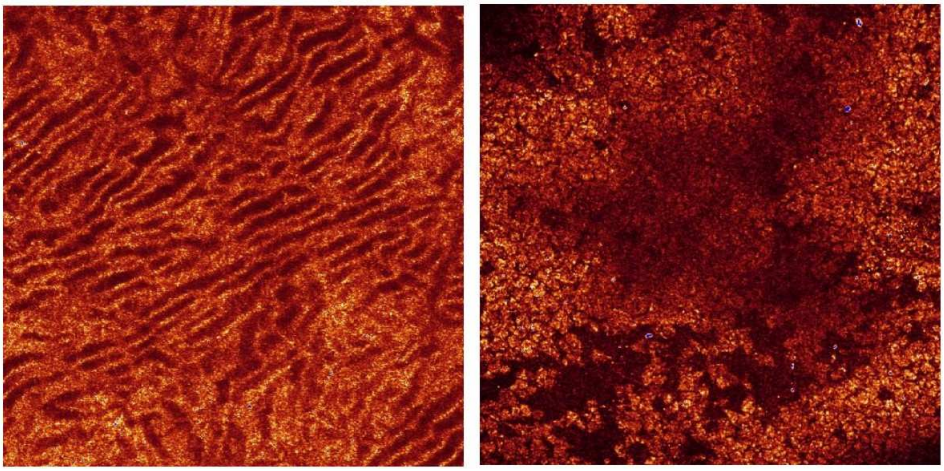

FIGURE 3.1.2. Images of an unprocessed cornea. The left picture shows the stroma and the right one the epithelium of the cornea. As can be seen in the right picture the confocal microscope shows not the collagen fibrils. So it can not be used to evaluate the laser treatment.

We also used it to make images of materials that did not generate second harmonic signals. The Leica microscope was used because we experienced some problems when we tried to make confocal pictures with the Zeiss microscope because the Zeiss microscope is optimized for multiphoton microscopy. In figure 3.1.3 a diagram of the build up of a confocal microscope can be seen.

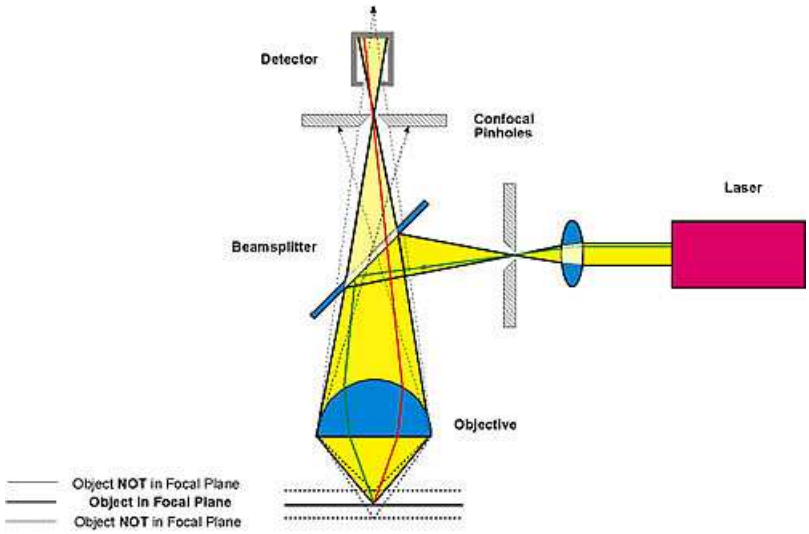

FIGURE 3.1.3. Diagram of the Leica confocal microscope [**43**]

3.1.2. Zeiss LSM 510 NLO multiphoton confocal microscope. Equipped with:

- Coherent Verdi V8 / Mira Laser (fs pulses in the red to infrared range) ; after upgrade : Coherent Chameleon Laser
- Ar Laser (457,476,488,514 nm)
- HeNe Lasers (543 and 633 nm)
- Filter sets for common fluorochromes (cyan to dark red fluorescence) and different Green Fluorescent Protein Variants (CFP,GFP,YFP and dsRed)
- 3 PMT's (epifluorescence and reflection mode)
- 2 sets of non-descanned detectors (NDD's) for epifluorescence and transmission fluorescence mode
- Software for sequential / simultaneous / time lapse recording / and for photobleaching experiments

This microscope was used for second harmonics pictures of the collagen fibers in the corneas and *D*ifferential *I*nterference *C*ontrast images (DIC). The generation of a second harmonics signal is, as said before, a special ability of collagen because of it's non - centrosymmetric structure. Another point for using SHG is that the wavelength of the emitted light, the second harmonic, determines the resolution of the microscope. Gauderon and Sheppard [**21**] calculated the imaging properties of a weak object in scanned SHG microscopy. They showed that SHG microscopy should exhibit a degree of "super-resolution". The resolution will not be as good as that of a microscope operated at the harmonic frequency but superior to that of a similar microscope operating at the fundamental frequency. A schematic of the microscope can be seen in figure 3.1.4. The other diagram (figure 3.1.5) shows the optical path of the Zeiss microscope scanning unit.

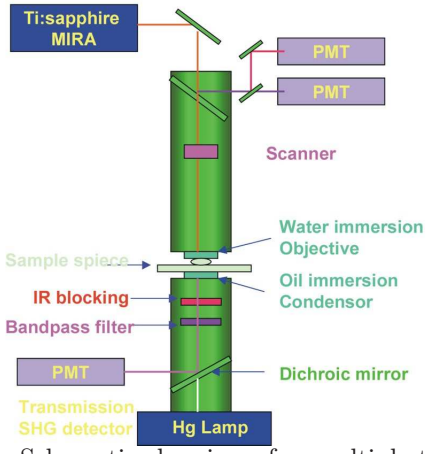

FIGURE 3.1.4. Schematic drawing of a multiphoton microscope used for SH imaging [**23**]

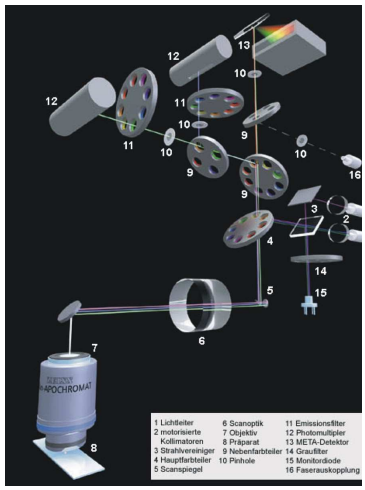

FIGURE 3.1.5. Diagram of the optical path in the scanning unit[**54**]

3.2. Atomic Force Microscope

- Digital Instruments MultiMode^{TM} SPM
- NanoScope^{R} IV Controller
- NanoScope^{R} Optical Viewing System
- Scanner 5176E
- FluidCell

The figure 3.2.1 shows a picture of an AFM like the one that was used.

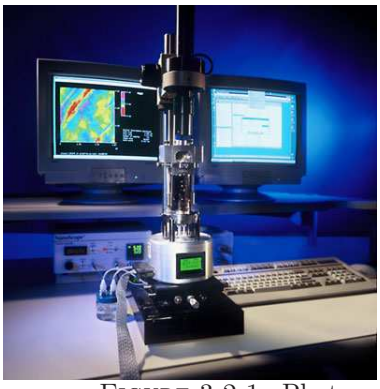

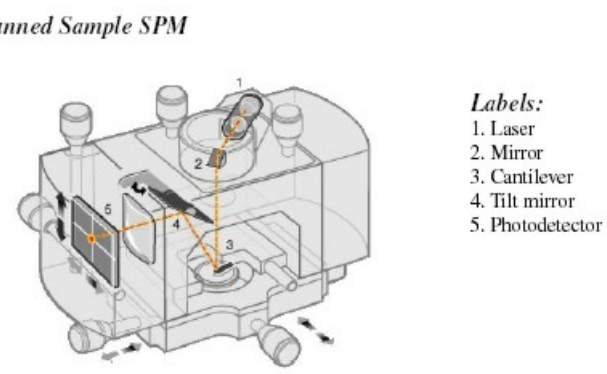

FIGURE 3.2.1. Photography of an AFM [**28**] and schematic of the scanning head with the laser beam path of the MultiMode AFM [**30**]

The Tapping mode was used for measurements because it reduced the forces on the sample to a minimum. How tapping mode works is shown in figure 3.2.2.

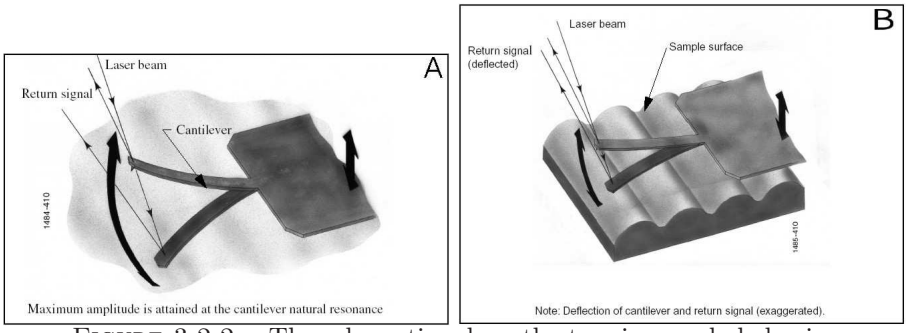

FIGURE 3.2.2. The schematics show the tapping-mode behavior of the cantilever and the laser beam in air away from the sample surface (A) and near sample surface (B). Because of the forces (attractive or repulsive depending on the distance to the sample surface and the sample material) in the neighborhood of the sample surface the amplitude of the oscillation of the cantilever is dampened. The hardware moves the tip over the surface of the sample and changes the z-position to hold the amplitude at a constant value. These z-position changes are monitored and give the height picture of the AFM. [**27**]

For our pictures we used not only the height picture produced by the AFM but also the so called phase picture. The phase picture shows the phase difference between the excitation oscillation and the detected oscillation of the cantilever. By this it is possible to distinguish between materials even if they do not show up in the height picture. Because the phase lag is due to properties of the sample that control the interaction between the sample surface and the tip of the cantilever, such as adhesion, friction, viscoelasticity and others. So an even higher resolution image of the sample is possible.

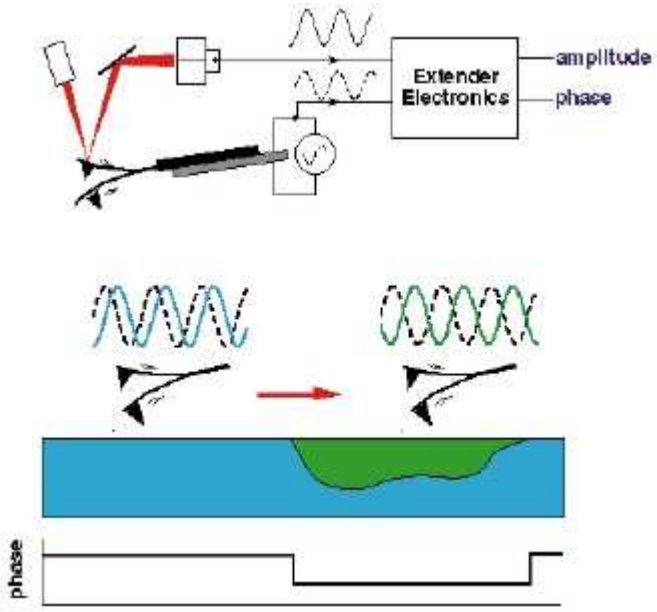

FIGURE 3.2.3. This schematic shows how the phase imaging works. The lag of the phase between excitation oscillation and detected oscillation is due to interaction forces between the material surface and the cantilever tip. Those interaction forces are specific for different materials. So it is possible to distinguish between two materials even if they do not show up in the amplitude (height) picture. [**29**]

3.3. Testing the Theory

To test if the theory can be proofed with this microscope setup Mr. Leander Zickler performed some experiments. For some of these the laser was tuned to $808\,nm$ because a $\frac{\lambda}{2}$ waveplate for this wavelength was available. At first the linearity of the *A*cousto–*O*ptic–*M*odulator (AOM) was checked. The average power was measured with a power meter directly after the AOM and after passing through the scanning unit of the Zeiss microscope. To measure the beam that passed the scanner the microscope objective was removed and the scanner was set to a frame size of 512x512 points at a scan speed of 8 and a digital zoom of 40x. The scan was performed unidirectional. As can be seen in the figure 3.3.1 the AOM setting corresponds linearly to the chosen percentage. The next measurement was to verify the intensity correlation between the incident beam and the SH light produced. For this a cornea sample was imaged, the colors were converted to a 256 gray-scale picture and the mean of the resulting values for the pixels was calculated. In figure 3.3.2 can be seen that the SH intensity has a square dependence to the incident laser beam as is predicted by theory. To verify the polarization dependence of the SH signal Mr. Zickler first tested the dependence of the power after passage through the scanner from the polarization of the laser beam. The polarization plane was rotated by the $\frac{\lambda}{2}$ waveplate. As can be seen in figure 3.3.3 the power dependence is about 10% due to the differences in reflectivity of the mirror coatings in the scanner. Figure 3.3.4 shows the measurement of the polarization dependence of the SH signal. The values were obtained in similar fashion as before. The result is that the SH signal is highly dependent on the polarization orientation that was also predicted by the theory.

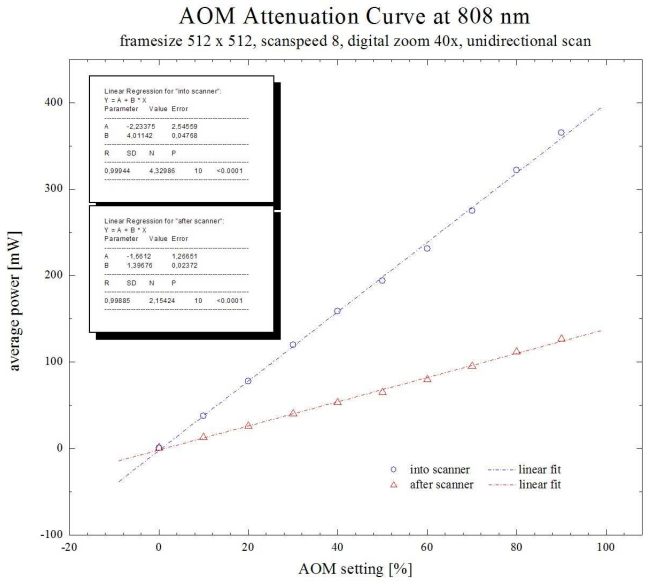

FIGURE 3.3.1. This graph shows the linearity of the AOM crystal and the software settings.

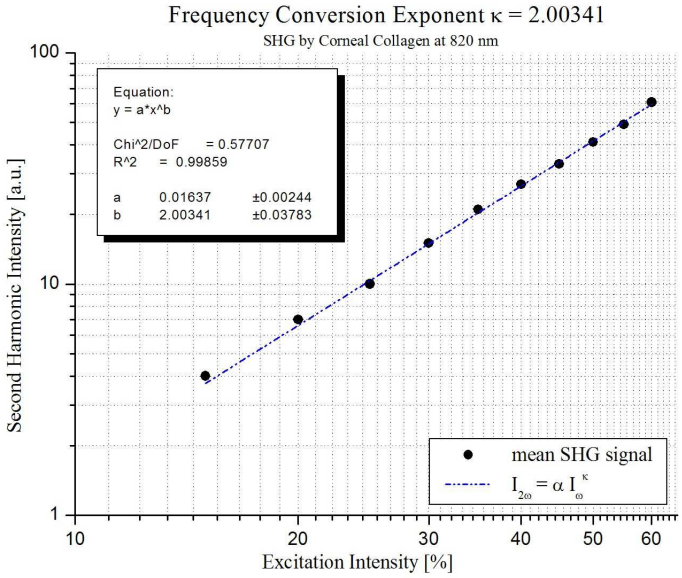

FIGURE 3.3.2. This graph shows the intensity dependence between the incident beam and the produced second harmonic light. The fit value is in good agreement with the theoretical value. The scales are logarithmic.

These test showed that all the effects predicted by theory can be reproduced with this microscope and they are also proofs that we are dealing with second harmonic light.

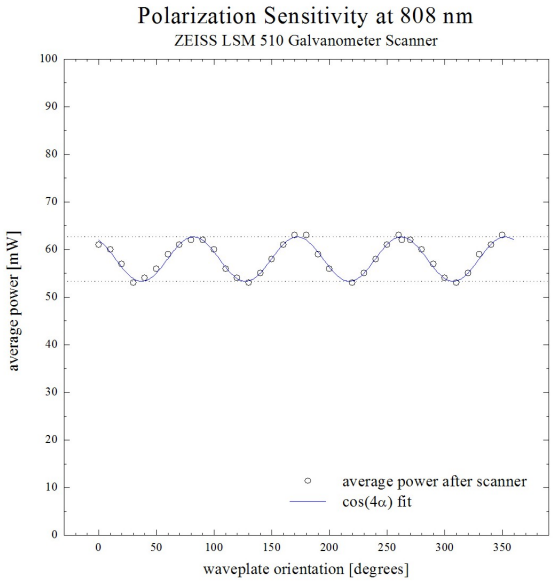

FIGURE 3.3.3. This graph shows the dependence of the reflectivity of the mirrors to the polarization of the incident laser beam.

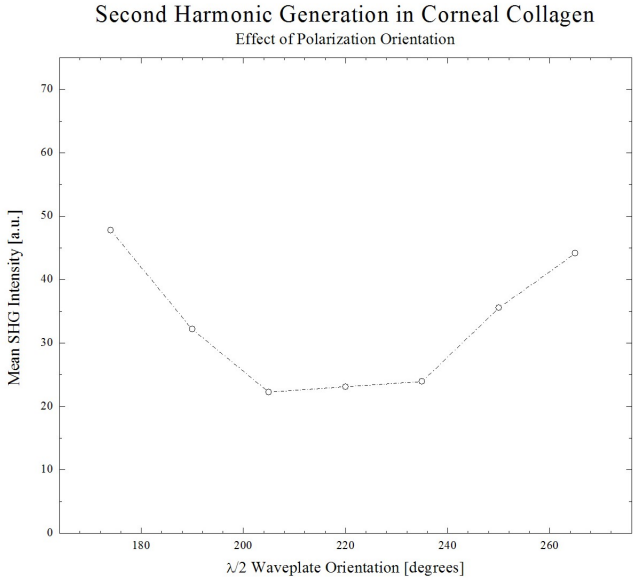

FIGURE 3.3.4. This graph shows the correspondence between the second harmonic signal and the polarization of the laser beam. It shows that the second harmonic signal intensity depends on the orientation of polarization of the laser as was predicted by theory and experimental by S. Roth and I. Freund **[53]**

CHAPTER 4

Theoretical basics

In this chapter the quantum mechanical basics for the multiphoton microscopy and second harmonics generation (SHG) will be described. The use of SHG for the microscopy of biological tissue has some big advantages: Unlike fluorescence signals from fluorescence labels the SH signal shows no bleaching during acquisition of repeated images from a given area. (see also Cox et al. [**15**]) This also indicates that no damage to the collagen structure occurs what is to be expected since SHG is a coherent process, unlike fluorescence, and no energy is lost. Also, as shown by Zoumi et al. [**58**], SH can be detected without change of intensity in a wide range of wavelengths (766 nm to 1064 nm). This means that the wavelength can be chosen to meet the needs of two-photon-fluorescence without compromise to the SH image. So the combination of two-photon-fluorescence labels and SH and their simultaneous imaging is possible.

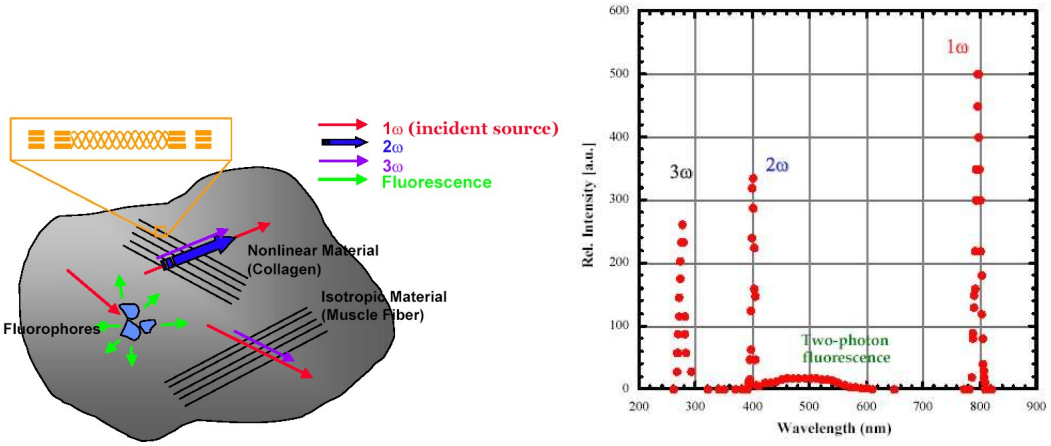

FIGURE 4.0.1. The left picture shows the three possibilities of what happens to the wavelength and the propagation direction of light incident on tissue. The right picture shows a graph were the intensity of the incident light wave (800 nm) and the intensities and wavelengths of the corresponding two-photon-fluorescence, the second harmonic and the third harmonic are displayed. [**35**]

4.1. Quantum Mechanics of Fluorescence Excitation

An exact physical explanation of fluorescence and with that of the interaction of the atoms, molecules and electro-magnetic fields can be given by using quantum mechanics. The Schroedinger equation for the whole system is

$$H\Psi_0(x) = E\Psi_0(x) \tag{4.1.1}$$

with the Hamiltonian

$$H_{ges} = \sum_k H^k + H_{Atom} + H^{'} \tag{4.1.2}$$

$\sum_k H^k$ defines the k conditions of the cavity which in this case describe the electro-magnetic waves in the vicinity of the atom. H_{Atom} is the Hamiltonian function of an atom that is supposed to be fixed and $H^{'}$ is the interaction energy between the two parts of the system. $H^{'}$ is small against the other two terms so it can be considered as a perturbation. Because of this assumption we can later use principles of perturbation theory.

First the terms of the Hamiltonian will be explained. The single quantum mechanical states of electro-magnetic waves will be described as bounded in a finite box potential which will be assumed infinite in the end. The vectorpotential $\vec{A}$ of the cavity states is then given by

$$\vec{A} = \sum_k q^k A^k = \sum_k q^k \mathfrak{e}^k e^{2\pi i \nu_k \left(s_x^k x + s_y^k y + s_z^k z\right)} \tag{4.1.3}$$

Also the following is known for electro-magnetic radiation in a cavity:

The number of possible eigen oscillations is limited and can be described in the frequency range between ν and $\nu + \Delta\nu$ as

$$Z(\nu)\,\Delta\nu = \frac{8\pi\nu^2}{c^3} V \Delta\nu \tag{4.1.4}$$

The Hamiltonian function of radiation in a cavity can be derived from the Maxwell equations for harmonic oscillators to be

$$\sum_k H^k = \sum_k h\nu_k \left(n_k + \frac{1}{2}\right), \text{ harmonic oszillator} \tag{4.1.5}$$

$$h\nu_{ss'} = \sum_k h\nu_k \left(n_k - n_k^{'}\right) \text{ , energy difference between two cavity states} \tag{4.1.6}$$

With this the matrix element $q^k$is given by:

$$\begin{aligned} q_{ss'}^k &= \sqrt{\frac{hc^2}{2\pi\nu_k V}\left(n_k + 1\right)} && \text{for } n_k^{'} = n_k + 1,\ n_l^{'} = n_l \\ &= \sqrt{\frac{hc^2}{2\pi\nu_k V}\left(n_k\right)} && \text{for } n_k^{'} = n_k - 1,\ n_l^{'} = n_l \\ &= 0 && \text{otherwise.} \end{aligned} \tag{4.1.7}$$

The Hamiltonian function for the fixed atom, H_{atom}, can be derived essentially from the known relations between the states of the atom which come from the current atomic models.

The interaction energy $H^{'}$ consists of the information on the impulse and location of the atomic electron, its potential energy in the atom and the vectorpotential of the electro-magnetic radiation field at the location of the electron. The spatial fluctuation of the vector potential can be neglected under the assumption that the wavelength of the light is big compared to the dimensions of the atom. By using the sum of the electronic momentum over all atomic electrons $\vec{P} = \sum_r eq_r$

$$H^{'} = -\frac{1}{c}\left(\vec{P}\vec{A}\right) \tag{4.1.8}$$

with the known relation that the temporal derivative of the vectorpotential is proportional to the electrical field strength $\frac{1}{c}\dot{\vec{A}} = \vec{E}$

$$H^{'} = -\vec{P}\vec{E} \tag{4.1.9}$$

So the interaction energy is the potential energy of the electronical momentum of the atomic electrons against the external electro-magnetic radiation field.

At this point we return to perturbation theory because it can be assumed that the interaction energy is small compared to the Hamiltonian of the atom or of the electro-magnetic field. So it is allowed to determine the wave equation by developing the eigen functions of the undisturbed system.

$$\Psi = \sum a_{ns}\Psi_{ns} \tag{4.1.10}$$

At an arbitrary time $t = 0$ the atom should be in a state n_0 and the cavity in a state s_0. In first approximation we get by using equation 4.1.1

$$a_{ns}^{(1)} = H^{'}_{ns,n^0s^0}\frac{1 - e^{2\pi i\left(\nu_{nn^0}+\nu_{ss^0}\right)t}}{h\left(\nu_{nn^0} + \nu_{ss^0}\right)} \tag{4.1.11}$$

Until now we only used calculation of perturbations of first order. From this we can conclude directly about the emission and absorption with involvement of one photon. So the absorption is basically dependent on the number of atoms in the ground state n_0 and on the light density $\rho(\nu)$ of the photons in the cavity which should have the exact frequency that is necessary to excite the atom. This manner of absorption is called one-photon-excitation.

Now we will go to the second order of perturbation calculation to describe the double absorption. Again, at an arbitrary time $t = 0$ the atom should be in the ground state n_0. The cavity in which the atoms reside at this point of time should contain two independent eigen oscillations which propagate in the same direction and have the same polarization. Further for the eigen frequencies ν_k, ν_l of these two eigen functions should the sum $\nu_k+\nu_l$ be the same as the frequency of the electronic transition in the atom. With this we get a possibility for a transition $n_0 \rightarrow n$ that is different from zero with the assumption that the cavity state s comes from s_0 by the absorption of a photon with the frequency ν_k (spectral range ν) and a second photon with the frequency ν_l (spectral range $\nu^{'}$). Using $H^{'}_{nn^{'}ss^{'}} = \sum_k \dot{q}_{ss^{'}}\left(\vec{P}_{nn^{'}}A^k\right)$ this leads to:

$$\begin{aligned} a_{ns}^{(2)} &= \frac{1}{c^2}\dot{q}^k_{n_k^0-1,n_k^0}\dot{q}^l_{n_l^0-1,n_l^0}\sum\left[\frac{\left(\vec{P}_{nn^{'}}\mathfrak{e}^l\right)\left(\vec{P}_{n^{'}n^0}\mathfrak{e}^k\right)}{h\left(\nu_{n^{'}n^0} - \nu_k\right)} + \frac{\left(\vec{P}_{nn^{'}}\mathfrak{e}^k\right)\left(\vec{P}_{n^{'}n^0}\mathfrak{e}^l\right)}{h\left(\nu_{n^{'}n^0} - \nu_l\right)}\right] \\ &\cdot\frac{1 - e^{2\pi i\left(\nu_{nn^0}-\nu_k-\nu_l\right)t}}{h\left(\nu_{nn^0} - \nu_k - \nu_l\right)} \end{aligned} \tag{4.1.12}$$

To simplify equation 4.1.12 we use the matrix elements defined in equation 4.1.7 which essentially describe the characteristics of the cavity. So the equation is described by system parameters like frequency (ν), eigen states (n), electronic moment, polarization and volume. This leads to

$$\begin{aligned} a_{ns}^{(2)} &= \frac{2\pi h}{V}\sqrt{n_k^0\nu_k n_l^0\nu_l}\sum_{n^{'}}\left[\frac{\left(\vec{P}_{nn^{'}}\vec{\mathfrak{e}}^{'}\right)\left(\vec{P}_{n^{'}n^0}\vec{\mathfrak{e}}\right)}{h\left(\nu_{n^{'}n^0} - \nu_k\right)} + \frac{\left(\vec{P}_{nn^{'}}\vec{\mathfrak{e}}\right)\left(\vec{P}_{n^{'}n^0}\vec{\mathfrak{e}}^{'}\right)}{h\left(\nu_{n^{'}n^0} - \nu_l\right)}\right] \\ &\cdot\frac{1 - e^{2\pi i\left(\nu_{nn^0}-\nu_k-\nu_l\right)t}}{h\left(\nu_{nn^0} - \nu_k - \nu_l\right)} \end{aligned} \tag{4.1.13}$$

Using the mean monochromatic radiation density $\rho(\nu)$ which is defined as

$$V\rho(\nu)\Delta\nu = \sum_{\nu<\nu_k<\nu+\triangle\nu} h\nu_k n_k^0 \tag{4.1.14}$$

we find the probability of the double absorption by summing up $\left|a_{ns}^{(2)}\right|^2$ over the cavity states s. For a big cavity this is an integration of the frequencies ν_k and ν_l.

$$\begin{aligned}\sum\left|a_{ns}^{(2)}\right|^2 &= 4\pi^2\cdot\left|\sum_{n'}\left[\frac{\left(\vec{P}_{nn'}\vec{\mathfrak{e}}'\right)\left(\vec{P}_{n'n^0}\vec{\mathfrak{e}}\right)}{h\left(\nu_{n'n^0}-\nu_k\right)}+\frac{\left(\vec{P}_{nn'}\vec{\mathfrak{e}}\right)\left(\vec{P}_{n'n^0}\vec{\mathfrak{e}}'\right)}{h\left(\nu_{n'n^0}-\nu_l\right)}\right]\right|^2\\ &\cdot\int\rho(\nu_k)\,\rho(\nu_l)\,\frac{4\sin^2\pi\left(\nu_{nn^0}-\nu_k-\nu_l\right)t}{h^2\left(\nu_{nn^0}-\nu_k-\nu_l\right)^2}d\nu_k d\nu_l\end{aligned} \tag{4.1.15}$$

In consideration of the condition for double absorption, that the sum of the frequencies in the cavity (ν_k,ν_l) is equal to the frequency (ν_{nn^0}) that is necessary to excite the atom we get at this point of resonance

$$w_{nn^0} = \frac{16\pi^4}{h^2}\int\rho\left(\nu_{nn^0}-\nu\right)\rho(\nu)\,d\nu\left|\vec{p}^k\vec{\mathfrak{e}}'\right|^2 \tag{4.1.16}$$

with $\vec{p}^k$ being the abbreviation of the sum in equation 4.1.15. The integral is to be done over the whole breadth of spectral lines in the cavity.

From this we can see the following:
The number of double absorptions is increased by the fact that it is proportional to the number of atoms in the ground state. On the other hand there is the quadratical dependence on the light density (s. equation 4.1.15) which is the cause why the effect is observable only with high light intensities. So we can summarize the following: The processes of double absorption and double emission can only occur in the very short time scale of the Heisenberg uncertainty relation because the single procedures in the process of double absorption respectively double emission do not comply with the energy conservation equation. This means that the atom changes its state n^0 to a virtual temporary state n' by absorbing or emitting a photon with the frequency ν. By absorbing or emitting another photon with the frequency v' the atom finally reaches its final state n.

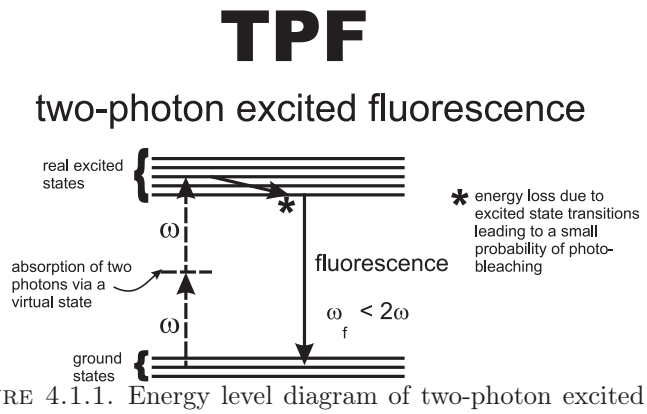

FIGURE 4.1.1. Energy level diagram of two-photon excited fluorescence TPF is a four-level process that includes the ground state, one virtual state and at least two real electronic or vibronic excited states.

A more detailed description of the process can be found in appendix A.

4.2. Generation of Second Harmonics

4.2.1. Second Harmonics Generation in Collagen. Collagen is known to consist of three parallel, intertwined, polar helices. In collagen type I two of these strands are the same while the third one is slightly different (see table 1). Optical SHG averages molecular properties over dimensions of the order of a wavelength of light, so that all local asymmetries disappear. As a result of this the collagen molecule can be considered to have cylindrical symmetry about its long axis. This, together with the polarity of the individual chains implies an effective symmetry for SHG of C_∞.

Let us label the polar axis as the z axis, and choose as $x-$ and y - axes as an arbitrary orthogonal set in a plane normal to this axis. So we can write the components of the harmonic polarization,$\vec{P}(2\omega)$, induced by optical fields $\vec{E}(\omega)$ as **[53]**

$$\begin{aligned} P_z(2\omega) &= \beta_3 E_z^2(\omega) + \beta_1 \left\{ E_x^2(\omega) + E_y^2(\omega) \right\} \\ P_x(2\omega) &= 2\beta_1 E_x(\omega) E_z(\omega) \\ P_y(2\omega) &= 2\beta_1 E_y(\omega) E_z(\omega) \end{aligned} \tag{4.2.1}$$

where

$$\begin{aligned} \beta_3 &= \beta_{zzz} \\ \beta_1 &= \beta_{zxx} = \beta_{zyy} = \beta_{xzx} = \beta_{yzy} = ... \end{aligned} \tag{4.2.2}$$

Equations 4.2.1 and 4.2.2 follow from the form of the C_∞ piezoelectric tensor as given by Fukada **[19]**, the formal equivalence to the hyperpolarizability tensor, and the assumed validity of the Kleinman **[37]** symmetry conditions. Kleinman symmetry means that all of the elements in the nonlinear susceptibility tensor that are connected by permutation of indices are equal. The assumption of Kleinman symmetry is valid because the second harmonic wavelength (400 nm) is far from the wavelength of the first electronic transition in collagen (approximately at 310 nm).

Because the collagen molecules are aligned parallel within a fibril equations 4.2.1 and 4.2.2 describe also the SHG by a single fibril using

$$\beta_{fibril} = N\beta_{molecule} \tag{4.2.3}$$

where N is the number of collagen molecules comprising the fibril. Equation 4.2.3 implies that a fibril may be treated like a simple, super-giant molecule. This approximation is correct as long as the sample geometry and fibril dimensions are such that the relative phases of the various optical fields do not vary appreciably over an individual fibril. To show this the setup in figure 4.2.1 was used by S. Roth and I. Freund **[53]**. As a possibility to get collagen fibrils a piece of a tendon was used.

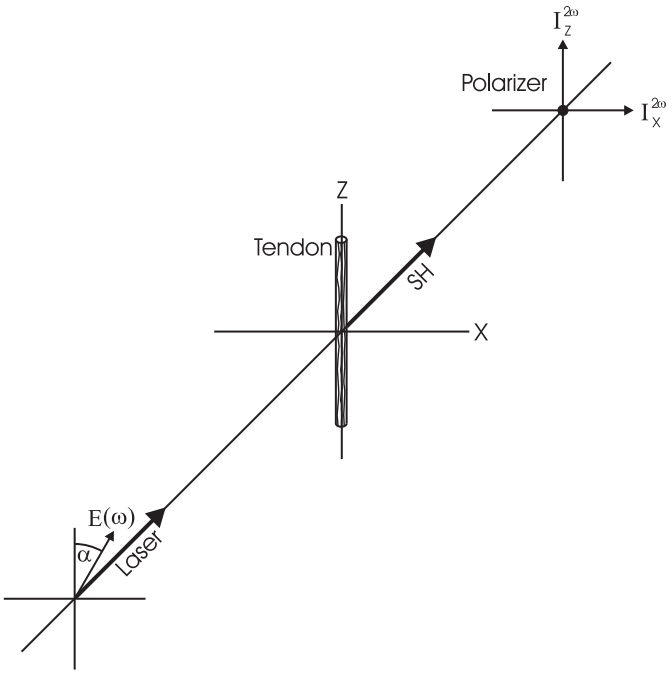

FIGURE 4.2.1. Experimental geometry

To change the opacity of the tendon it was stretched against a glass surface, what resulted in a flattening of the tendon cross section and hence an increased transparency. The collagen fibrils were not disordered from their parallel alignment by the process of stretching. The SH signal measured remained unchanged except that its intensity increased as did the intensity of the scattered light due to the better transparency. So the conclusion was that scattering is only a secondary effect and in spite of the large amount of light scattering, that the light polarized parallel or perpendicular to the tendon axis retains its polarization to better than 99%. For other orientations the tendon behaves like a highly birefringent crystal. S. Roth and I. Freund **[53]** found in their experiment that the flattened tendons viewed in white light between crossed polarizers exhibit the interference colors characteristic of thin anisotropic crystal plates and thereby displaying the expected high degree of birefringence of the individual fibers.

With the experimental setup shown in figure 4.2.1 the intensity of the SHG for which the harmonic is polarized parallel to the tendon axis, $I_Z^{2\omega}(\alpha)$, and normal to the tendon axis $I_X^{2\omega}(\alpha)$ as a function of the angle α that the incident laser polarization makes relative to the Z-(tendon) axis, was measured by S. Roth and I. Freund (s. figure 4.2.2)

To understand figure 4.2.2 we have to look first at the theory. From electron microscope studies it is known that the polar direction of the fibrils alternates up/down in a more-or-less random fashion throughout the tendon. So to sum up the SH contributions from different fibrils the intensities rather than the field amplitudes have to be summed also we can neglect coherence-length effects. On the other hand the linear optical properties approximate that of a birefringent crystal which must not be neglected in describing the laser fields. Also the case that the fibril axes are not perfectly aligned, but are rather distributed in some way around the mean tendon axis, has to be considered. According to these considerations the following calculations were done by S. Roth and I. Freund **[53]**:

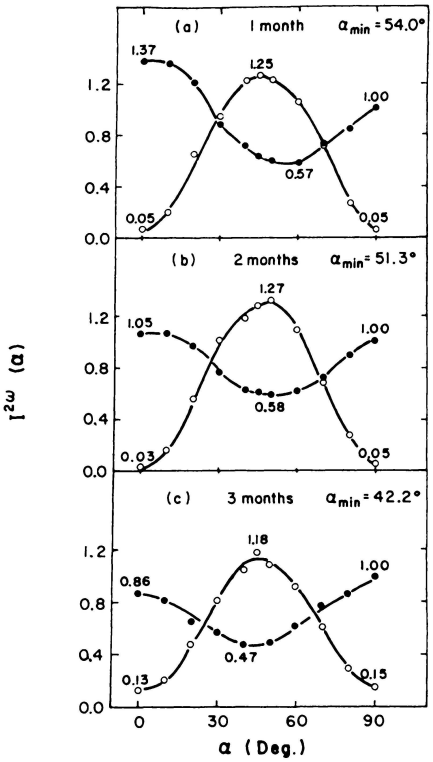

FIGURE 4.2.2. $I_Z^{2\omega}$, filled circles, and $I_X^{2\omega}$, open circles, as measured experimentally for rats of different ages. The results are typical for the age groups shown but vary somewhat from specimen to specimen. The data are normalized to $I_Z^{2\omega}(90) = 1$, and the three most important data values are given for each graph. The angle α_{min} at which $I_Z^{2\omega}$ is a minimum is used to determine $\frac{\beta_3}{\beta_1}$ as described in the text. **[53]**

The external (tendon) reference frame is denoted by XYZ as shown in figure 4.2.1, the fibril reference frame by xyz as in equation 4.2.1, and the fibril axis, the z axis, is assumed to make polar angle θ and azimuthal angle ϕ relative to the XYZ frame. At the location of the fibril the incident laser field consists of two orthogonal components oriented along the tendon Z- and X-axes which is written for unit amplitude as

$$E_Z(\omega) = \cos\alpha \tag{4.2.4}$$

$$E_X(\omega) = e^{i\delta}\sin\alpha \tag{4.2.5}$$

The factor $e^{i\delta}$ takes account of the fact that in the birefringent tendon the two components of the laser propagate with different phase velocities. In the fibril reference frame the components of the fields in equation 4.2.4 give rise to the fields $E_x(\omega)$, $E_y(\omega)$ and $E_z(\omega)$ of equations 4.2.1. These produce the nonlinear polarizations of equations 4.2.1, which then combine in the tendon frame as macroscopic components which may be written in the form

$$P_j(2\omega) = A_j + B_j e^{i\delta} + C_j e^{2i\delta} \tag{4.2.6}$$

The relative phase δ varies from location to location within the tendon, so the average over all δ is taken and written $I_j^{2\omega} = |P_j(2\omega)|^2$ with

$$|P_j(2\omega)|^2 = A_j^2 + B_j^2 + C_j^2 \tag{4.2.7}$$

By assuming cylindrical symmetry about the tendon axis for the distribution of fibril orientations A^2, B^2 and C^2 of equation 4.2.7 are averaged over all ϕ. To describe the orientation distribution of the fibrils a normalized distribution function $\Pi(\theta)$ is used. The distribution function $\Pi(\theta)$ arises from the fact that stretching the tendon does not completely straighten the individual fibers, but leaves a residual wavy pattern. This can be approximated by a sinusoid running along the Z axis with the displacement, for example, in the X-Z plane

$$X = a\sin(kZ) \tag{4.2.8}$$

The angle θ that the fibrils comprising the fiber make with the Z axis is easily seen to be

$$\theta = \tan^{-1}[ak\cos(kZ)] \tag{4.2.9}$$

so the maximum possible angular displacement is $\theta_{max} = \tan^{-1}(ak)$ in equation 4.2.13. $\Pi(\theta)\,d\theta$ may be seen to be proportional to the length of arc over which θ changes by no more than $d\theta$, i.e. ,$\Pi(\theta)$ is proportional to one over the curvature, so that except for normalization,

$$\Pi(\theta) = \left[k\cos^2\theta\sqrt{(ak)^2 - \left[1+(ak)^2\right]\sin^2\theta}\right]^{-1} \tag{4.2.10}$$

This results in

$$\begin{aligned} I_Z^{2\omega}(\alpha) &= Q\sin^4\alpha + R\sin^2 2\alpha + S\cos^4\alpha \\ I_X^{2\omega}(\alpha) &= T\sin^4\alpha + Q\sin^2 2\alpha + R\cos^4\alpha \end{aligned} \tag{4.2.11}$$

with

$$\begin{aligned} Q &= \left[\left(3\rho^2 - 10\rho + 11\right)I_2 + \left(-6\rho^2 + 28\rho - 30\right)I_4\right. \\ &\quad \left. + \left(3\rho^2 - 18\rho + 27\right)I_6\right] \\ R &= \frac{1}{2}\left[1 + (2\rho - 7)I_2 + \left(\rho^2 - 8\rho + 15\right)I_4 + \left(-\rho^2 + 6\rho - 9\right)I_6\right] \\ S &= 9I_2 + (6\rho - 18)I_4 + \left(\rho^2 - 6\rho + 9\right)I_6 \\ T &= \frac{1}{16}\left[\left(5\rho^2 + 6\rho + 9\right) + \left(-15\rho^2 + 18\rho + 9\right)I_2\right. \\ &\quad \left. + \left(15\rho^2 - 54\rho + 27\right)I_4 + \left(-5\rho^2 + 30\rho - 45\right)I_6\right] \end{aligned} \tag{4.2.12}$$

Here $\rho = \frac{\beta_3}{\beta_1}$,

$$I_m = \int_0^{\theta_{max}} d\theta\cos^m\theta\Pi(\theta) \tag{4.2.13}$$

In the equations 4.2.12 all constants were neglected since the results of measurements are always relative intensities. To verify these considerations a perfectly ordered array of fibrils is considered, i.e., $\theta_{max} = 0$, since this represents a reasonable first approximation to the actual situation and provides a useful initial guide to the interpretation of the measurement. With this assumption it may be written

$$\begin{aligned} I_Z^{2\omega}(\alpha) &= \beta_3^2\cos^4\alpha + \beta_1^2\sin^4\alpha \\ I_X^{2\omega}(\alpha) &= \beta_1^2\sin^2 2\alpha \end{aligned} \tag{4.2.14}$$

A plot of the equations 4.2.14 can be seen in figure 4.2.3.

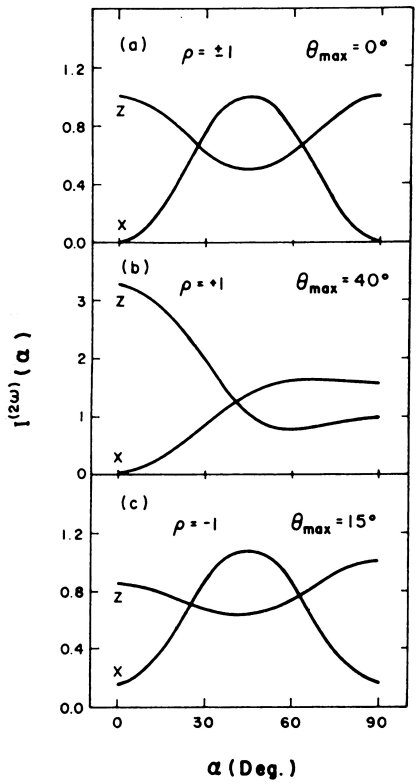

FIGURE 4.2.3. Calculated $I^{2\omega}$ curves for different values of $\rho = \frac{\beta_3}{\beta_1}$ and θ_{max} [Equation 4.2.9]. (a) Perfectly ordered tendon, equations 4.2.14; (b) Equations 4.2.11 and 4.2.12, $\rho > 0$. Note that even for highly disordered tendon ($\theta_{max} = 40^o$), $I_X^{2\omega}(0)$ is entirely negligible (0.026); (c) Equations 4.2.11 and 4.2.12, $\rho < 0$. Note the nearly quantitative agreement with the data of figure 4.2.2(c). **[53]**

As can be seen the calculated curves correctly predict the form of the measured ones.

From these experiments can be seen that the polarization of SH light in the forward direction is sensitive to the degree and kind of molecular order. More information can be obtained, in principle, through angular measurements which are capable of delineating the range over which order persists. **[7, 18]** The conclusion that can be drawn is that in our microscope pictures we were able to see the spatial order of collagen fibers by their SH signal.

4.2.2. Efficiency of Second Harmonics Generation. The use of a pulsed laser, instead of a CW laser, increases the instantaneous peak power of the input radiation and consequently improves the SHG efficiency **[20]**. A pulse can be temporally defined by the general function

$$U(t) = U_p e^{-i\omega_0 t} \cdot f\left(\frac{t}{\tau_p}\right) \tag{4.2.15}$$

where ω_0 is the central frequency and U_p the amplitude. The function $f\left(\frac{t}{\tau_p}\right)$ is given by $e^{-\frac{4(\ln 2)t^2}{\left(\frac{\tau_p}{2}\right)}}$ for a Gaussian pulse shape and by $\text{sech}^2 \frac{1{,}76t}{\tau_p}$ for a hyperbolic

secant pulse shape. **[33]** The pulse width τ_p is the Full-Width at Half-Maximum (FWHM) of the intensity envelope function $I(t)$ given by

$$I(t) = U_p^2 \cdot f^2\left(\frac{t}{\tau_p}\right) \tag{4.2.16}$$

The fundamental input average power $\bar{P}_\omega$ is simply given by

$$\int_{-\infty}^{\infty} I(t)\,dt = U_p^2 \int_{-\infty}^{\infty} f^2\left(\frac{t}{\tau_p}\right) dt = U_p^2 \tau_p \int_{-\infty}^{\infty} f^2(u)\,du = U_p^2 \tau_p \cdot F \tag{4.2.17}$$

where F is a constant. Using equation 4.2.16, the second-harmonic average power $\bar{P}_{2\omega}$ is given by

$$\int_{-\infty}^{\infty} I^2(t)\,dt = aU_p^4 \int_{-\infty}^{\infty} f^4\left(\frac{t}{\tau_p}\right) dt = aU_p^4 \tau_p \int_{-\infty}^{\infty} f^4(u)\,du = aU_p^4 \tau_p \cdot G \tag{4.2.18}$$

with $G \neq F$. Finally, we have the relationship

$$\bar{P}_{2\omega} = aU_p^4 \tau_p \cdot G = a\frac{\bar{P}_\omega^2}{F^2 \tau_p^2}\tau_p \cdot G \propto \frac{\bar{P}_\omega^2}{\tau_p} \tag{4.2.19}$$

Equation 4.2.19 shows that the efficiency of second harmonic generation is enhanced by the use of ultrashort pulses since the detected average second harmonic power is inversely proportional to the laser pulse width. Therefore, femtosecond pulses are used to maximize the second harmonics intensity for a given average power. There is no advantage to be gained from using femtosecond pulses for time resolution since the time scale for second harmonic generation is a few femtoseconds which is shorter than the pulses themselves. S. Fine and W. P. Hansen **[17]** found experimentally that their collagenous tissue samples converted on the order of 10^{-10} of the laser irradiance at $694\,nm$ to peak sample radiance at $347\,nm$. Since some light scattering occurs in the sample a conversion efficiency of significantly more than 10^{-10} may be possible. Also the SHG efficiency should decrease monotonically with the peak power of the laser. The result of this is that the second harmonic emission pulse should be temporally narrower than the input laser pulse. Experimental a narrowing of at least 30% at half maximum was observed.

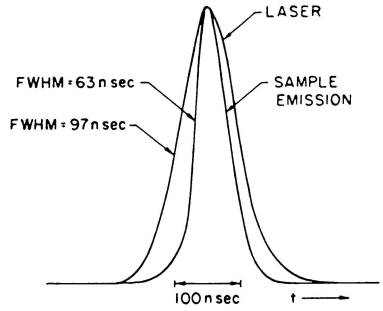

FIGURE 4.2.4. Drawing of normalized laser and sample emission pulses taken from photograph of dual-beam oscilloscope traces. Full width at half-maximum for the laser pulse is $97\,ns$, while it is $63\,ns$ for the emission pulse. It shows clearly the narrowing of the emitted pulse in correlation to the incident laser pulse. **[17]**

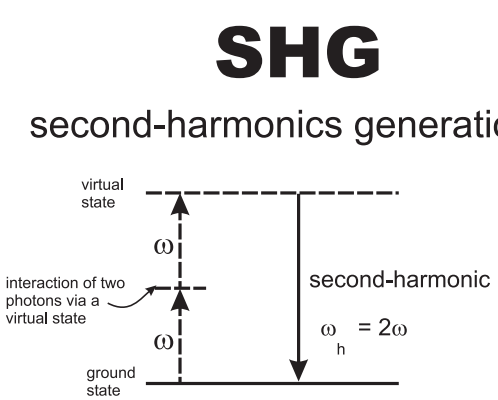

FIGURE 4.2.5. Energy level diagram of second-harmonic generation. SHG is a three-level process that involves only virtual states beside the ground state and is therefore non-resonant. The second-harmonic photon is generated almost instantaneously [within a few fs]. Also energy loss can not occur unlike with TPF.

4.2.3. Propagation of the Second Harmonic Signal. As SHG is a coherent process, its radiation pattern is not uniform in all directions [**12, 15**]. The electric polarization of the system is described by

$$\begin{aligned} \vec{P} &= \alpha \cdot \vec{E} + \beta \cdot \vec{E} \cdot \vec{E} + \cdots \\ P_i &= \sum_j \alpha_{ij} \cdot E_j + \sum_j \sum_k \beta_{ijk} \cdot E_j \cdot E_k + \cdots \end{aligned} \tag{4.2.20}$$

with α and β the second and third order polarization tensors, respectively. For a single radiating dipole μ in classical electro-magnetic theory the following equations for the field vectors can be derived

$$\vec{E}_{sc} = \left(\frac{\omega_3^2}{c^2 R}\right)\left(\mu \times \hat{R}\right) \times \hat{R} \tag{4.2.21}$$

$$\vec{H}_{sc} = \left(\frac{\omega_3^2}{c^2 R}\right)\left(\mu \times \hat{R}\right) \tag{4.2.22}$$

with $\hat{R}$ an unit vector from the dipole to the point of observation. With this the Poynting vector is

$$\vec{S} = \frac{c}{4\pi}\left(\vec{E}_{sc} \times \vec{H}_{sc}\right) = \frac{\omega_3^4}{4\pi c^3 R^2}\left[\mu^2 - \left(\mu \cdot \hat{R}\right)^2\right]\hat{R} = \frac{\omega_3^4 \mu \lambda_3^2}{4\pi c^3 R^2}\hat{R} \tag{4.2.23}$$

The corresponding quantum-mechanical expression for the energy flux vector scattered by a single molecule a is

$$\begin{aligned} \frac{w_{k_3 \leftarrow k_1 k_2} \hbar \omega_{k_3}}{R^2 d\Omega}\hat{R} &= \frac{2\pi}{R^2}\left(\frac{\hbar}{mc}\right)^4 \left(\frac{e^2}{\hbar c}\right) I(\omega_1)\, I(\omega_2) \\ &\quad \times \left| f_a\left(\vec{k}_3 \lambda_3, \vec{k}_2 \lambda_2, \vec{k}_1 \lambda_1\right)\right|^2 \hbar \omega_3 \hat{R} \end{aligned} \tag{4.2.24}$$

with $\vec{k}_i$ the respective wave vector, λ_i the respective polarization and the scattering amplitude

$$\begin{aligned} f_a\left(\vec{k}_3\lambda_3, \vec{k}_2\lambda_2, \vec{k}_1\lambda_1\right) &= ie^2m^2 \sum_q \sum_r \omega_{0q}\omega_{qr}\omega_{r0} \\ &\left[\frac{\left(\mu\lambda_1^{(\alpha)}\right)_{0q}\left(\mu\lambda_2^{(\alpha)}\right)_{qr}\left(\mu\lambda_3^{(\alpha)}\right)_{r0}}{(\omega_1-\omega_{0q})(\omega_1+\omega_2-\omega_{0r})} \right. \\ &+\frac{\left(\mu\lambda_2^{(\alpha)}\right)_{0q}\left(\mu\lambda_1^{(\alpha)}\right)_{qr}\left(\mu\lambda_3^{(\alpha)}\right)_{r0}}{(\omega_2-\omega_{0q})(\omega_1+\omega_2-\omega_{0r})} \\ &+\frac{\left(\mu\lambda_1^{(\alpha)}\right)_{0q}\left(\mu\lambda_3^{(\alpha)}\right)_{qr}\left(\mu\lambda_2^{(\alpha)}\right)_{r0}}{(\omega_1-\omega_{0q})(-\omega_2-\omega_{0r})} \\ &+\frac{\left(\mu\lambda_2^{(\alpha)}\right)_{0q}\left(\mu\lambda_3^{(\alpha)}\right)_{qr}\left(\mu\lambda_1^{(\alpha)}\right)_{r0}}{(\omega_2-\omega_{0q})(-\omega_1-\omega_{0r})} \\ &+\frac{\left(\mu\lambda_3^{(\alpha)}\right)_{0q}\left(\mu\lambda_1^{(\alpha)}\right)_{qr}\left(\mu\lambda_2^{(\alpha)}\right)_{r0}}{(\omega_1+\omega_2+\omega_{0q})(\omega_2+\omega_{0r})} \\ &\left. +\frac{\left(\mu\lambda_3^{(\alpha)}\right)_{0q}\left(\mu\lambda_2^{(\alpha)}\right)_{qr}\left(\mu\lambda_1^{(\alpha)}\right)_{r0}}{(\omega_1+\omega_2+\omega_{0q})(\omega_1+\omega_{0r})} \right] \end{aligned} \tag{4.2.25}$$

The wave vectors $\vec{k}_1$ and $\vec{k}_2$ and the polarizations λ_1 and λ_2 belong to the incident beam while the wave vector $\vec{k}_3$ and the polarization λ_3 belong to the produced second harmonic radiation. From the equations 4.2.23 and 4.2.24 the component of the induced dipole in the direction of polarization of the scattered wave can be derived as

$$\begin{aligned} \mu_3 &= \left(\frac{1}{8}\right)^{\frac{1}{2}}\left(\frac{e\hbar^2}{m^2}\right)\left[\frac{E_{\lambda_1}(\omega_1)E_{\lambda_2}(\omega_2)}{\omega_3(\omega_1\omega_2)^{\frac{1}{2}}}\right] \\ &\times f_\alpha\left(\vec{k}_3\lambda_3, \vec{k}_2\lambda_2, \vec{k}_1\lambda_1\right) \end{aligned} \tag{4.2.26}$$

by substituting

$$I(\omega_i) = \left[\frac{cE_{\lambda_i}^2(\omega_i)}{8\pi}\right] \quad i = 1, 2 \tag{4.2.27}$$

Because of the definition of the tensor β we get

$$\mu_{\lambda_3} = \beta_{\lambda_3\lambda_2\lambda_1}E_{\lambda_2}E_{\lambda_1} \tag{4.2.28}$$

With this equation we can find the following correspondence

$$\beta_{\lambda_3\lambda_2\lambda_1} = \left(\frac{1}{8}\right)^{\frac{1}{2}}\left(\frac{e\hbar^2}{m^2}\right)\left[\frac{1}{\omega_3(\omega_1\omega_2)^{\frac{1}{2}}}\right] f_\alpha\left(\vec{k}_3\lambda_3, \vec{k}_2\lambda_2, \vec{k}_1\lambda_1\right) \tag{4.2.29}$$

between the matrix elements of β and the scattering amplitude f_α. For a group of molecules the sum over the scattering amplitudes for the individual molecule weighted by phase factors will give the corresponding matrix element.

So, as illustrated in figure 4.2.6, the far - field radiation pattern of SH is dependent not only on the size, but also the shape of a scatterer, as a consequence of the coherent addition of the signal field from each induced dipole inside a sample.

[12] The radiation from a single Hertzian dipole along the x axis is symmetrical in both forward (+z) and backward (-z) directions (figure 4.2.6(A)). The coherent superposition of the radiation fields from an ensemble of dipoles in the x-y plane exhibits a narrow but still symmetrical pattern in both directions (figure 4.2.6(B)). The coherent addition of the radiation fields from an ensemble of dipoles lined up along the z axis builds a large signal in the forward direction because of the constructive interference, and a weak signal in backward direction because of the destructive interference (figure 4.2.6(C)). For a large scatterer centered at the focus or a bulk medium, the coherent addition in three dimensions builds a sharp and directional forward going signal (figure 4.2.6(D)). Thus, forward detection is suitable for imaging objects with an axial length comparable to or larger than the excitation wavelength. So in our case the SH signal is strongly detectable only in the propagation direction of the incident laser beam.

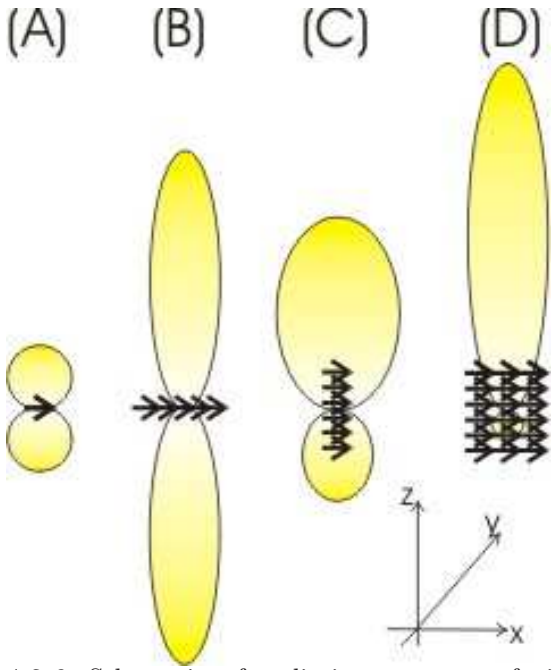

FIGURE 4.2.6. Schematic of radiation patterns of single and an ensemble of Hertzian dipoles coherently induced by forward-propagating (+z) excitation beams **[12]**

For more details on the subject of propagation read the article from R. Bersohn and Yoh-Ha Pao and H.L. Frisch **[7]**.

4.3. Laser - Tissue Interaction

To understand the interaction we have to look at some basic optical properties of tissue first. In general the index of refraction n, the absorption and the scattering coefficient μ_a and μ_s and at last the anisotropy factor $g = \langle \cos\theta \rangle$ with θ the angle of photon deflection after one single scattering event have to be considered. So as g approaches -1, 0 and 1 this describes highly backward, isotropic and extremely forward scattering, respectively. From these the following properties can be derived **[35, 57]**:

- The total attenuation coefficient $\mu_t = \mu_a + \mu_s$

- The mean free path $mfp = \frac{1}{\mu_t}$
- The effective attenuation coefficient $\mu_{eff} = \{3\mu_a [\mu_a + \mu_s (1-g)]\}^{\frac{1}{2}}$
- The penetration depth $\delta = \frac{1}{\mu_{eff}}$
- The fluency rate-versus-depth $\phi(z) = \phi_0 k e^{-\frac{z}{\delta}}$ for $z > \delta$ with ϕ_0 the irradiance and k a scalar that depends on the amount of backscattered reflectance [**31**]
  k has usually values between 2 and 4. The depth at which the fluency rate drops to $\frac{\phi_0}{e}$ is $\delta [1 + \ln(k)]$ [**31**]

Lets just have a look at an example: Human myocardium tissue at a wavelength of 1064 nm. Under this condition the basic properties are: $\mu_a = 0.3\, cm^{-1}$, $\mu_s = 178\, cm^{-1}$ and $g = 0.964$. So a photon of this light is able to travel about 3.3 cm in the tissue before absorption and about 56 μm between scattering events. A compendium of the basic optical properties of different tissue and how these were obtained can be found in the paper from Wai-Fung Cheong et al. [**13**]. Figure 4.3.1 shows a chart of the absorption of laser light by tissue components.

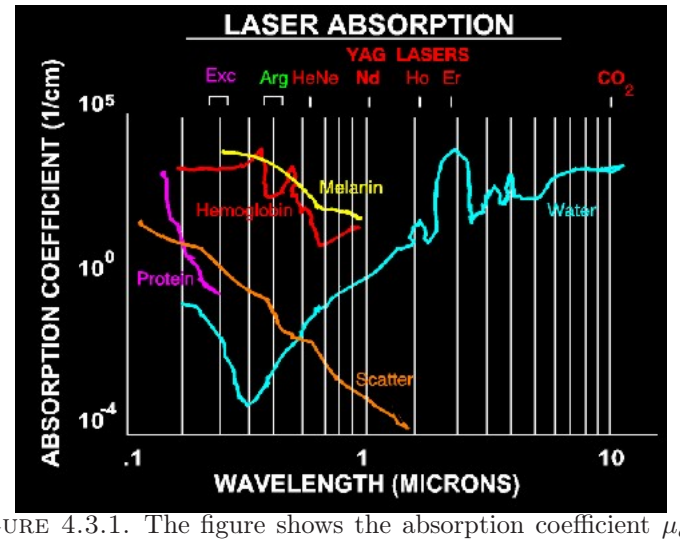

FIGURE 4.3.1. The figure shows the absorption coefficient μ_a in relation for different wavelengths of incident laser radiation and in dependence of different absorbing materials. [**32**]

Let us now turn to the effects of laser radiation interacting with biological tissue. Four main effects can be discerned [**41**]:

(1) Photochemical and photo-biological smooth effects: the irradiance could be continuous-wave or pulsed, from $10^{-3}\, \frac{W}{cm^2}$ to $1\, \frac{W}{cm^2}$ or from $10^{-2}\, \frac{J}{cm^2}$ to $10^5\, \frac{J}{cm^2}$, its temporal duration is very variable.
(2) Photo-thermal effects: the radiation is absorbed by the tissue, transforming into internal energy and producing an temperature increment; the following processes can be thermo-physical, chemical or biological in nature. The irradiance could be continuous-wave or pulsed, from $0.1\, \frac{W}{cm^2}$ to $10^5\, \frac{W}{cm^2}$ or from $0.1\, \frac{J}{cm^2}$ to $10^6\, \frac{J}{cm^2}$, its temporal duration is from 1 ms to hours.
(3) Photochemical hard effects or photoablation: UV radiation is used because the photon's high energy can break molecular links and ionize atoms. By this way only atoms and molecules in the focus of the beam are affected.

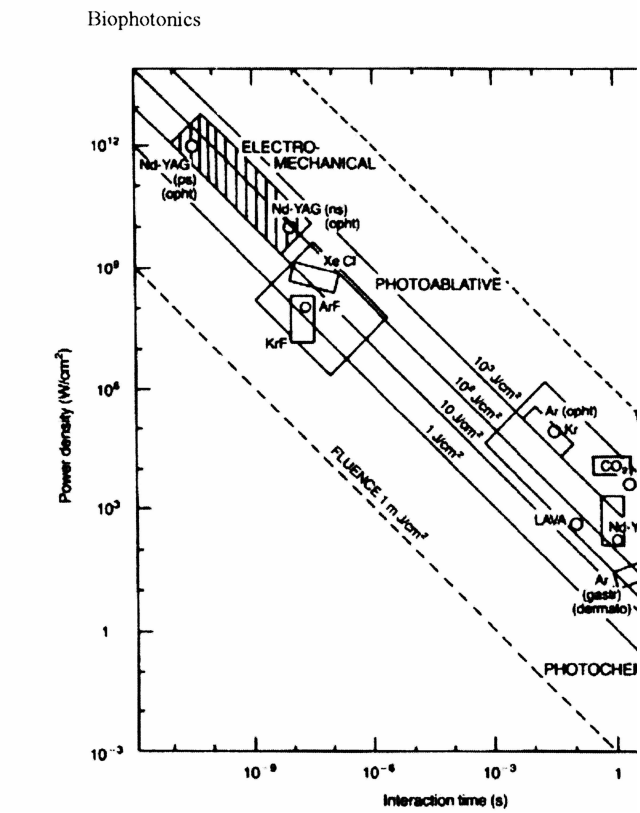

FIGURE 4.3.2. Medical lasers interaction map. The ordinate axis corresponds to the irradiance (in $Watts/cm^2$ on a logarithmic scale) and is commonly labeled "power density"; the abscissa corresponds to the interaction time (in seconds on a logarithmic scale); drawn diagonally are the lines of constant fluency (in J/cm^2) by increasing magnitude. [**39**]

The exposition time is very short, from 1 ns to 500 ns and irradiance from $10^5 \frac{W}{cm^2}$ to $10^9 \frac{W}{cm^2}$.

(4) Photodisruption: In this process a very short exposition time from ps to fs and high-powered laser beams, which are focused by lenses into the treated tissue, are used. The so obtained irradiance is in the magnitude of $10^{14} \frac{W}{cm^2}$.

These four processes may occur singly but can also be intermingled with each other.

In our work we used the photodisruptive process, which relies on nonlinear light absorption leading to the generation of a plasma at the laser focus. To create an ionized atom an energy of 10 eV or more is needed. But each photon from the laser at 1064 nm has only 1.17 eV, so a multiphoton process has to occur to provide enough energy. By applying a fluency of about 100 $\frac{J}{cm^2}$ with extremely short pulses (fs) a locally high electric field ($10^6 \sim 10^7 \frac{V}{cm}$) is generated, which is comparable to average atomic or intra-molecular Coulomb electric fields. This will induce a dielectric breakdown, resulting in the formation of a microplasma with a temperature of about 15 000 K in the focus [**4**], an ionized volume with a very large free-electron density via electron avalanche growth (see figure 4.3.3).

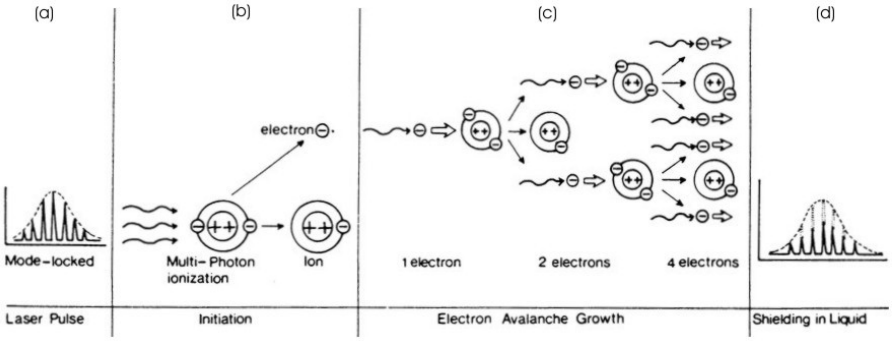

FIGURE 4.3.3. Initiation, growth and shielding effect off plasma formation by optical breakdown. The dominant mechanism of initiation of ionization by a mode–locked pulse is multiphoton absorption (b). After a free electron is produced, the plasma grows as a cascade or avalanche when photons cause free electrons to accelerate and collide with atoms, resulting in more free electrons and ions (c). This photon absorption reduces light transmission along the beam path, known as shielding (d), compared to the original pulse shape (a). [**49**]

The shock wave associated with the plasma expansion, which starts immediately with the plasma formation, generates a localized mechanical rupture over dimensions where the rise in pressure exceeds the yield strength of encountered tissues. Because of the temperature of the microplasma vaporization and melting of liquids and solids will occur in a small volume near the focal point [**48, 50**]. Thermal denaturation of protein and nucleic acids is calculated to be confined to a radius of $0.1\,mm$ for a $1\,mJ$ pulse [**25**]. This means that even so locally high temperatures briefly occur the total heat energy is low and photocoagulation is not important. The shock wave generated by the plasma expansion is due to a combination of several mechanisms. First is the rapid plasma expansion which begins as a hyper-sonic ("shock") wave [**6, 16, 38**]. A second, weaker source of hyper-sonic and sonic ("acoustic") waves is stimulated Brillouin scattering, in which the laser light itself creates the acoustic wave that scatters it [**51, 8**]. (Hyper-sonic means a velocity of about $4\,\frac{km}{s}$, while acoustic means a velocity of about $1.5\,\frac{km}{s}$ for the wave front propagation) The focal heating can lead to a phase change (vaporization and melting) and thermal expansion, both of which generate acoustic waves [**24, 14, 9**]. And at last the laser light, if sufficiently strong, will deform a target through electrostriction (the mechanism that leads to simple Brillouin scattering [**51**]) and through radiation pressure due to momentum transfer from photons to atom during inverse bremsstrahlung [**52**]. The table 1 shows the estimated contributions of these mechanisms to the pressure wave after optical breakdown.

More information on plasma shielding effects and about the shock wave can be found in the paper from Puliafito and Steinert [**49**]. In the appendix C there are some formulas concerning the connection of laser energy and ablation depth calculated via formulas from plasma physics.

Mechanism	Maximum Pressure [Atmospheres]
Plasma formation	1000 - 2000
Stimulated Brillouin scattering	50 - 100
Phase change (vaporization)	100
Thermal expansion	100
Electrostriction	0.01 - 100
Radiation pressure	0.01

TABLE 1. Estimated contributions to the pressure wave that occurs after optical breakdown. [**49**]

CHAPTER 5

Second harmonic imaging

5.1. Preliminary Tests

In the beginning some words about our handling of the samples. The excised porcine eyes were obtained in the slaughterhouse in Mannheim. Because of the slaughtering procedure nearly all eyes had a damaged epithelium. So the epithelium was removed carefully before our experiments.

The transport to either Perfect Vision in Heidelberg, where the laser system resides, or directly to the microscope facility of the Max – Planck – Institute for medical research in Heidelberg was performed in a styrofoam box on ice. The eyes were put in the box in that way that the cornea was face up and could not be damaged during the transport. PBS (*P*hosphate *B*uffered *S*aline) was used to prevent the eyes from getting dry. After laser treatment or after arrival at the microscope facility the corneas were carefully removed manually by using a very sharp knife or a scalpel to minimize the possible formation of artifacts due to the stress induced by the blade. The removed corneas were put into PBS awaiting further treatment. That could mean staining or fixation with PFA (*P*ara*F*orm*A*ldehyde in PBS) or Acetone. (The recipes for PBS and PFA can be found in the appendix)

As a first experiment we looked if second harmonic (SH) imaging is possible with the microscope setup described in chapter 3. After positive results we checked if the SH signal was disturbed by the autofluorescence of the collagen. For this we

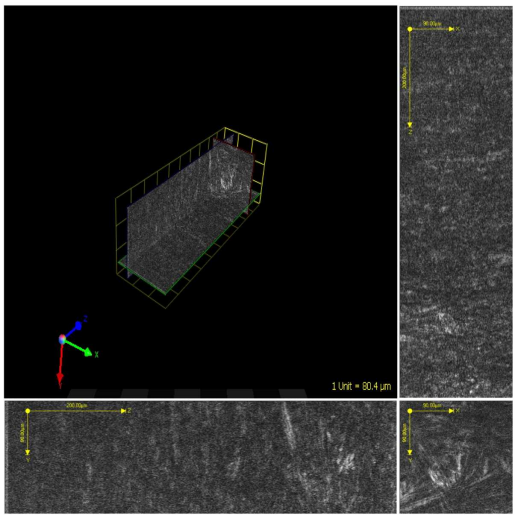

FIGURE 5.1.1. A stack picture of porcine cornea to check if second harmonic imaging is possible or if it is disturbed by the autofluorescence signal of the collagen. As can be seen no disturbance is visible. The dimensions of the stack are in the x - and y directions $230.3\,\mu m \times 230.3\,\mu m$ and in the z direction $800\,\mu m$.

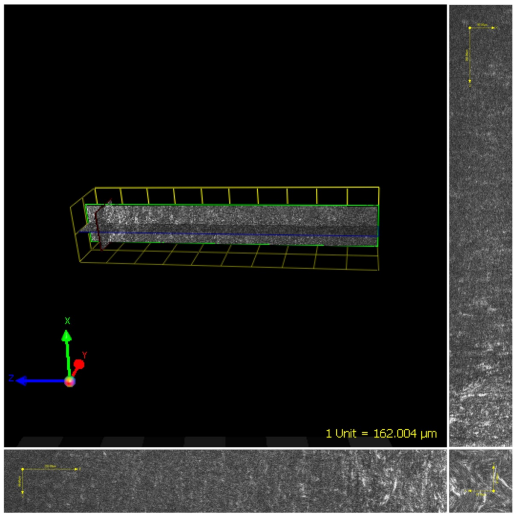

FIGURE 5.1.2. Picture of imaging through the whole thickness of a porcine cornea that has a thickness of nearly $2\,mm$. The picture shows that we are able to get pictures of structures that were deep in the tissue. The dimensions in x,y and z are $230.3\,\mu m \times 230.3\,\mu m \times 1614.5\,\mu m$, respectively.

tuned the laser to a wavelength of $890\,nm$ and used two channels with different bandpass filters. The trans-channel had a bandpass filter with $435\,nm - 485\,nm$ and the epi-channel had a bandpass filter with $500\,nm - 550\,nm$. As can be seen in figure 5.1.1 no disturbance by autofluorescence occurred. Next we checked how deep we were able to penetrate into the cornea with this imaging method. Figure 5.1.2 shows that we were able to image through the whole thickness of the porcine cornea, which can be up to $2\,mm$ thick. (The measured sample was $1.6\,mm$ thick)

The next thing to test was if it was second harmonic light, what we detected in the transmission photomultiplier. We had some clues that it should be second harmonic light. One clue was that we only got pictures in the transmission direction and nearly no signal in the epi-direction. Another was that there seemed to be no bleaching of the signal. So to determine if it really was a SH signal we had to do a test. The first test we performed was that we put a narrow bandpass filter in front of the transmission photomultiplier because if it really was SH light that we saw it should have exactly the half wavelength of the incident laser light. We tuned the laser to a wavelength of $880\,nm$ and put a narrow bandpass filter $440/10\,nm$ in the system. As can be seen in figure 5.1.3 image (A) we got an image. Then we changed the filter to $450/10\,nm$. Figure 5.1.3 image (B) shows that no image was detectable. Then we changed the wavelength of the laser to $900\,nm$. With this we got an image again (see figure 5.1.3 image (C)). So our first test was successful and we had very strong indications that what we saw was really second harmonics light and that it showed us the structure of the collagen fibrils in the cornea. But to get hard evidence we wanted to use antibody staining. By this we should be able to correlate the picture created by the second harmonic light and the picture of the fluorescence labeled antibodies which are docked to the collagen. But some problems occurred and because of these the results are not included in this work.

In order to do antibody staining we had to use another method of fixation than normally used with tissue. The literature said that antibody staining would not work properly if paraformaldehyde was used. The fixation method that was

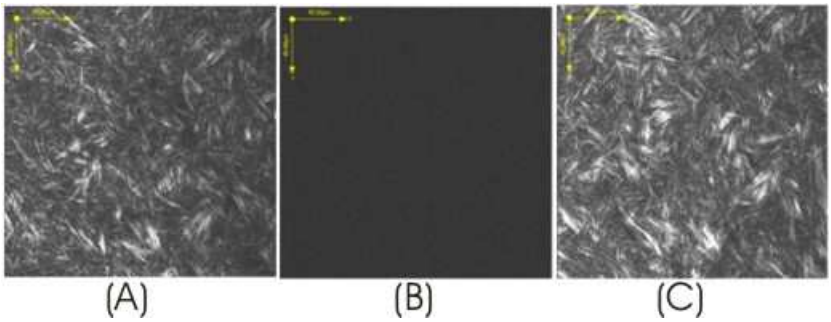

FIGURE 5.1.3. Picture (A) : Collagen structure with the laser tuned to 880 nm and a narrow bandpass filter 440/10 nm. (Dimensions [x,y] 230.3 μm × 230.3 μm) ; Picture (B) : Collagen structure with the laser tuned to 880 nm and a narrow bandpass filter of 450/10 nm in the beam path. As can be seen no structure was visible. (Dimensions [x,y] 230.3 μm × 230.3 μm) ; Picture (C) : Collagen structure with the laser tuned to 900 nm and a narrow bandpass filter 450/10 nm. (Dimensions [x,y] 230.3 μm × 230.3 μm)

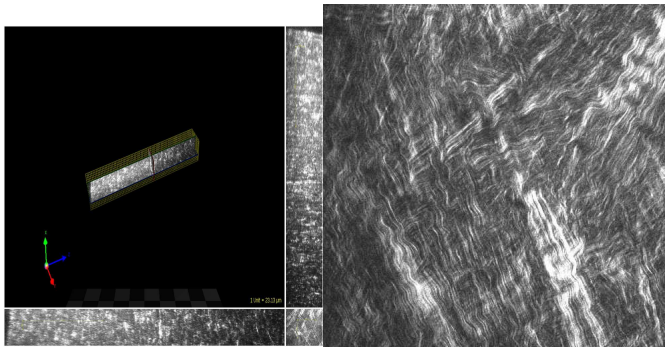

FIGURE 5.1.4. An unfixed cornea for comparison because a new fixation method was tested. (Dimensions of the stack picture (left side) [x,y,z] 230.3 μm × 230.3 μm × 1760.2 μm); dimensions of the right side picture are [x,y] 230.3 μm × 230.3 μm)

recommended was with acetone. So we made a test if the fixation with acetone somehow changes the SH signal. As can be seen in the figures 5.1.4 and 5.1.5 the fixation method did not change our signal.

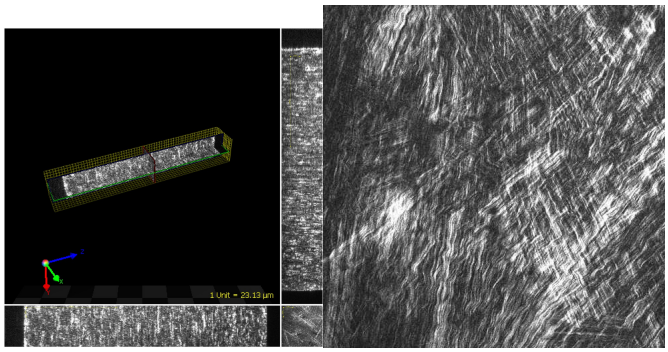

FIGURE 5.1.5. A cornea fixed with acetone at about 0 degrees centigrade for about 20 minutes. No changes in the structure are visible. So fixation with acetone is also possible. (Dimensions of the stack picture (left side) [x,y,z] $230.3\,\mu m \times 230.3\,\mu m \times 1537.6\,\mu m$); dimensions of the right side picture are [x,y] $230.3\,\mu m \times 230.3\,\mu m$)

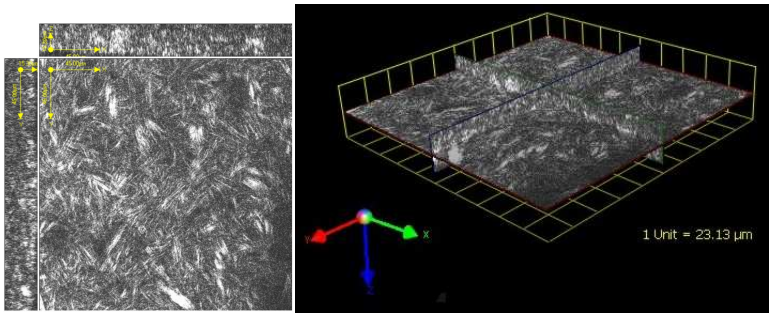

FIGURE 5.1.6. Unfixed porcine cornea as a reference against possible changes due to fixation of the cornea with paraformaldehyde. (Dimensions [x,y,z] $230.3\,\mu m \times 230.3\,\mu m \times 29.5\,\mu m$)

But for normal use we wanted to fix the sample with paraformaldehyde because the samples become more stable than with acetone. Also formalin fixation is a standard procedure for tissue conservation and so the effects are well known. We decided against using glutardialdehyde because it shows autofluorescence. So after finding that SH imaging was possible with the microscope setup and the positive test results concerning the SH signal we started with a test series to determine if fixation with paraformaldehyde changes the SH image in any way. The figures 5.1.6 to 5.1.9 show an unfixed porcine cornea, a porcine cornea fixed with a 4% solution of paraformaldehyde for 10 minutes, a porcine cornea fixed with a 4% solution of paraformaldehyde for 30 minutes and a porcine cornea fixed with a 4% solution of paraformaldehyde for 120 minutes (in this order). As can be seen the signal does not change due to treating the cornea with the fixer. The changes that were observable resulted from using different corneas and by this also imaging different areas of the corneas. We also had a sample available that was immersed in commercial formaldehyde solution for about five weeks. As can be seen in the figure 5.1.10 the second harmonic signal is not destroyed also there was a certain possibility for that because of the fact that formaldehyde dissociates in methanol and formic acid according the formula in figure 5.1.11. The dissociation process is an equilibrium process so to keep the formic acid level low the manufacturer

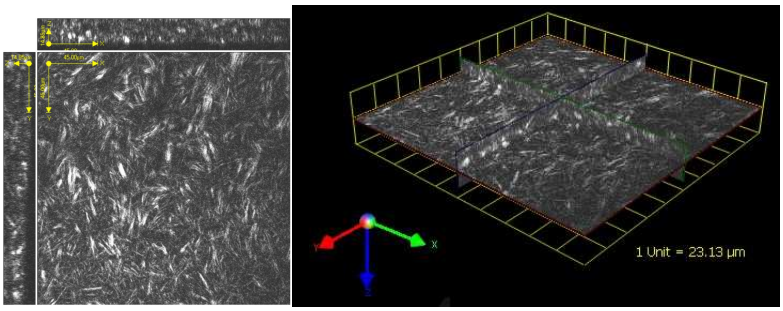

FIGURE 5.1.7. Porcine cornea fixed with paraformaldehyde for 10 minutes. No changes in the second harmonic signal compared to the reference picture are visible. The changes in the structure are based on the use of another cornea sample. (Dimensions [x,y,z] $230.3\,\mu m \times 230.3\,\mu m \times 28.7\,\mu m$)

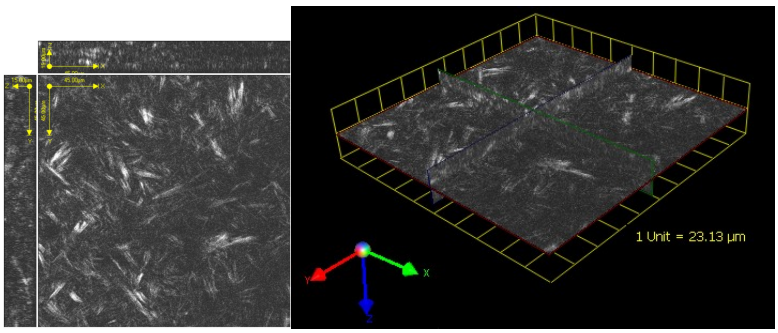

FIGURE 5.1.8. Porcine cornea fixed with paraformaldehyde for 30 minutes. Also no changes. As before a new cornea was used which accounts for the structural changes visible. (Dimensions [x,y,z] $230.3\,\mu m \times 230.3\,\mu m \times 29.1\,\mu m$)

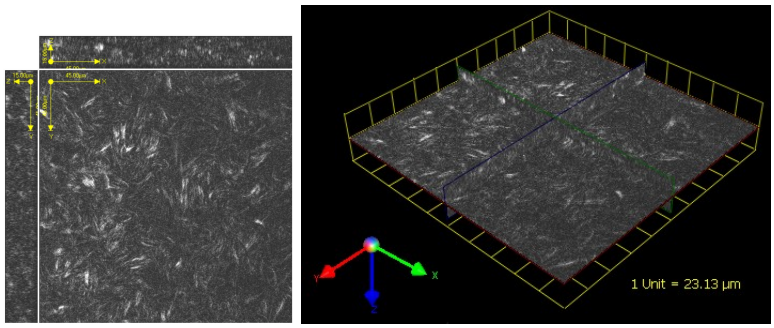

FIGURE 5.1.9. Porcine cornea fixed with paraformaldehyde for 120 minutes. The same conditions as in the pictures before were used. (Dimensions [x,y,z] $230.3\,\mu m \times 230.3\,\mu m \times 29.1\,\mu m$)

sometimes puts methanol in to change the equilibrium. The methanol may also have disturbed the SH signal.

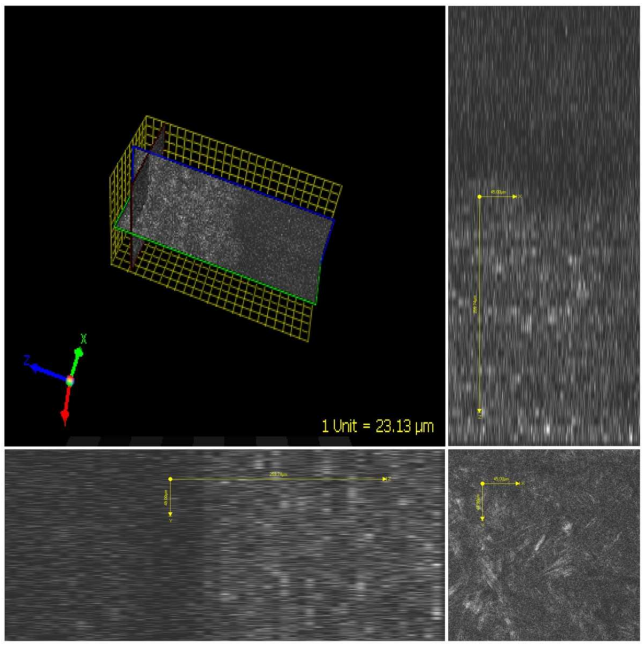

FIGURE 5.1.10. Porcine cornea fixed in commercial formalin for about five weeks. As can be seen even this treatment does not affect the SHG. (Dimensions [x,y,z] $230.3\,\mu m \times 230.3\,\mu m \times 519.3\,\mu m$)

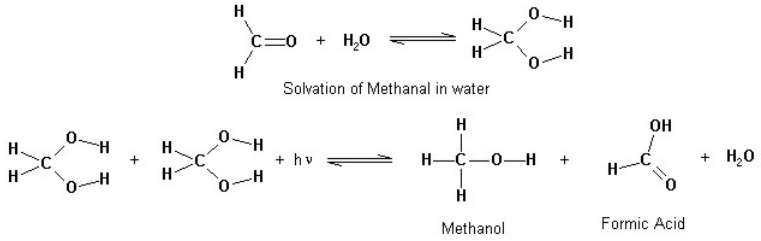

FIGURE 5.1.11. Dissociation of Formalin

5.2. Laser cutting experiments

After these preliminary test, we began to treat the corneas with the fs – laser. By thinking about this we found another problem we had not considered until then. Because we wanted to "burn" holes into the stroma we had to think about a way to discern between cells, which show up in the second harmonic image as dark holes, and the cavities produced by the laser. (figure 5.2.1 shows the cavities produced by the laser). So we tried using fluorescence dyes to label some structures in the cornea. With DAPI we were able to stain the nuclei of the cells in the cornea (figure 5.2.2) and we tried to stain actin fibers with phalloidin-FITC (figure 5.2.3). As can be seen in figure 5.2.2 the DAPI was able to penetrate even an unpermeabilized cornea if it has enough time. The phalloidin-FITC on the other hand seemed to work only on the surface as the images in figure 5.2.3 show. Because of the size of the phalloidin-FITC we used a 0.1% Triton X-100 solution in PBS to permeabilize the fixed corneas (time of permeabilization: 30 min). Even after permeabilization, which disturbed the structural order of the collagen slightly, the phalloidin-FITC

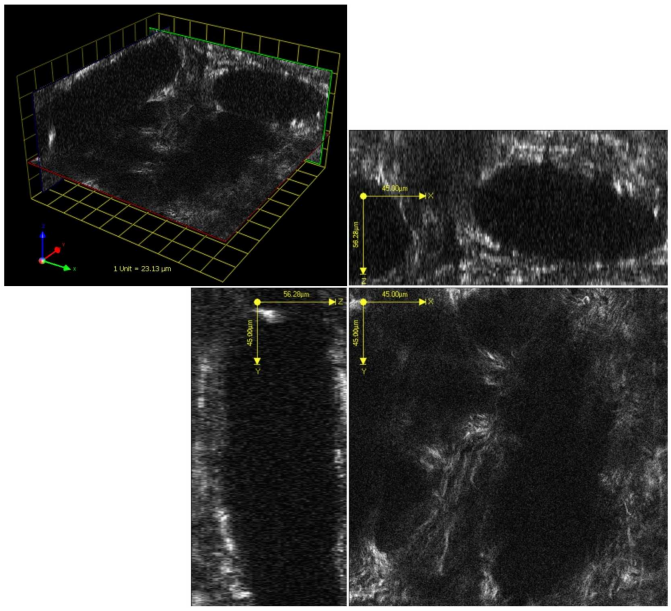

FIGURE 5.2.1. The image shows a picture of the cavities produced by the laser treatment. The cavities have a diameter of about $20\,\mu m$. (Dimensions [x,y,z] $230.3\,\mu m \times 230.3\,\mu m \times 110.5\,\mu m$)

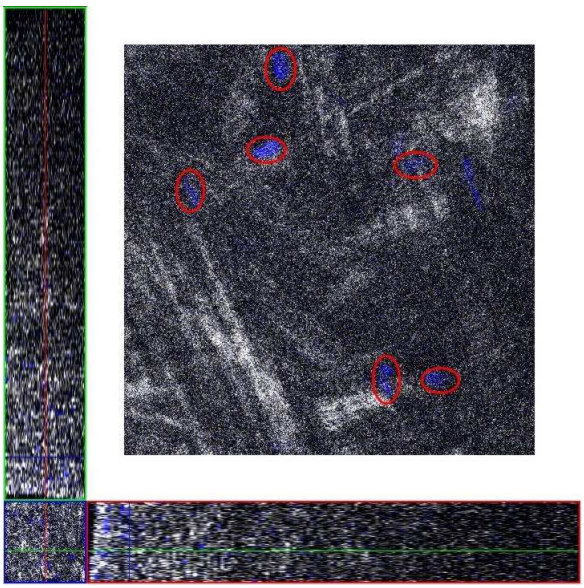

FIGURE 5.2.2. Stack image of an unpermeabilized cornea stained with DAPI and phalloidin-FITC over night in PBS. The red circles mark some of the DAPI stained cell nuclei which are colored blue in this picture. The collagen fibers are shown in white. (Dimensions [x,y,z] $230.3\,\mu m \times 230.3\,\mu m \times 1423.1\,\mu m$)

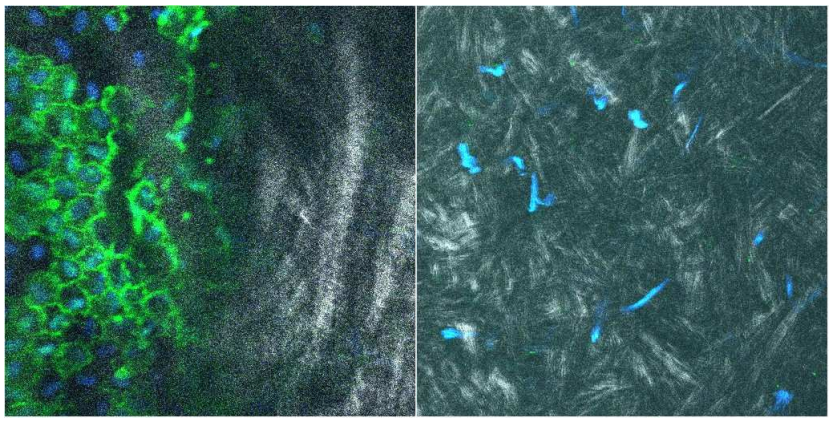

FIGURE 5.2.3. Images of a cornea stained with DAPI and phalloidin-FITC. The left one was taken from the surface (as far as this is possible with a bend object). The curvature of the sample is responsible for the look of the picture; this means that on the left side of the picture we are already on the surface while on the right side we are still a little bit beneath the surface, which is why we can see some blurry collagen structures. The right picture was taken from inside the cornea. The nuclei are colored blue, the collagen fibers are colored white and the actin fibers are colored green. In the left picture the polygonal structure of the endothelial cells can be seen. (Dimensions [x,y] 230.3 μm × 230.3 μm respectively)

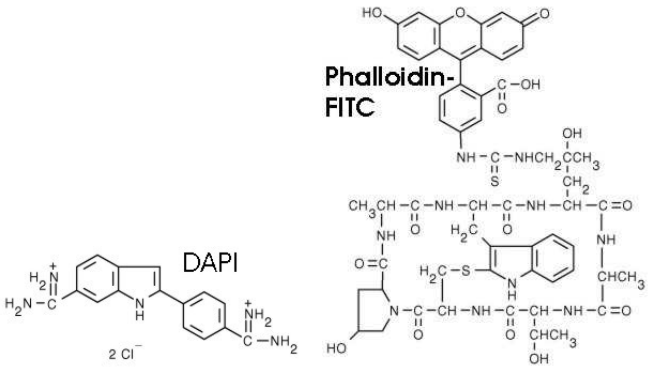

FIGURE 5.2.4. These pictures show the molecular structure of DAPI and phalloidin-FITC respectively.

did not stain anything inside the cornea sample. This could mean two different things:

- The phalloidin was not able to penetrate the cornea tissue even after permeabilization with Triton X-100 (which is highly likely because of the size of the molecule) (see figure 5.2.4 for the structural formulas of DAPI and phalloidin-FITC).
- There is no actin in the cornea present so no staining could occur in deeper layers of the cornea.

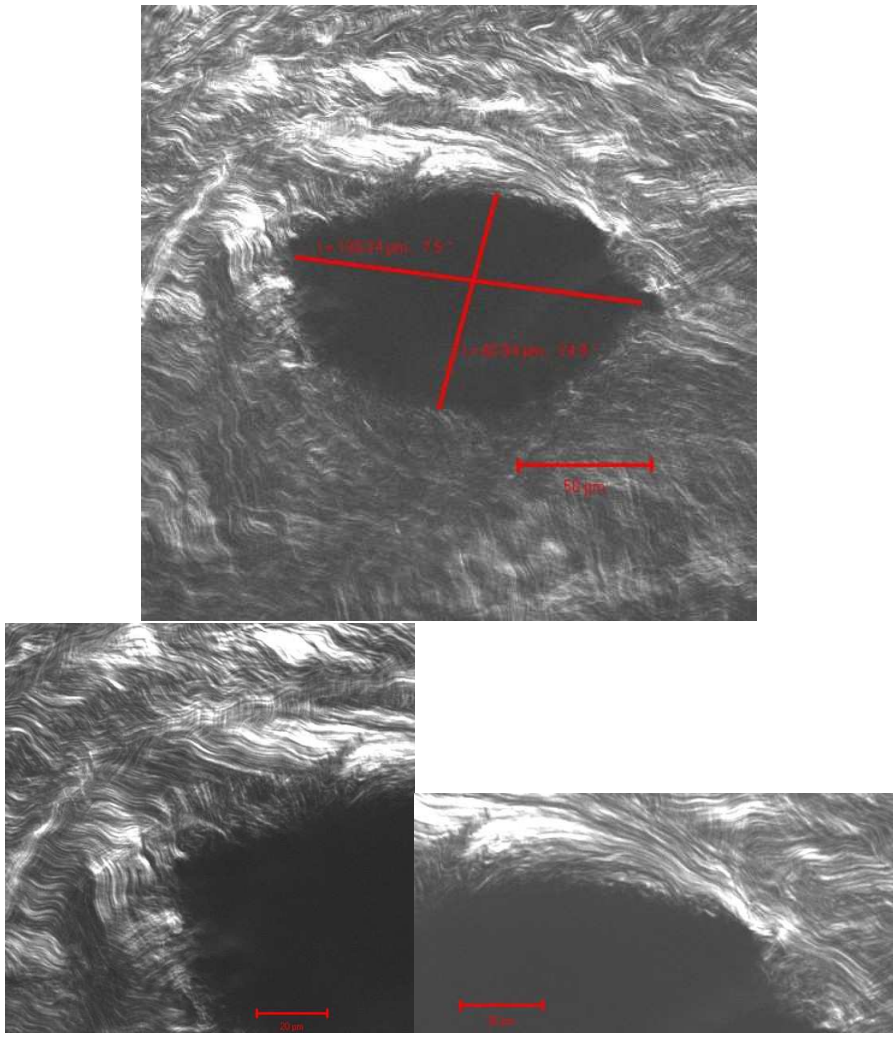

FIGURE 5.2.5. These images show a cavitation bubble. In the even more magnified images of the border regions of this bubble it is visible that the collagen is not coagulated by heat.

Because of these two possibilities which we were not able to rule out we stopped using phalloidin-FITC and permeabilization with Triton X-100. Also the use of DAPI was enough for our purpose because the nuclei of the cells were labeled and by that way we were able to distinguish between cavities produced by the laser treatment and cells that give no second harmonic signal.

Because we were interested in the shape of a cavity and the order of the collagen fibers in the neighborhood of a cavity we made a magnified image of a cavitation bubble. (figure 5.2.5) As can be seen the collagen is not coagulated by heat which was to be expected because of the laser – tissue interaction that occurs. In another image of a single cavitation bubble relaxation of some collagen fibers in the upper part of the image was visible. (figure 5.2.6)

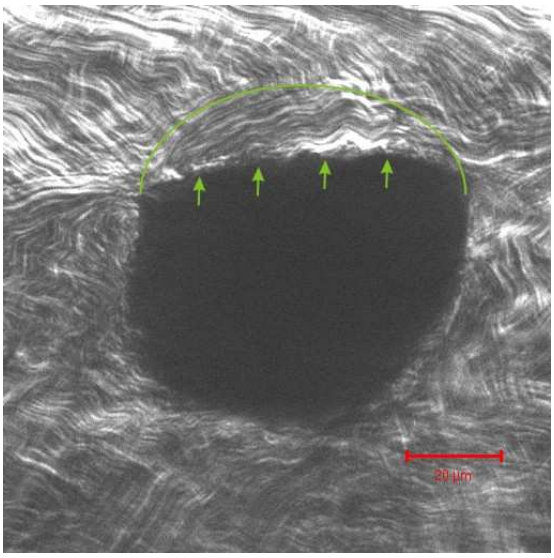

FIGURE 5.2.6. This magnified image shows another cavitation bubble. In the upper part of the image it can be seen that the collagen fibers relaxed into their natural position after being displaced by the pressure wave that formed the bubble (denoted by the green arc and the green arrows).

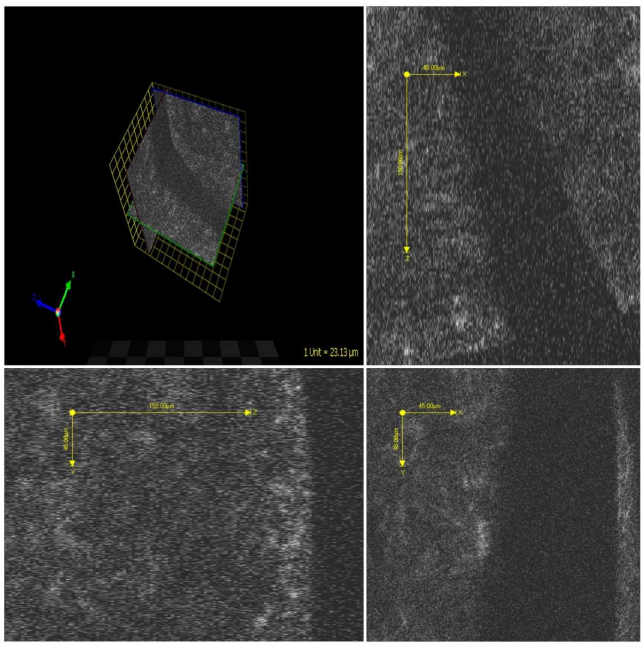

FIGURE 5.2.7. Stack image of a part of the ring cut into the cornea. (Dimensions [x,y,z] 230.3 μm × 230.3 μm × 300.1 μm)

After these experiments we started with an easy to produce geometric cutting figure. First we cut a ring from the surface into the stroma. Figure 5.2.7 shows a stack image of the ring cut. The following pictures (in figure 5.2.8) show single high resolution scans of different parts of the ring at different depths from the surface.

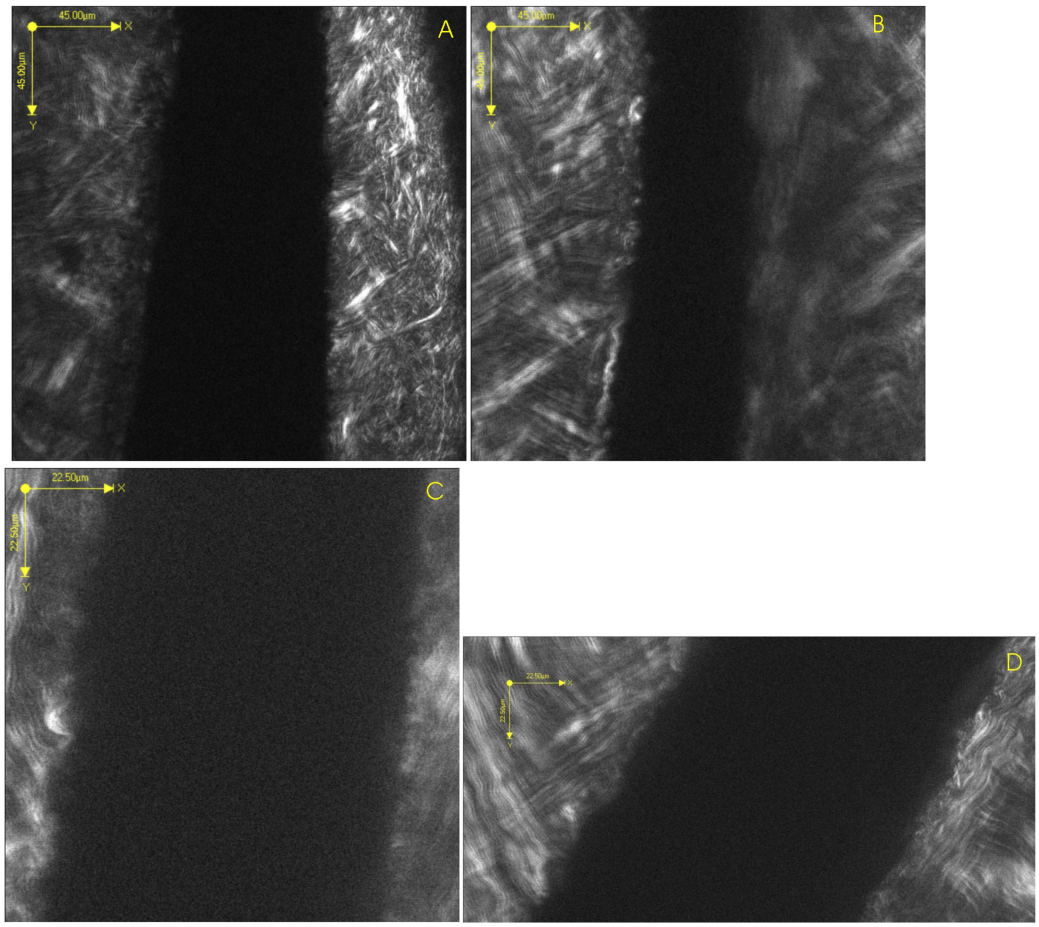

FIGURE 5.2.8. Pictures of the ring cutting at different depths from the surface and different parts of the cornea. Scanned at high resolution. Picture A: Dimensions [x,y] 230.3 μm × 230.3 μm at the surface; picture B: Dimensions [x,y] 230.3 μm × 230.3 μm at a depth of 200 μm from the surface; picture C: Dimensions [x,y] 115.2 μm × 115.2 μm at a depth of 200 μm from the surface at the same position as picture B but with zoom factor 2; picture D: Dimensions [x,y] 115.2 μm × 115.2 μm at a depth of 200 μm from the surface but at a different section of the cornea. The smoothness of the edges of the cut is very good and also it is discernible that the collagen fibrils were not coagulated by heat.

As can be seen on these high resolution scans the edges of the cut are smooth and the collagen fibers are not coagulated by heat as was already determined before. After this we changed the lateral spacing of the laser spots. The result can be seen in figure 5.2.9. As the picture shows the cutting quality is very good at the surface but decreases with depth. This was one problem we encountered early in our experiments because the control software of the laser application system was optimized for other tasks than the ones we performed with it. (The software was designed for flap cutting at first)

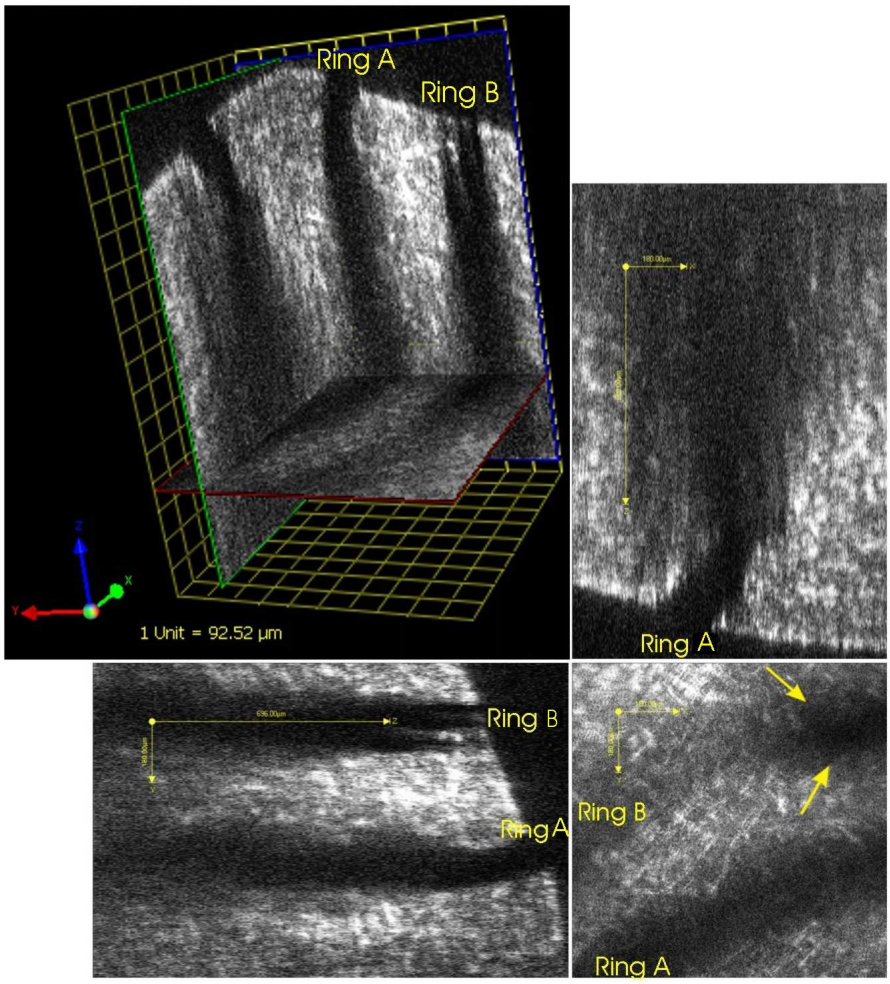

FIGURE 5.2.9. Stack image of a part of two ring cuts. The laser energy was set to $3\,\mu J$. The lateral spacing of the laser spots was varied. Ring A has a spot spacing of $10\,\mu m$; Ring B has a spot spacing of $20\,\mu m$. As can be seen the cutting quality of ring B is not as good as it is in ring A. It is nearly possible to recognize the impact point of the laser in ring B (see arrows). The bend at the surface of ring A is likely the result of applicating force to the cornea by the "contact lens" that was used in the laser delivery system and by that flatten it in the middle. So in the relaxed cornea a formerly straight cut is bend. (Dimensions [x,y,z] $921.4\,\mu m \times 921.4\,\mu m \times 1384.5\,\mu m$)

After getting these results we started with cutting flaps. The flaps had some big advantages compared to using the whole corneas for imaging. It was much easier to image through the whole thickness of the flap because the thickness was well defined, much thinner than an original cornea and also the problem of possible artifact production while removing the corneas was circumvented. The flaps where produced by scanning the laser intrastromal in a spiral pattern. This spiral pattern can be seen in figure 5.2.10 which shows an artificial cornea. So the cavities produced by the laser do not collapse due to the stiffness of the material. The next

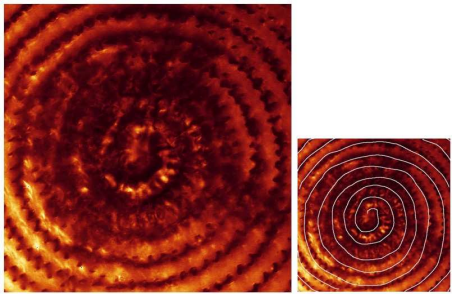

FIGURE 5.2.10. A picture taken with the Leica confocal microscope of an artificial cornea to show the spiral pattern of the scanning of the laser used to create the flap bed. (In the small picture the spiral pattern is denoted by the white line) (Dimensions [x,y] $1500\,\mu m \times 1500\,\mu m$)

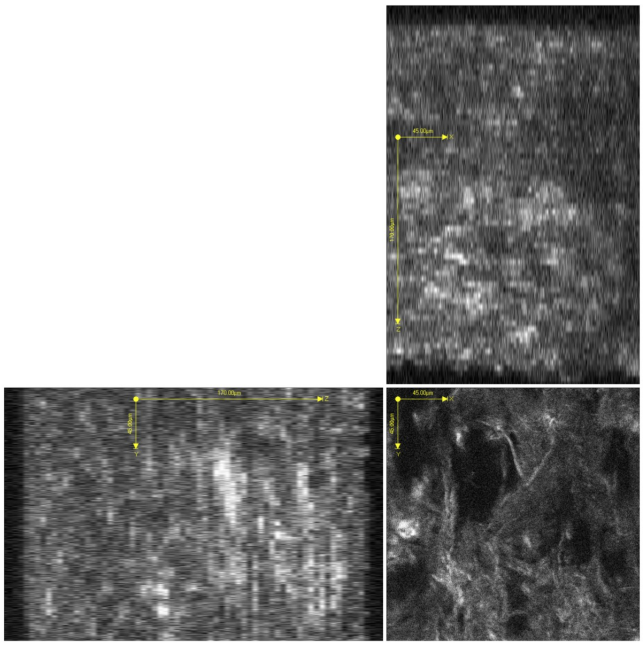

FIGURE 5.2.11. The picture shows a stack image of the flap which is lying upside down while imaging. As can be seen the flap bed is smooth but not to smooth to make it difficult to place it back after the LASIK operation and to inhibit wound healing afterwards. The roughness is about $20\,\mu m$ (Dimensions [x,y,z] $230.3\,\mu m \times 230.3\,\mu m \times 340.1\,\mu m$)

step after creating the flap bed was a ring cut that went up to the surface. After this the flap could be removed easily. In a LASIK operation the flap would be left connected to the cornea via a small hinge but for our purposes we did not create a hinge. Figure 5.2.11 shows a stack image of the flap and figure 5.2.12 shows a high resolution image of the roughness of the flap bed which is as small as we hoped it would be.

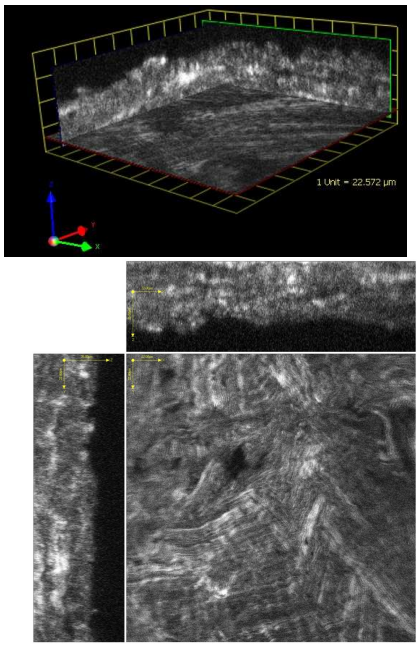

FIGURE 5.2.12. This picture shows a high resolution stack image of the flap bed. The roughness of the flap bed surface is about $20\,\mu m$. (Dimensions [x,y,z] $230.3\,\mu m \times 230.3\,\mu m \times 70.1\,\mu m$)

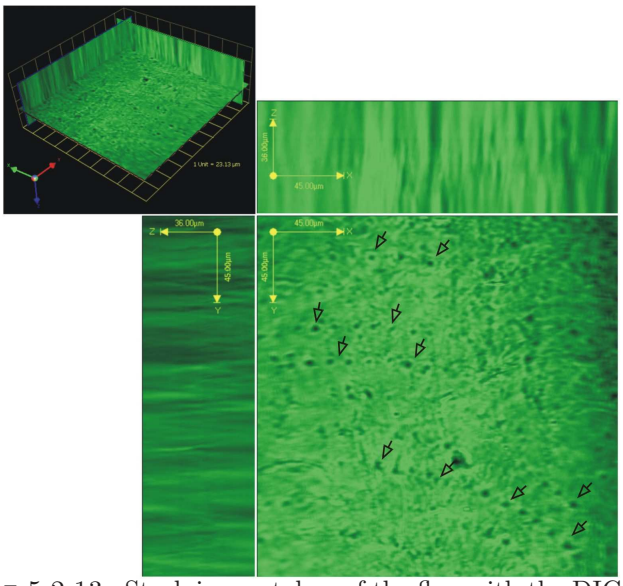

FIGURE 5.2.13. Stack image taken of the flap with the DIC mode of the microscope. A spiral patterned track of holes are visible (see arrows). The depth of these holes varies from $40\,\mu m$ to $70\,\mu m$. (Dimensions [x,y,z] $230.3\,\mu m \times 230.3\,\mu m \times 69.9\,\mu m$)

After these SH images of the flap we made a DIC image (*D*ifferential *I*nterference *C*ontrast) of it with the DIC mode of the Zeiss microscope. To our surprise we saw a spiral patterned damage track from the laser. So we made a stack image

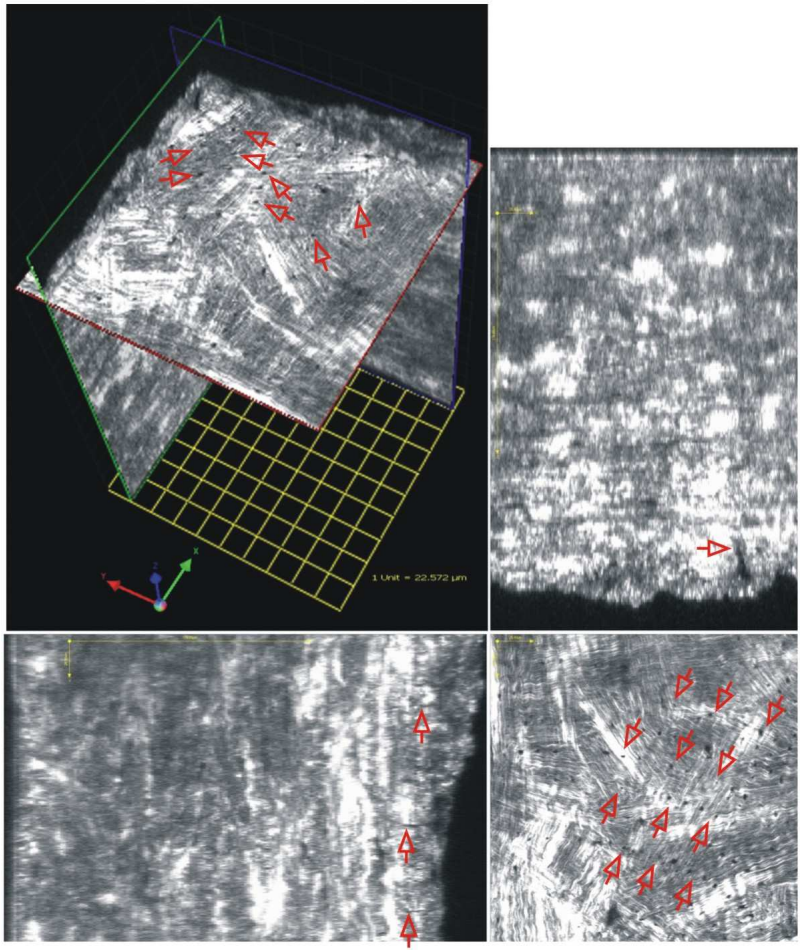

FIGURE 5.2.14. Second harmonic stack picture from the same sample as the DIC picture. The streaks are clearly visible (some are marked with red arrows). (Dimensions [x,y,z] $230.3\,\mu m \times 230.3\,\mu m \times 352.2\,\mu m$)

with visible light of this phenomenon. (figure 5.2.13) After this we had a closer look at the same area with SH imaging. In the SH picture we found those holes or streaks also (figure 5.2.14). We made also a high magnification image of two of those streaks and had a look at their diameter (figure 5.2.15). The result was that they had a diameter of approximately $2\,\mu m$ to $3\,\mu m$. Figure 5.2.16 suggested that those streaks were really ablated tissue and not some change in the collagen which inhibited the generation of the SH signal. But we also had the suspicion that the streaks had an extension in the z – direction.

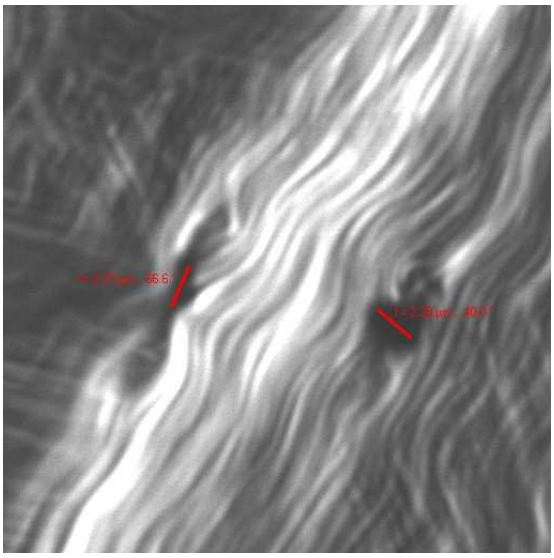

FIGURE 5.2.15. A picture of two streaks. It can be seen that they have an approximate diameter of about $2.3\,\mu m$. (Dimensions [x,y] $28.8\,\mu m \times 28.8\,\mu m$)

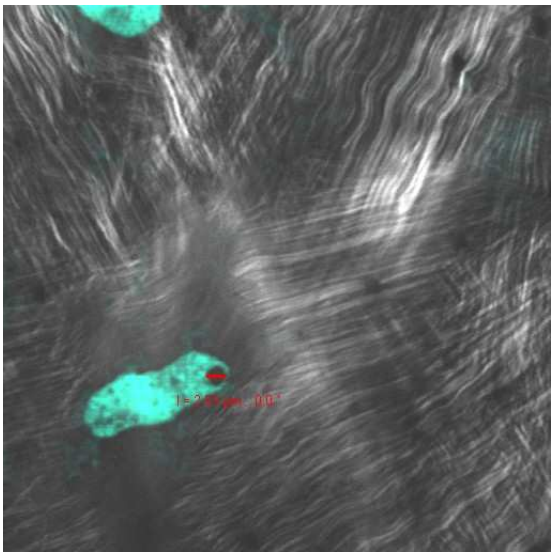

FIGURE 5.2.16. This image seems to proof that the streaks are ablated tissue because here can be seen a streak which penetrates a nucleus. The nucleus was stained with DAPI before imaging but after the laser treatment. (Dimensions [x,y] $76.8\,\mu m \times 76.8\,\mu m$)

This gave us a new problem, how to measure the extend of those streaks in both directions from the cutting plane. The solution was simple we had to make an intrastromal cut in a flap. By doing this we had all the advantages of the flap and also the possibility to image the full extension of the streaks. So we made a stack image of an intrastromal cut in a flap. For the images of these streaks we changed our routine from measuring the samples upside down to measuring them upside up. This we did because we wanted to avoid the streaks that may have been

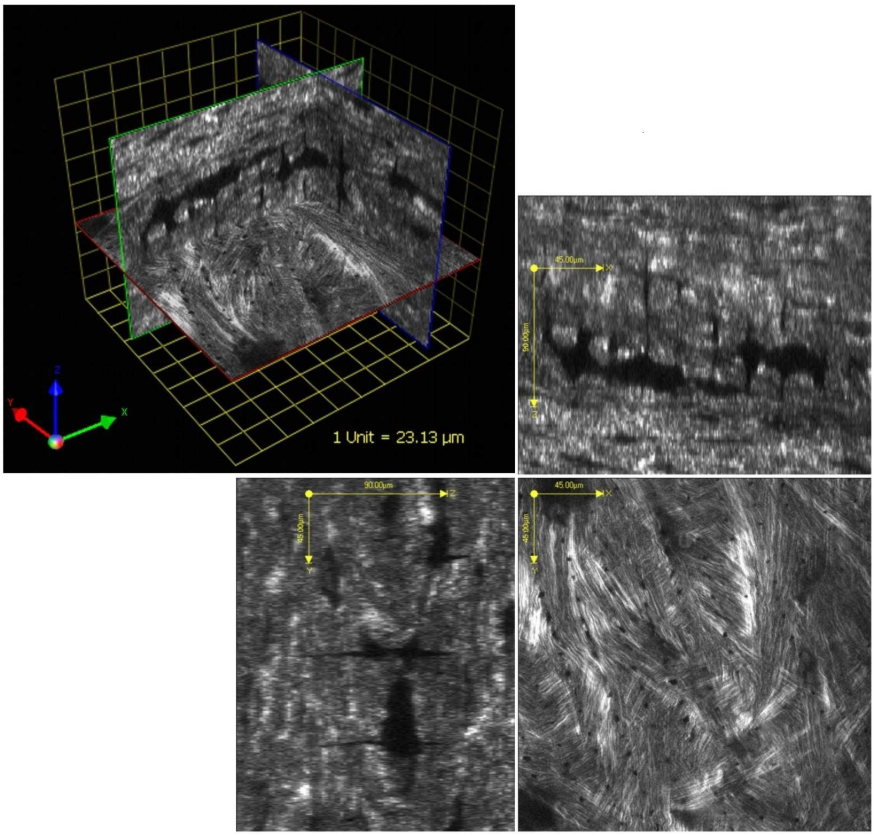

FIGURE 5.2.17. In the image can be seen that the streaks start above the level were the cavities are produced by the laser and that they continue beyond that level. It also shows that they correspond to the damage tracks we have seen in the other pictures. (Dimensions [x,y,z] 230.3 μm × 230.3 μm × 180 μm)

produced by cutting the flap bottom. Also it was no longer necessary to turn them upside down because the flap bed was a smooth plane (figures 5.2.17 and 5.2.18). Those streaks came totally unexpected especially their length. There could be two different causes for those streaks:

- self-focusing of the laser due to its power. (this thesis was aided by the diameter of the streaks; the laser beam has a diameter of 5 μm at its focal point)
- a long focus due to the fact that in the delivery system of the laser beam a lens with low numerical aperture was used.

The streaks could also be a result of a combination of the two effects. The lens in the delivery system was designed to enable the delivery system to reach all points of a circle with radius of more than 1 cm without movement of the delivery system. So if the lens is the problem the laser delivery system has to be redesigned to take this into account. Because of this we could not exchange the lens easily so we made an energy series and also changed the profile of the laser beam by blocking some parts of it.

The energy series revealed that by lowering the energy the quality of the flap cutting decreased. But to get a connected cutting plane we had to decrease the distance between the laser spots. This resulted in a slowdown of the treatment

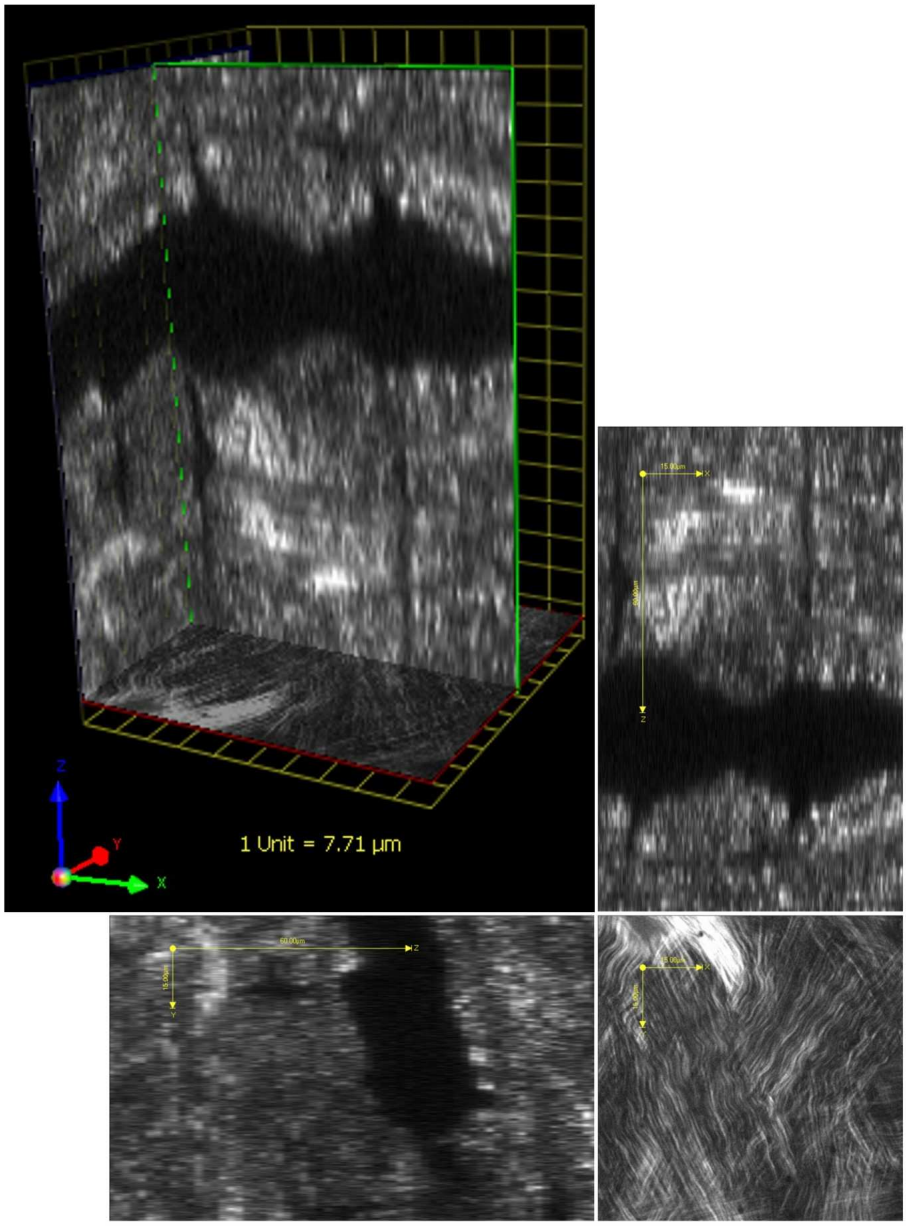

FIGURE 5.2.18. In this image an enlarged part of a intrastromal cut can be seen. The streaks are clearly visible and as can be determined form the picture have a total length of about $100\,\mu m$. (Dimensions [x,y,z] $76.8\,\mu m \times 76.8\,\mu m \times 120.0\,\mu m$)

speed which may cause problems with the correct alignment between the eye and the application unit. So we made some experiments in which we changed the profile of the laser by using a beam block to block the inner parts of the laser beam and an aperture to block the outer parts. By this we hoped to be able to eliminate the long focus of the lens as a cause for the streaks. The result for the beam block was not good as could be expected from the fact that by blocking the inner part of the beam we blocked about 50 % of the total laser power. The laser produced no cavities which made it impossible for us to locate any streaks. With the aperture

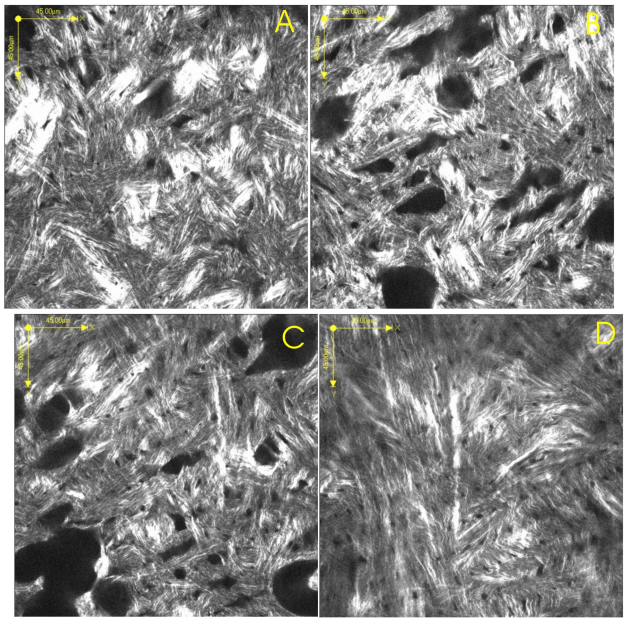

FIGURE 5.2.19. These images show the cornea after laser treatment at different depth form the surface. The cornea was lying upside up and an aperture in the beam pass was used to block the outer parts of the laser beam. The energies used were $5\,\mu J$ for cutting the flap and $4\,\mu J$ for the intrastromal cut. Picture A shows the cornea at a depth of $60\,\mu m$ from the surface; picture B at a depth of $80\,\mu m$; picture C at a depth of $100\,\mu m$ and picture D at a depth of $140\,\mu m$. As can be seen the streaks are still visible so blocking the outer parts does not help. (Dimensions [x,y] $230.3\,\mu m \times 230.3\,\mu m$)

the outer parts of the beam were blocked. As can be seen in figure 5.2.19 with this arrangement there were still streaks. Figure 5.2.20 shows a stack image of a cornea sample that was treated in the same way as was the sample from figure 5.2.19.

Because of these results the question of the cause of the streaks can not be answered right now. There are further experiments needed to give a final answer. The next step may be to use a microscope objective in the beam application system and to redo the experiments with the beam stop and the aperture. By this it should be possible the see if the lens is the problem.

As can be seen second harmonic microscopy is a very good and easy to use method for evaluation of the laser treatment of corneas.

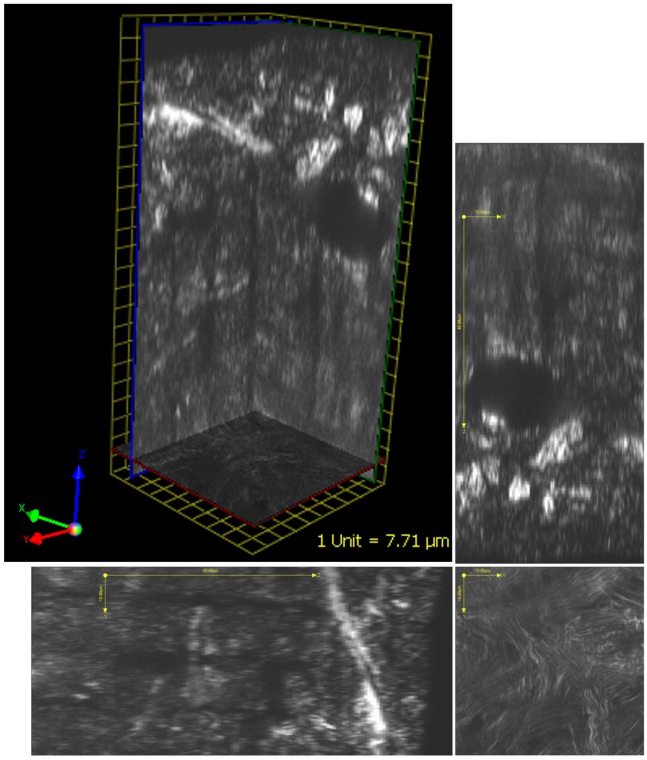

FIGURE 5.2.20. This stack image shows that the streaks are not only visible but have also nearly the same length as in the images of cornea samples that were lased without a aperture. (Dimensions [x,y,z] $76.8\,\mu m \times 76.8\,\mu m \times 170.2\,\mu m$)

CHAPTER 6

Atomic Force Microscope Measurements

We wanted to try to use the AFM to measure the changes in cornea thickness due to intrastromal ablation. We also hoped to obtain more information about those streaks we observed in the SH pictures. The first problem we encountered was to mount any sample to the metal pucks necessary for the scanner of the Digital Instruments MultiMode microscope. We first tried to use super-glue to fix a whole cornea to the metal puck. The result was not very encouraging because the solvent of the super-glue changed our cornea that much that these changes in the surface structure and the collagen fibers were observable by the naked eye and the sample was rendered totally useless. So we had to find another method to fix the cornea on the metal puck. Our next idea, inspired by a paper from Lydataki et al. **[40]**, was to fix the cornea mechanically. By using the specially designed liquid tight chamber shown in figure 6.0.1 we were able to obtain our goal.

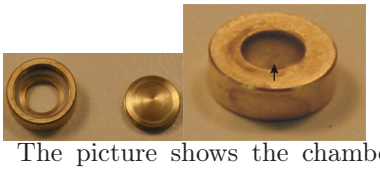

FIGURE 6.0.1. The picture shows the chamber that was designed to scan punched out pieces of the cornea. In the left picture (marked with the arrow) a cornea is fixed in the chamber and ready for scanning.

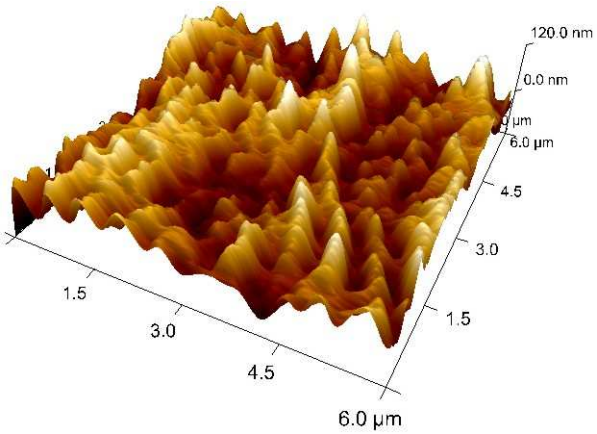

FIGURE 6.0.2. 3D picture of the surface of a pig cornea (without epithelium). The epithelium was removed because it was damaged in the process of slaughtering of the animal in the slaughterhouse. As can be seen the cornea surface is rather rough. The image was obtained with the AFM in tapping mode in fluid.

The first picture we made with this chamber was that of a cornea fixed with PFA and scanned on the front surface. Figure 6.0.2 shows a 3D picture of this scan. There can be seen that the surface of the cornea is rather rough. But to get information about thickness changes due to tissue ablation the thickness of a native cornea was too non-uniform. So we had to slice the cornea. This was the second problem that occurred. First we tried the embedding and slicing process used for transmission electron microscopy but that did not work. The slices that were produced were all right but the fact that we wanted to have a look at these slices also with SH imaging rendered this process useless, because the used embedding material gave a strong autofluorescence signal and the SHG capability of the collagen was somehow destroyed in the dehydration and contrast magnification process. So we tried using cryosectioning. This seems to be the method we were looking for because the SHG capability of the collagen was not hampered as we tested with the LSM. And also the fibers did not seem to be dislocated. The figures 6.0.4 and 6.0.3 show AFM images of a cornea slice with a diameter of about $2\,mm$ and a thickness of $22.5\,\mu m$. The slice was put on a microscope slide and left to dry in the air so we could measure the alignment of the collagen fibers more easily. "Glue" was not necessary for this because the slice was adhering strongly enough to the microscope slide in its dry state.

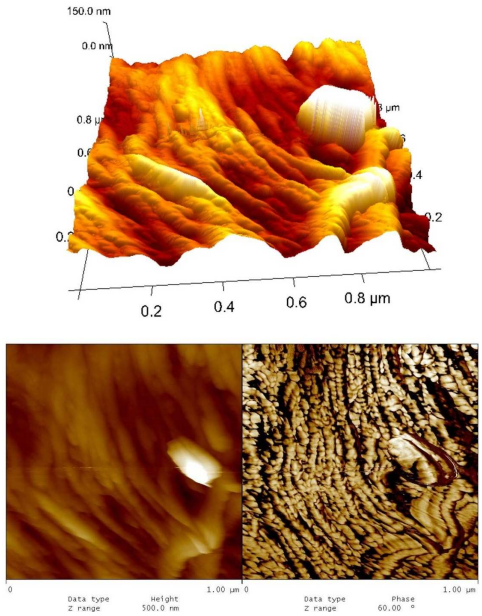

FIGURE 6.0.3. AFM images of a dry cornea slice (dimensions: diameter $2\,mm$; thickness $22.5\,\mu m$) with the AFM in tapping mode with different resolutions. The cantilever we used was from Veeco NanoProbe Tips (Model#: RTESP7). Especially in the Phase picture the orientation of the collagen fibers can be seen.

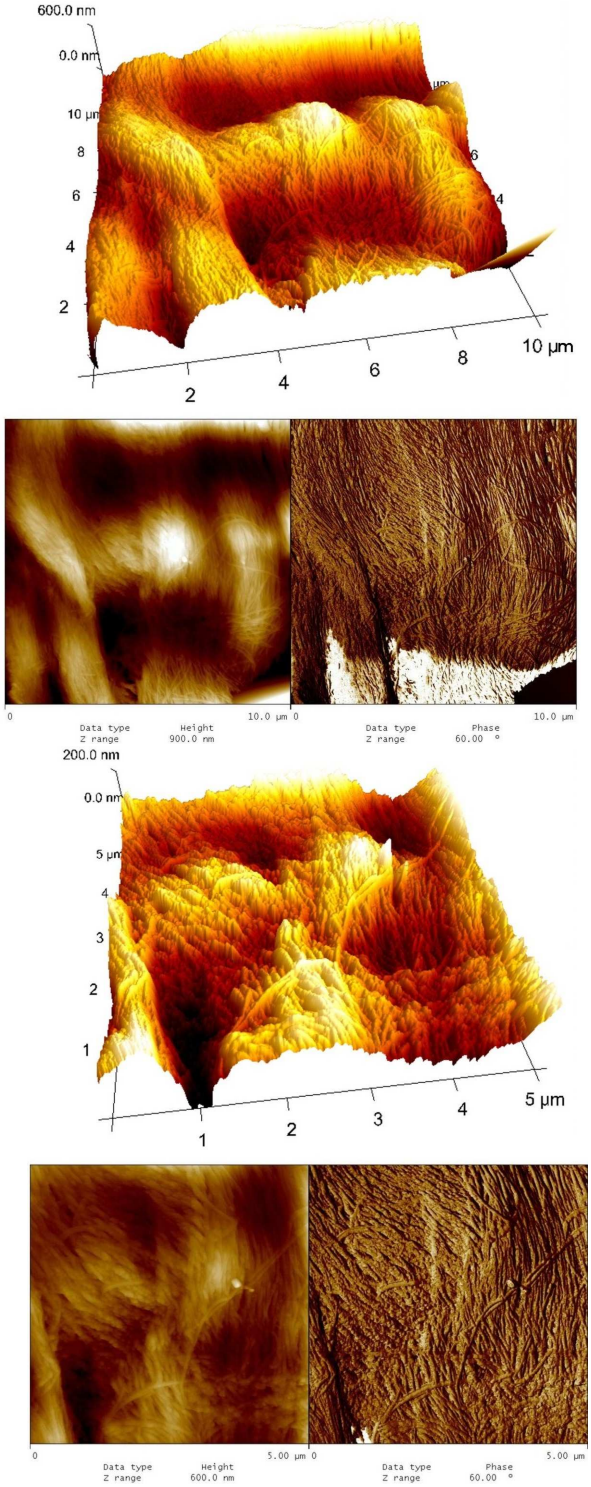

FIGURE 6.0.4. AFM images of a dry cornea slice (dimensions: diameter $2\,mm$; thickness $22.5\,\mu m$) with the AFM in tapping mode with different resolutions. The cantilever we used was from Veeco NanoProbe Tips (Model#: RTESP7). Especially in the phase picture the orientation of the collagen fibers can be seen.

The next thing we imaged was the backside of a flap cut with the laser. In the second harmonic image of this flap no streaks were visible. Figure 6.0.5 shows

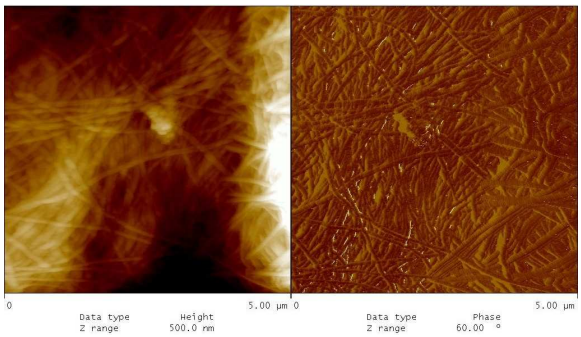

FIGURE 6.0.5. The image shows the height and the phase image of the flap separately. As can be seen the phase image reveals even more information about the sample. (The images are not processed in any way)

the alignment of the collagen fibers of a square-section of $5\,\mu m$ edge length. By subtracting the height and the phase images and making a plane fit the image gets clearer.

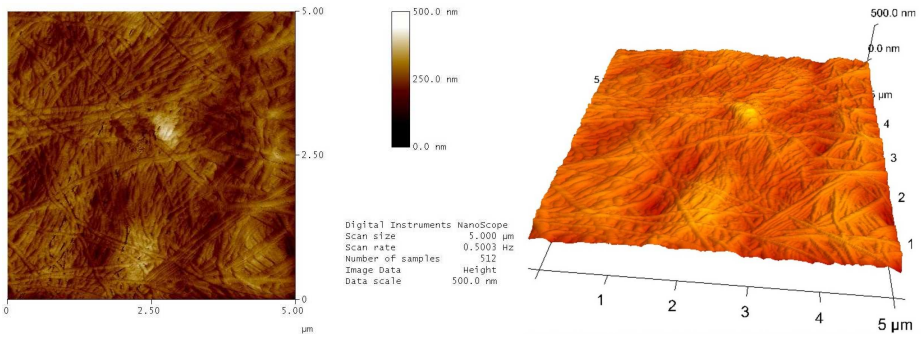

FIGURE 6.0.6. The left image was produced by subtracting the images from figure 6.0.5 from each other and then making a plane fit of third order in x and y direction. The collagen fibers are now clearly discernible and also a fine pattern on each fiber is visible. The right image is a 3D projection of the data in the left image.

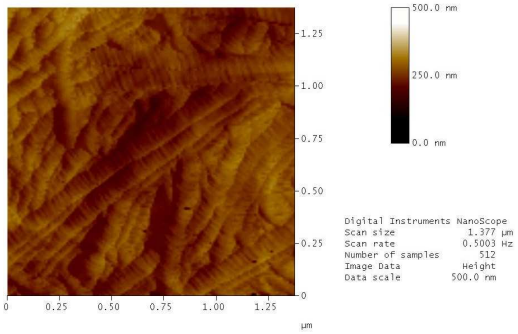

FIGURE 6.0.7. This image is a zoom of the image in figure 6.0.6. Now the pattern on the collagen fibers is easily visible. It has a strong resemblance to the pictures of collagen taken with a transmission electron microscope.

This was done in the images in figure 6.0.6 and figure 6.0.7. Figure 6.0.8 shows a square-section of $10\,\mu m$ edge length of the flap sample to give a broader view of the cornea. The image was treated like the one in figure 6.0.6. Because of the

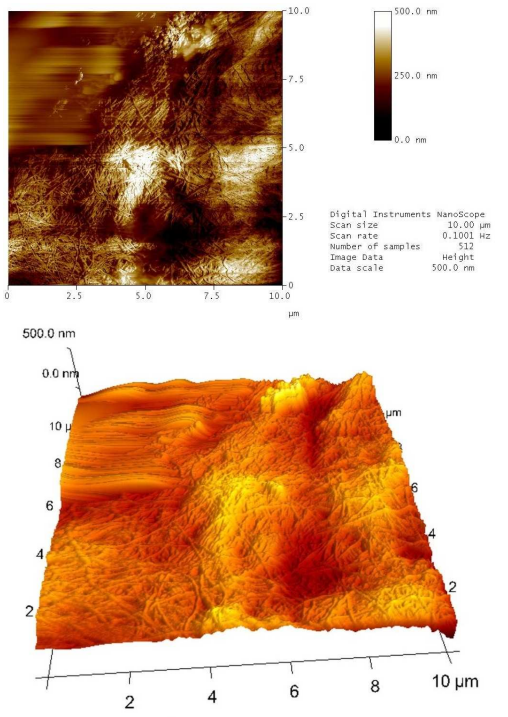

FIGURE 6.0.8. The upper image was produced by subtracting the original images from each other and then making a plane fit of third order in x and y direction. The feature in the upper left corner of the image may be due to a left over water droplet. The lower image is a 3D projection of the data in the upper image.

likeness of the phase image to images of collagen fibers taken with the transmission electron microscope we took a closer look at the phase image and made some evaluations with the tools of the NanoScope Software. For this the images were

left in the same state as they were measured only the parts that were measured were zoomed. The fibrils on which the measurements were performed were chosen randomly. With the "Section Analysis" tool of the NanoScope Software twenty-one values were determined by hand (as shown in figures 6.0.9 and 6.0.10) for the determination of the diameter and the D–periodicity of the fibrils.

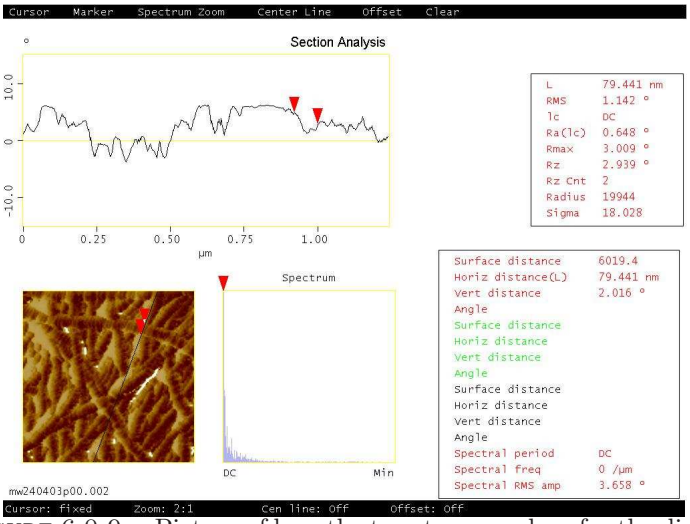

FIGURE 6.0.9. Picture of how the twenty-one values for the diameter measurement were obtained. The limiting arrows were placed manually as good as possible also the line for the cross section was placed in that way that it should be perpendicular to the measured fibril.

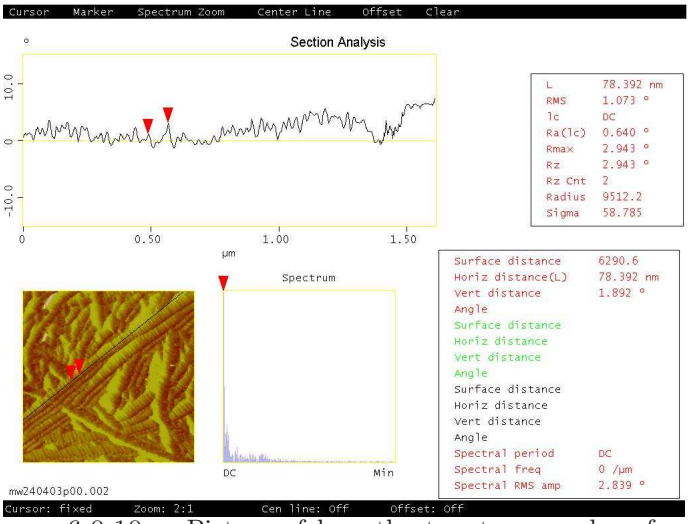

FIGURE 6.0.10. Picture of how the twenty-one values for the D–periodicity measurement were obtained. The limiting arrows were placed manually as good as possible also the line for the cross section was placed in that way that it should be perpendicular to the measured fibril feature.

Figures 6.0.11 and 6.0.12 show the results of these evaluations. It should

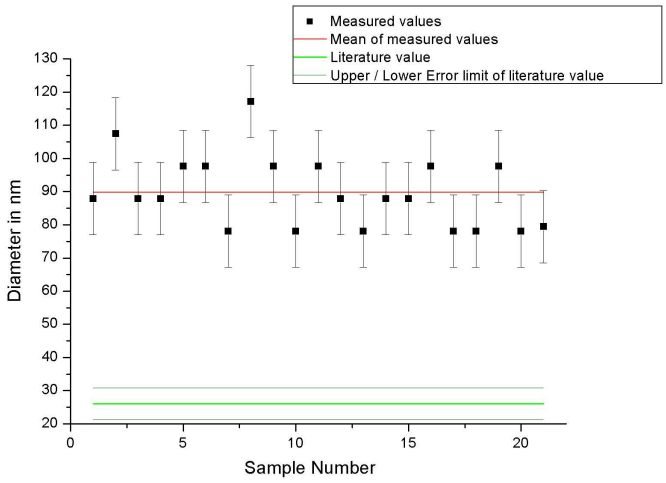

FIGURE 6.0.11. This graph shows the results of the diameter measurement. The literature value was taken from the paper of Atsuko Miyagawa et al. [**44**]. It should be considered that the literature value is for a human cornea and the measured cornea was that of a pig which may explain the differences in the values.

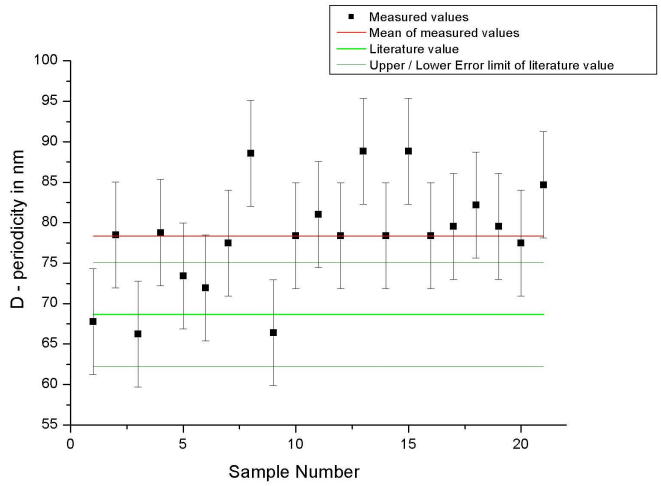

FIGURE 6.0.12. This graph shows the results of the D–periodicity measurement. The literature value was taken from the paper of Atsuko Miyagawa et al. [**44**]. It should be considered that the literature value is for a human cornea and the measured cornea was that of a pig which may explain the differences in the values.

be kept in mind that all our measurements were performed on porcine cornea so literature values which most of the time refer to human corneas are not the right comparison for our results.

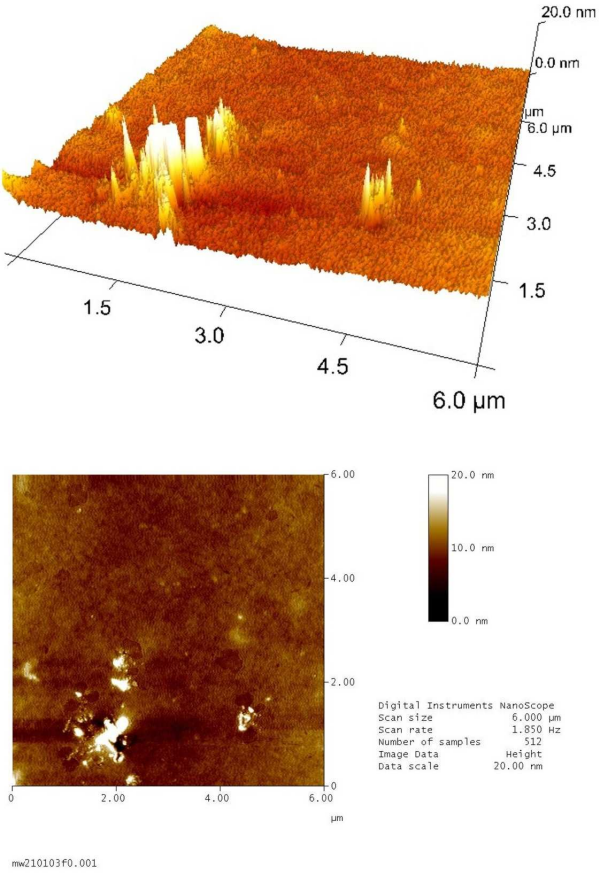

FIGURE 6.0.13. This AFM image shows a picture of a dried gelatin film on a steel puck measured with tapping mode in air. As can be seen the roughness of the surface is very low. The big bumps are due to dust that got stuck during the drying process and could not be removed by using compressed air.

Because we wanted to use gelatin as a glue we produced a gelatin film on a steel puck and measured it with the AFM with tapping mode in air after drying. This was done to assure us that the surface unevenness would not cause problems for the measurement of the cornea slice by changing the topography of the cornea slice to much. As a result the film was very uniform and only adhering dust particles, which were visible with the optical viewing system of the AFM, disturbed the picture. This result means that we have found a possible glue with gelatin which has the feature that its solvent is just water which does not affect the cornea sample.

So everything is now ready for the experiments concerning the change in thickness of the sample and the try to make streaks visible with the AFM. But due to the fact of the time limit for this work these experiments are not included.

CHAPTER 7

Conclusion and Discussion

The human eye is a very complex device and so it is quite delicate. Anything that is done to it has to be well considered. So evaluation of operation methods is the thing to do.

The fs–laser has a great potential to change the surgery methods used until now. The cavitation bubbles that were measured with the SH microscope showed that the fs–laser is a progress compared to the excimer laser and microkeratome. The smoothness of the borders was much better and the effects on the ambient tissue were much smaller. This showed that the fs–laser is a better laser for minimal invasive surgery. So it has to be tested what improvements are achieved with it but also the negative effects that can occur have to be checked. But not only the tools for surgery change also the tools for evaluation of operation methods. Second harmonic imaging is a recently developed microscopy method. It makes microscopy of materials that render second harmonic signals very easy. No staining or other treatment has to be done. So measurements in nearly in vivo conditions are possible. The resolution in all three dimensions is very good because the near–infrared laser beam can penetrate the cornea easily and using a multi-photon process defines the scanning plane to a high degree. By also using stains it is possible to get even more information and use, with this microscope setup, up to three channels simultaneously in one picture (one for the SH signal in transmission direction and two in epifluorescence direction) because SHG occurs in a wide field of wavelengths. This makes SH imaging a great method for evaluation of the fs–laser treatment. The sample preparation methods we used take the easy handling into account and are designed to be equally easy.

But as with all light microscopy methods the resolution is depending on the wavelength of the used illumination light. Even the second harmonic conversion that enhances the resolution because of the fact that the wavelength is changed can not overcome this problem. So for higher resolutions down to nearly molecular scale transmission electron microscopy, scanning electron microscopy or atomic force microscopy has to be used. Only recently, living tissue or cells have been probed successfully with the AFM after the discovery of the tapping mode. The tapping mode minimizes the forces exerted on the sample. The advantages of the AFM compared to the TEM and SEM are clear: The complexity in sample preparation is much smaller for AFM than for TEM / SEM. Because of the possibility to measure in aqueous environments nearly in vivo conditions for measurements are possible as well. The combination of phase image and hight image that can be obtained with the AFM shows a very good resolution of the sample.

Both, the AFM as well as the SH microscope, have their advantages and disadvantages. The table 1 is a short compilation of these positive and negative properties. The field of view was left out as a criteria because it depends on the microscope respective objective used. For the MultiMode AFM the field of view is limited by the scanner that was available to $14\,\mu m$. But most of the time the field of view of the AFM will be much smaller than that of the SH microscope.

	SH microscopy	AFM
advantages:	very easy sample handling	resolution up to atomic scales possible
	possibility to create 3D–images	near in vivo conditions during measurement possible
	near in vivo conditions during measurement possible	independent of the property of the material
	possibility to use stains and SHG simultaneous => more information per image	easy sample handling
	not many variable parameters that determine the quality of the image (it depends mostly on the quality of the hardware components of the microscope)	well defined scale for measurements of fiber thickness for example
disadvantages:	limited resolution due to the use of light waves	only data from surfaces can be obtained => for data of the inside of a 3D–object it has to be sliced
	information depends on the capability of the sample to generate SH => changes may occur that are not visible	"only" height and phase data can be obtains simultaneous
	no predefined scale for measuring fiber thickness for example	many variable parameters determine the image quality (spring constant of the tip, good adjustment of the laser beam path in the scanner head (see figure 3.2.1), control parameters such as integral gain, etc) => to obtain good images a well experienced person is needed

TABLE 1. A short compilation of the advantages and disadvantages of AFM and SH microscopy. The table has not the claim to be complete.

So the usage of either microscope depends on what information has to be gathered. But because of the non–invasive measurement method and the possibility to produce three dimensional images the SH microscopy has a very big advantage.

The problem of the missing scale for the SH microscope can be solved by calculating the point spread function (PSF) for the cornea which will be a next step in the on going experiments. Also a check of correspondence in the SH signals between a human cornea and the measured porcine corneas will be done.

The ongoing experiments (antibody staining and looking at the streaks with the AFM) will be performed in the near future. The problem with the antibodies should be solved soon. The look at the streaks with the AFM may take some more time because of the more difficult slicing process required for this.

There are also some continuative ideas for the evaluation methods of the fs–laser. So it may be worth a try to use fluorescence beads of appropriate diameter to obtain information on the streaks with the SH microscope. If those streaks are really channels of ablated tissue the beads should be able to migrate into them.

Also the wound healing process has to be investigated in a clinical study. This will show how those streaks effect the healing process.

For the fs–laser an optimization of the laser application unit and an investigation in the possible surgical strategies will be future projects. By optimizing the application unit it may be possible to reduce the streaks in length and so minimize the damage to the cornea. Investigating surgical strategies will help to determine the best approach for individual tasks set for the fs–laser.

So the fs–laser is a step in the right direction and the tools for further evaluation are now available.

Bibliography

[1] Grendahl Eye Associates. Anatomy of the eye.

[2] Protein Data Bank. Collagen. http://www.rcsb.org/pdb/molecules/pdb4_1.html.

[3] Protein Data Bank. File 1cag (displayed with raswin). http://www.rcsb.org/pdb/index.html.

[4] P. A. Barnes and K. E. Rieckhoff. Laser induced underwater sparks. *Applied Physical Letters*, 13:282–284, 1968.

[5] G. Bekefi. *Radiation Processes in Plasmas*. New York: John Wiley & Sons, 1966.

[6] C. E. Bell and J. A. Landt. Laser-induced high pressure shock waves in water. *Applied Physical Letters*, 10:46–48, 1967.

[7] R. Bersohn, Zoh-Han Pao, and H.L. Frisch. Double-quantum light scattering by molecules. *Journal of Chemical Physics*, 45(9):3184–3198, 1966.

[8] R. J. Brewer and K. E. Rieckhoff. Stimulated brillouin scattering in liquids. *Physical Review Letters*, 13(334-336), 1964.

[9] E. F. Carome, N. A. Clark, and C. E. Moeller. Generation of acoustic signals in liquids by ruby laser-induced thermal stress transients. *Applied Physical Letters*, 4:95–97, 1964.

[10] St.Luke´s Cataract and Laser Institute. Eye Anatomy. *http://www.stlukeseye.com/Anatomy.html*.

[11] St.Luke´s Cataract and Laser Institute. Eye Anatomy. *http://www.stlukeseye.com/anatomy/TearFilm.asp*.

[12] Ji-Xin Cheng, Y. Kevin Jia, Gengfeng Zheng, and X. Sunney Xie. Laser-scanning coherent anti-stokes raman scattering microscopy and applications to cell biology. *Biophysical Journal*, 83(1):502–509, 2002.

[13] Wai-Fung Cheong, Scott A. Prahl, and Ashley J. Welch. A review of the optical properties of biological tissues. *IEEE Journal of Quantum Electronics*, 26(12):2166–2185, 1990.

[14] S. F. Cleary and P. E. Hamrick. Laser-induced acoustic transients in the mammalian eye. *Journal of the Acoustical Society of America*, 46:1037–1044, 1969.

[15] Guy Cox, Eleanor Kable, Allan Jone, Ian Fraser, Frank Manconi, and Mark D. Gorrell. 3-dimensional imaging of collagen using second harmonic generation. *Journal of Structural Biology (in press)*.

[16] P. A. Felix and A. T. Ellis. Laser-induced liquid breakdown - a step-by-step account. *Applied Physical Letters*, 19:484–486, 1971.

[17] S. Fine and W.P. Hansen. Optical second harmonic generation in biological systems. *Applied Optics*, 10(10):2350–2353, 1971.

[18] Isacc Freund and L. Knopf. Long-range order in nh(4)cl [ammoniumchloride]. *Physical Review Letters*, 24(18):1017–1021, 1970.

[19] E. Fukada. *Advanced Biophysics*, 6:121, 1974.

[20] R. Gauderon, P.B. Lukins, and C.J.R. Sheppard. Optimization of second-harmonic generation microscopy. *Micron*, 32:691–700, 2001.

[21] R. Gauderon and C.J.R. Sheppard. Two-dimensional weak-object transfer functions in the scanning harmonic microscope. *Journal of Modern Optics*, 47:1195–1202, 2000.

[22] M. Goeppert-Mayer. Über Elementarakte mit zwei Quantensprüngen. *Annahlen der Physik (Paris)*, 9:273–294, 1931.

[23] Dr. Meng Han. Microscopic evaluation of fs laser intrastromal surgery. Seminar Talk, Jan 2003.

[24] C.-L. Hu. Spherical model of an acoustic wave generated by rapid laser heating in a liquid. *Journal of the Acoustical Society of America*, 46:728–736, 1969.

[25] C.-L. Hu and F. S. Barnes. The thermal-chemical damage in biological material under laser irradiation. *IEEE Transactions on Biomedical Engineering*, BME-17:220–229, 1970.

[26] TP. Huhges. *Plasmas and Laser Light*. New York: John Wiley & Sons, 1975.

[27] Veeco-Digital Instruments. Crm5.12 rev.b. http://ftp.veeco-europe.de.

[28] Veeco-Digital Instruments. Multimodepolymer. http://www.veeco.com/productImagesBig/MultiModePolymer.jpg.

[29] Veeco-Digital Instruments. Phase imaging - beyond topography. http://www.veeco.com/appnotes/AN1_PhaseImaging.pdf.

[30] Veeco-Digital Instruments. Training notebook v 3. http://ftp.veeco-europe.de.
[31] S.L. Jacques. Simple theory, measurements, and rules of thumb for dosimetry during photodynamic therapy. *Proceedings SPIE*, 1065:100–108, 1989.
[32] Hershall Kaufman. Laser absorption. www.uhmc.sunysb.edu/oralbio/lasers/sld017.htm, 1997.
[33] M. Kempe, U. Stamm, B. Wilhelmi, and W. Rudolph. Spatial and temporal transfromation of femtosecond laser pulses by lenses and lens systems. *Journal of the Optical Society of America Communications*, 9:1158–1165, 1992.
[34] Klaus Kühne. The classical collagens Types i ii and iii. pages 1–42, 1987.
[35] Beop-Min Kim. Novel laser applications in medicine - general physics and clinical applications. physics.hanyang.ac.kr/colloquium/200201/seminar.pdf, 2002.
[36] Dr. Michael W. King. The medical biochemistry page. http://www.indstate.edu/thcme/mwking/extracellularmatrix.html#collagen.
[37] D.A. Kleinman. Second harmonic generation of light. *Physical Review*, 128:1761–1775, 1962.
[38] W. Lauterborn. High-speed photography of laser-induced breakdown in liquids. *Applied Physical Letters*, 21:27–29, 1972.
[39] Chii-Wann Lin. Biophotonics - ch. 4 laser surgery and therapy. http://ibme.mc.ntu.edu.tw/cwlin/courses/handouts/941u0230/Ch4OpticSurgery&Therapy.pdf, 2000.
[40] S. Lydataki, E. Lesniewska, M.K. Tsilimbaris, S. Panagopoulou, C. Le Grimellec, and I.G. Pallikaris. Excimer laser ablated cornea observed by atomic force microscopy. *Single Molecules*, 3(2-3):141–147, 2002.
[41] L. Marti. Tecnologia laser en medicina. *AIDO*, 1997.
[42] Dr. P. McMenamin. Fahers 321 lect 1 the cornea. *http://www.lab.anhb.uwa.edu.au/vsci/cornea.html*.
[43] Leica Microsystems. Basic principle of a confocal microscope. http://www.confocal-microscopy.com/website/sc_llt.nsf.
[44] Atsuko Miyagawa, Miya Kobayashi, Yoshikazu Fujita, Ossama Hamdy, Koji Hirano, Makoto Nakamura, and Yozo Miyake. Surface ultrastructure of collagen fibrils and their association with proteoglycans in human cornea and sclera by atomic force microscopy and energy-filtering transmission electron microscopy. *Cornea*, 20(6):651–656, 2001.
[45] Mark H. Niemz, Edward G. Klancnik, and Josef F. Bille. Plasma-mediated ablation of corneal tissue at 1053 nm using a nd:ylf oscillator/regenerative amplifier laser. *Lasers in Surgery and Medicine*, 11:426–431, 1991.
[46] Center of Ultrafast Optical Science. Femtosecond lamellar keratoplasty (flk). http://www.eecs.umich.edu/CUOS/Medical/CornealRefractive.html.
[47] Center of Ultrafast Optical Science. Lasik with the fs laser to produce the flap. http://www.eecs.umich.edu/CUOS/Medical/CornealRefractive.html.
[48] B. F. Ponomarenko, V. I. Samoilov, and P. I. Ulyakov. Polarization-optical investigation of the failure of transparent dielectrics laser radiation. *Soviet Physics Journal of experimental and theoretical physics*, 27:415–419, 1968.
[49] Carmen A. Puliafito and Roger F. Steinert. Short-pulsed nd:yag laser microsurgery of the eye: Biophysical considerations. *IEEE Journal of Quantum Electronics*, QE-20(12):1442–1448, 1984.
[50] J. F. Ready. Effects of high-power laser radiation. *New York: Academic*, page 301, 1971.
[51] J. F. Ready. Effects of high-power laser radiation. *New York: Academic*, pages 279–283, 1971.
[52] J. F. Ready. Effects of high-power laser radiation. *New York: Academic*, page 261 and 262, 1971.
[53] Samuel Roth and Isaac Freund. Second harmonic generation in collagen. *Journal of Chemical Physics*, 70((04)):1637–1643, 1979.
[54] Carl Zeiss Life Science and Health Care. Laser scanning mikroskope. http://www.zeiss.de/C12567BE00459794/allBySubject/2BD456F1B35DF1C2C1256AE3003656BB.
[55] Carl Zeiss Life Science and Health Care. Laser scanning mikroskope. http://www.zeiss.de/C12567BE00459794/allBySubject/8CB38E3166E0FA7CC1256AED00273172.
[56] D. Stern, CA. Puliafito, ET. Dobi, and WT. Reidy. Corneal ablation by nanosecond, picosecond and femtosecond lasers at 532 nm and 625 nm. *Archives of Ophthalmology*, 107:587–592, 1989.
[57] Brian C. Wilson and Steven L. Jacques. Optical reflectance and transmittance of tissues: Principles and applications. *IEEE Journal of Quantum Electronics*, 26(12):2186–2199, 1990.
[58] Aikaterini Zuomi, Alvin Yeh, and Bruce J. Tromberg. Imaging cells and extracellular matrix *in vivo by using second-harmonic generation and two-photon excited fluorescence.* Proceedings of the National Academy of Sciences of the United States of America*, 99(17):11014–11019, 2002.*

APPENDIX A

Multiphoton Absorption and Emission

(according to a paper from Goeppert Mayer [**22**])

We will look at the interaction of an atom in a radiation field. The radiation should be thought of being trapped in a cubic box with the volume V, so the number of degrees of freedom is countable. This box should also cause the light waves to reiterate them self periodically outside of it. Later this box will be thought of being endless. Such a radiation field is equivalent to a system of uncoupled harmonic oscillators. So the radiation can be dissected into planar, linear polarized waves. Let $\vec{A}$ be the vectorpotential which is given by

$$\vec{A} = \sum_k q^k A^k = \sum_k q^k \mathfrak{e}^k e^{2\pi i \nu_k \left(s_x^k x + s_y^k y + s_z^k z\right)} \tag{A.0.1}$$

The components of the vector $\nu_k s^k$ in equation A.0.1 are given by the whole-numbered relations to the extension of the box. Also every vector $\nu_k s^k$ in equation A.0.1 has two unit vectors $\mathfrak{e}^k$ that are orthogonal to them self and also orthogonal to s^k. In a big cavity the asymptotic number of eigen oscillations between the frequencies ν and $\nu + \Delta\nu$ is given by

$$Z(\nu)\,\Delta\nu = \frac{8\pi\nu^2}{c^3} V \Delta\nu \tag{A.0.2}$$

The Maxwell equations provide for q^k the differential equation of the harmonic oscillator. With the quantization results the Hamiltonian of the radiation with

$$\sum_k H^k = \sum_k h\nu_k \left(n_k + \frac{1}{2}\right) \tag{A.0.3}$$

A state s of the radiation field is described by indicating the states of all oscillators $s = (n_1 \ldots n_k \ldots)$. The energy difference between two states of the cavity is

$$h\nu_{ss'} = \sum_k h\nu_k \left(n_k - n_k^{'}\right) \tag{A.0.4}$$

With this the matrix elements of q^k are given by

$$\begin{aligned} q^k_{ss'} &= \sqrt{\frac{hc^2}{2\pi\nu_k V}\,(n_k+1)} && \text{for } n_k^{'} = n_k + 1,\ n_l^{'} = n_l \\ &= \sqrt{\frac{hc^2}{2\pi\nu_k V}\,(n_k)} && \text{for } n_k^{'} = n_k + 1,\ n_l^{'} = n_l \\ &= 0 && \text{sonst.} \end{aligned} \tag{A.0.5}$$

An atom with a localized nucleus, the Hamiltonian H_{Atom}, the stationary states n and the eigen frequencies $\nu_{nn'}$ should be interacting with the radiation field. The Hamiltonian of the whole system is then given by

$$H = \sum_k H^k + H_{Atom} + H^{'} \tag{A.0.6}$$

$H^{'}$ is the interaction energy which is resulting from the Hamiltonian function of the electron:

$$H_{el} = \frac{\vec{p}^{\,2}}{2m} + V(\vec{q}) + \frac{e}{mc}\left(\vec{p}\vec{A}\right) + \frac{e^2}{2mc^2}\vec{A}^{\,2} \tag{A.0.7}$$

In equation A.0.7 is $\vec{p}$ the momentum vector and $\vec{q}$ the vector of the coordinates of an electron in the atom. V is the potential energy of the electron and $\vec{A}$ is the vector potential of the radiation field at the location of the electron. The twofold interaction energy

$$H^{'} = \frac{e}{mc}\left(\vec{p}\vec{A}\right) + \frac{e^2}{2mc^2}\vec{A}^{\,2} \tag{A.0.8}$$

is easily transformed in a simpler Form. If we form the property function of H_{el} which is the following

$$L = \dot{\vec{q}}\vec{p} - H_{el} \tag{A.0.9}$$

and then express it with $\dot{\vec{q}} = \frac{\partial H_{el}}{\partial \vec{p}}$ as a function of $\vec{q}$ and $\dot{\vec{q}}$ we get:

$$L\left(\dot{\vec{q}}, \vec{q}\right) = \frac{m}{2}\dot{\vec{q}}^{\,3} - V(\vec{q}) - \frac{e}{c}\left(\dot{\vec{q}}\vec{A}\right) \tag{A.0.10}$$

The equation A.0.10 is equivalent to another property function which results through the addition of the total temporal differential $\frac{d}{dt}\left(\vec{q}\vec{A}\right)$ to the equation A.0.9:

$$\bar{L}\left(\dot{\vec{q}}, \vec{q}\right) = \frac{m}{2}\dot{\vec{q}}^{\,2} - V(\vec{q}) + \frac{e}{c}\left(\vec{q}\frac{d\vec{A}}{dt}\right) \tag{A.0.11}$$

If we form the Hamiltonian function $\bar{H}_{el}$ that is related with the property function A.0.11 we get:

$$\bar{H}_{el} = \frac{\bar{\vec{p}}^{\,2}}{2m} + V(\vec{q}) - \frac{e}{c}\left(\vec{q}\frac{d\vec{A}}{dt}\right) \tag{A.0.12}$$

If the wave length of the light is large compared with the dimension of the atom the spatial fluctuation of the vector potential $\vec{A}$ in the atom can be neglected which means $\frac{d\vec{A}}{dt} = \frac{\partial \vec{A}}{\partial t} = \dot{\vec{A}}$.
The result for the interaction energy after the introduction of the electrical moment $\vec{P} = \sum_r e\vec{q}_r$ (all electrons of the atom have to be summed up) is

$$H^{'} = -\frac{1}{c}\left(\vec{P}\dot{\vec{A}}\right) \tag{A.0.13}$$

In equation A.0.13 the value for $\dot{\vec{A}}$ can be set to be the same as at the location x_0, y_0, z_0 in the center of the atom. Because $\frac{1}{c}\dot{\vec{A}}$ is the same as the electrical field strength $\vec{E}$ of the radiation the interaction energy is under these circumstances reduced to the potential energy of the electrical moment $\vec{P}$ against the light field. $H^{'}$ is considered as a perturbation and the eigen function of the whole system will be developed from the eigen functions of the undisturbed system

$$\Psi = \sum a_{ns}\psi_{ns} \tag{A.0.14}$$

Under the assumption that the system at the time $t = 0$ is in the state n^0, s^0 the perturbation theory provides for amounts of time that are small against the mean residence time the probability amplitudes a_{ns} to be as a first approximation

$$a_{ns}^{(1)} = H^{'}_{ns,n^0s^0}\frac{1 - e^{2\pi i\left(\nu_{nn^0} + \nu_{ss^0}\right)t}}{h\left(\nu_{nn^0} + \nu_{ss^0}\right)} \tag{A.0.15}$$

and as a second approximation

(A.0.16)
$$a_{ns}^{(2)} = \sum_{n's'} \frac{H'_{nn',ss'} H'_{n'n^0,s's^0}}{h\left(\nu_{n'n^0} + \nu_{s's^0}\right)} \cdot \left[\frac{1 - e^{2\pi i\left(\nu_{nn'} + \nu_{ss'}\right)t}}{h\left(\nu_{nn'} + \nu_{ss'}\right)} - \frac{1 - e^{2\pi i\left(\nu_{nn^0} + \nu_{ss^0}\right)t}}{h\left(\nu_{nn^0} + \nu_{ss^0}\right)} \right]$$

Equation A.0.15 shows the absorption and emission. Equation A.0.16 shows not only the Raman effect and dispersion but also the effects of the simultaneous emission and absorption of two light quanta which are of interest in this work.

Let us look first at the double emission. The atom shall be in the excited state n^0 at the time $t = 0$ and in the box there shall be only one eigen oscillation

(A.0.17)
$$A^k = \mathfrak{e}^k e^{2\pi i \nu_k \left(s_x^k x + s_y^k y + s_z^k z\right)}$$

with the frequency ν_k which is not identical with any eigen frequency of the atom. This eigen oscillation (s. equation A.0.17) shall be intensely excited what means

(A.0.18)
$$n_k^0 \gg 1 \; ; \; n_l^0 = 0 \text{ for } l \neq k \; ; \; \nu_k \neq \nu_{nn'}$$

Because of the properties of the oscillator matrices q^k (s. equation A.0.5) in

(A.0.19)
$$H'_{nn'ss'} = \sum_k \dot{q}_{ss'}^k \left(\vec{P}_{nn'} A^k \right)$$

$H'_{nn'ss'} H'_{n'n^0s's^0}$ is only then not identical with zero if s emanates from s^0 either by absorption of one light quantum ν_k of the send in frequency and emission of one arbitrary other light quantum ν_l - this is the Raman effect and the dispersion - or by emission of two light quanta. We will see in the future that if ν_k is fixed the conservation of the total energy is only possible with emission of a certain frequency. To include both these cases in the following computations we will use the following convention: double signs in the equations are that way that the upper one is for the Raman effect and the dispersion and the lower one is for double emission. This means the following:

(A.0.20)
$$\begin{aligned} a_{ns}^{(2)} \quad = \quad & \frac{\dot{q}_{n_k^0 \pm 1, n_k^0}^k \dot{q}_{1,0}^l}{c^2} - \sum_{n'} \left[\frac{\left(\vec{P}_{nn'} A^k \right) \left(\vec{P}_{n'n^0} A^l \right)}{h\left(\nu_{n'n^0} + \nu_l\right)} \right. \\ & \cdot \left\{ \frac{1 - e^{2\pi i\left(\nu_{nn'} \mp \nu_k\right)t}}{h\left(\nu_{nn'} \mp \nu_k\right)} - \frac{1 - e^{2\pi i\left(\nu_{nn^0} + \nu_l \mp \nu_k\right)t}}{h\left(\nu_{nn^0} + \nu_l \mp \nu_k\right)} \right\} \\ & + \frac{\left(\vec{P}_{nn'} A^l \right) \left(\vec{P}_{n'n^0} A^k \right)}{h\left(\nu_{n'n^0} \mp \nu_k\right)} \\ & \left. \cdot \left\{ \frac{1 - e^{2\pi i\left(\nu_{nn'} + \nu_l\right)t}}{h\left(\nu_{nn'} + \nu_l\right)} - \frac{1 - e^{2\pi i\left(\nu_{nn^0} + \nu_l \mp \nu_k\right)t}}{h\left(\nu_{nn^0} + \nu_l \mp \nu_k\right)} \right\} \right] \end{aligned}$$

$a_{ns}^{(2)}$ is only then considerably different from zero if ν_l is in the neighborhood of or zero for one of the three denominators from equation A.0.20

(A.0.21)
$$\nu_{n'n^0} + \nu_l \quad , \quad \nu_{nn'} + \nu_l \quad , \quad \nu_{nn^0} + \nu_l \mp \nu_k$$

The neighborhood of zero of the first two denominators provides the probability for processes in which the the energy theorem is not retained. Those processes are transitions of the atom from n^0 to n by absorption respectively emission of a quantum of the send in frequency ν_k and emission of an eigen frequency of the atom. Those transitions don't occur in reality. They are a peculiarity of the here used method of varying the constants. By doing this we assume that the perturbation

energy $H^{'}$ starts to act at a time t=0. In reality the effect is continuous. This "switching on" is the cause for the abnormal transitions.

The neighborhood of zero of the third denominator which describes the change of the total energy in this process is the essential one. For frequencies ν_l in the neighborhood of $\nu^{'} = \nu_{n^0 n} \pm \nu_k$ the following parts of equation A.0.20 can be neglected :

$$\frac{1-e^{2\pi i\left(\nu_{nn'}\mp\nu_k\right)t}}{h\left(\nu_{nn'}\mp\nu_k\right)} \quad , \quad \frac{1-e^{2\pi i\left(\nu_{nn'}+\nu_l\right)t}}{h\left(\nu_{nn'}+\nu_l\right)} \tag{A.0.22}$$

By doing this we get the following equation if we use the values of the matrix elements q from A.0.5

The sign $\begin{pmatrix} 0 \\ 1 \end{pmatrix}$ means that for dispersion and Raman effect 0 and for double emission 1 has to be used.

$$\begin{aligned} \left|a_{ns}^{(2)}\right|^2 &= \frac{4\pi^2 h^2}{V^2}\left(n_k^0 + \begin{pmatrix} 0 \\ 1 \end{pmatrix}\right) \\ &\cdot\left|\sum_{n'}\left(\frac{\left(\vec{P}_{nn'}\mathfrak{e}^k\right)\left(\vec{P}_{n'n^0}\mathfrak{e}^l\right)}{h\left(\nu_{n'n^0}+\nu_l\right)} + \frac{\left(\vec{P}_{nn'}\mathfrak{e}^l\right)\left(\vec{P}_{n'n^0}\mathfrak{e}^k\right)}{h\left(\nu_{n'n^0}\mp\nu_k\right)}\right)\right|^2 \\ &\cdot\frac{4\sin^2\pi\left(\nu_{nn^0}+\nu_l\mp\nu_k\right)t}{h^2\left(\nu_{nn^0}+\nu_l\mp\nu_k\right)^2} \end{aligned} \tag{A.0.23}$$

The probability of this process is given by summation of $\left|a_{ns}^{(2)}\right|^2$ for all l for which ν_l is in the neighborhood of $\nu^{'}$. For a big cavity the sum $\sum_l$ is changed into an integral $\int Z\left(\nu_l\right)d\nu_l$ (s. equation A.0.2) for the number of all eigen oscillations A^l. Because of the sharp maximum of the integrand at the location of the resonance we get then

$$\begin{aligned} \sum_l\left|a_{ns}^{(2)}\right|^2 &= \frac{8\pi^2 h^2}{V^2}\cdot\frac{1}{3}\left(n_k^0 + \begin{pmatrix} 0 \\ 1 \end{pmatrix}\right) \\ &\cdot\left|\sum_{n'}\left(\frac{\left(\vec{P}_{nn'}\mathfrak{e}^k\right)\cdot\vec{P}_{n'n^0}}{h\left(\nu_{n'n^0}+\nu_l\right)} + \frac{\vec{P}_{nn'}\cdot\left(\vec{P}_{n'n^0}\mathfrak{e}^k\right)}{h\left(\nu_{n'n^0}\mp\nu_k\right)}\right)\right|^2 \\ &\cdot\int Z\left(\nu_l\right)\frac{2\sin^2\pi\left(\nu_{nn^0}+\nu_l\mp\nu_k\right)t}{h^2\left(\nu_{nn^0}+\nu_l\mp\nu_k\right)^2}d\nu_l \\ \Rightarrow\sum_l\left|a_{ns}^{(2)}\right|^2 &= \frac{64\pi^4\nu^{'3}}{3hc^3}\cdot\frac{2\pi h\nu_k\left(n_k^0 + \begin{pmatrix} 0 \\ 1 \end{pmatrix}\right)}{V} \\ &\cdot\left|\sum_{n'}\left(\frac{\left(\vec{P}_{nn'}\mathfrak{e}^k\right)\cdot\vec{P}_{n'n^0}}{h\left(\nu_{n'n}\pm\nu_k\right)} + \frac{\vec{P}_{nn'}\cdot\left(\vec{P}_{n'n^0}\mathfrak{e}^k\right)}{h\left(\nu_{n'n^0}\mp\nu_k\right)}\right)\right|^2\cdot t \end{aligned} \tag{A.0.24}$$

Equation A.0.24 has only then any meaning if $\nu^{'} > 0$. So double emission is only possible if $\nu_{n^0 n} > 0$ and the sent in frequency is $\nu_k < \nu_{n^0 n}$.

Until now we only used one eigen function of the cavity. Now let us assume that more than one eigen function is intensely excited at the beginning and that a spectral line of finite broadness is sent in. Under these circumstances looking at the case of double emission the probability of emission of ν_k not exactly in the one eigen function A^k but in a narrow frequency range $\triangle\nu$ shows that equation A.0.24 has to be summed up for all eigen oscillations A^k with the frequency between ν and $\nu+\triangle\nu$. Using the function $\rho\left(\nu\right)$ of the mean monochromatic emittance which

is defined by

$$V\rho(\nu)\triangle\nu = \sum_{\nu<\nu_k<\nu+\triangle\nu} h\nu_k n_k^0 \tag{A.0.25}$$

we derive the probability of the double emission per time

(A.0.26)

$$w_{nn^0}^{d_e} = \frac{64\pi^4\nu'^3}{3hc^3}\cdot 2\pi\left(\rho(\nu)+\frac{8\pi\nu^3 h}{c^3}\right)\triangle\nu\cdot\frac{1}{3}\left|\sum_{n'}\left(\frac{\vec{P}_{nn'}\cdot\vec{P}_{n'n^0}}{h(\nu_{n'n}-\nu)}+\frac{\vec{P}_{nn'}\cdot\vec{P}_{n'n^0}}{h(\nu_{n'n^0}+\nu)}\right)\right|^2$$

This shows that for an unoccupied cavity there is a probability for the spontaneous simultaneous emission of two light quanta and that every frequency partition is possible. If light of the frequency ν is sent in the part of the forced emission of the frequency ν' behaves in its intensity like a virtual oscillator with the momentum

$$\vec{P}_{nn^0}^k = \sqrt{2\pi\rho(\nu)}p_{nn^0}^k \text{ with} \tag{A.0.27}$$

$$p_{nn^0}^k = \sum_{n'}\left(\frac{\left(\vec{P}_{nn'}\vec{\mathfrak{e}}\right)\cdot\vec{P}_{n'n^0}}{h(\nu_{n'n}-\nu)}+\frac{\vec{P}_{nn'}\cdot\left(\vec{P}_{n'n^0}\vec{\mathfrak{e}}\right)}{h(\nu_{n'n^0}+\nu)}\right) \tag{A.0.28}$$

which emits the frequency ν' spontaneous. The strength of the forced double emission is for normal emittance much smaller than for the analogous spontaneous double emission.[1] The equation A.0.28 is analogous to the equation for the Raman effect in which the leading momentum is

$$p_{nn^0}^r = \sum_{n'}\left(\frac{\left(\vec{P}_{nn'}\vec{\mathfrak{e}}\right)\cdot\vec{P}_{n'n^0}}{h(\nu_{n'n}+\nu)}+\frac{\vec{P}_{nn'}\cdot\left(\vec{P}_{n'n^0}\vec{\mathfrak{e}}\right)}{h(\nu_{n'n^0}-\nu)}\right) \tag{A.0.29}$$

The observed intensity is depending on the number of atoms in the initial state which is in this case an excited state. So the occurrence of double emission is nearly unobservable because of the strength of the spontaneous normal emission. Only if there are meta stable states which have a low probability for spontaneous emission$\left(\left|\vec{P}_{nn^0}\right|^2 \text{ has a small value}\right)$ is there a chance to observe double emission.

The inverse process, the double absorption, is depending on the number of atoms in the ground state. The equations for this are almost analogous to the ones we have calculated before. Only the initial state n^0 of the atom is the ground state this time and before the perturbation there is only light of two small spectral ranges with the mean frequency ν respectively ν' in the box. The mean frequency sum of these spectral ranges is equivalent to an eigen frequency of the atom $\nu+\nu' = \nu_{nn^0}$. The eigen functions of each spectral range shall have the same direction of propagation s respectively s' and the same polarization $\vec{\mathfrak{e}}$ respectively $\vec{\mathfrak{e}}'$.

With the same considerations as before the probability amplitude a_{ns}^2 (s. equation A.0.16) of the transition from n^0 to n is only then considerably different from zero if the state s emanates from the state s' in the box by absorption of a light quant ν_k from the spectral range ν and a light quant ν_l from the spectral range ν'.

[1] It is the same ratio as between forced normal emission and spontaneous normal emission.

By neglecting analogous terms as in equation A.0.23 for such transitions we get:

$$\begin{aligned} a_{ns}^{(2)} &= \frac{1}{c^2}\dot{q}^k_{n^0_k-1,n^0_k}\dot{q}^l_{n^0_l-1,n^0_l} \\ &\quad \cdot\sum_{n'}\left[\frac{\left(\vec{P}_{nn'}\mathfrak{e}^l\right)\left(\vec{P}_{n'n^0}\mathfrak{e}^k\right)}{h\left(\nu_{n'n^0}-\nu_k\right)}+\frac{\left(\vec{P}_{nn'}\mathfrak{e}^k\right)\left(\vec{P}_{n'n^0}\mathfrak{e}^l\right)}{h\left(\nu_{n'n^0}-\nu_l\right)}\right] \\ &\quad \cdot\frac{1-e^{2\pi i\left(\nu_{nn^0}-\nu_k-\nu_l\right)t}}{h\left(\nu_{nn^0}-\nu_k-\nu_l\right)} \\ &= \frac{2\pi h}{V}\sqrt{n^0_k\nu_k n^0_l\nu_l} \\ &\quad \cdot\sum_{n'}\left[\frac{\left(\vec{P}_{nn'}\vec{\mathfrak{e}}'\right)\left(\vec{P}_{n'n^0}\vec{\mathfrak{e}}\right)}{h\left(\nu_{n'n^0}-\nu_k\right)}+\frac{\left(\vec{P}_{nn'}\vec{\mathfrak{e}}\right)\left(\vec{P}_{n'n^0}\vec{\mathfrak{e}}'\right)}{h\left(\nu_{n'n^0}-\nu_l\right)}\right] \\ &\quad \cdot\frac{1-e^{2\pi i\left(\nu_{nn^0}-\nu_k-\nu_l\right)t}}{h\left(\nu_{nn^0}-\nu_k-\nu_l\right)} \end{aligned} \tag{A.0.30}$$

The probability of this process can be gained by summation of $\left|a_{ns}^{(2)}\right|^2$ for s. This means that for a big box we have to integrate over ν_k and ν_l. By using the in equation A.0.25 defined function $\rho(\nu)$for the monochromatic emittance per volume we get because of the sharp resonance at $\nu_k+\nu_l=\nu_{nn^0}$:

$$\begin{aligned} \sum\left|a_{ns}^{(2)}\right|^2 &= 4\pi^2\cdot\left|\sum_{n'}\left[\frac{\left(\vec{P}_{nn'}\vec{\mathfrak{e}}'\right)\left(\vec{P}_{n'n^0}\vec{\mathfrak{e}}\right)}{h\left(\nu_{n'n^0}-\nu\right)}+\frac{\left(\vec{P}_{nn'}\vec{\mathfrak{e}}\right)\left(\vec{P}_{n'n^0}\vec{\mathfrak{e}}'\right)}{h\left(\nu_{n'n^0}-\nu'\right)}\right]\right|^2 \\ &\quad \cdot\int\rho\left(\nu_k\right)\rho\left(\nu_l\right)\frac{4\sin^2\pi\left(\nu_{nn^0}-\nu_k-\nu_l\right)t}{h^2\left(\nu_{nn^0}-\nu_k-\nu_l\right)^2}d\nu_k d\nu_l \end{aligned} \tag{A.0.31}$$

$$w_{nn^0}^{d_a}=\frac{16\pi^4}{h^2}\int\rho\left(\nu_{nn^0}-\nu\right)\rho\left(\nu\right)d\nu\left|p^k_{nn^0}\vec{\mathfrak{e}}'\right|^2 \tag{A.0.32}$$

$p^k_{nn^0}$ in equation A.0.32 means the same vector that is defined in equation A.0.28. It has to be integrated over the broadness of the sent in spectral line. As you can see the probability of simultaneous absorption is smaller than that of simultaneous emission at normal light densities. The ratio of double absorption to double emission is the same as in normal emission and absorption. This means that the processes of double emission respectively double absorption will not disturb the radiation balance of the system.

The number of double absorptions is increased by the fact that it is proportional to the number of atoms in the ground state. On the other hand there is the quadratical dependence on the light density (s. equation A.0.31) which is the cause why the effect is observable only with high light intensities.

The following graphics (figure A.0.1) shows the efficiency of the two photon fluorescence excitation.

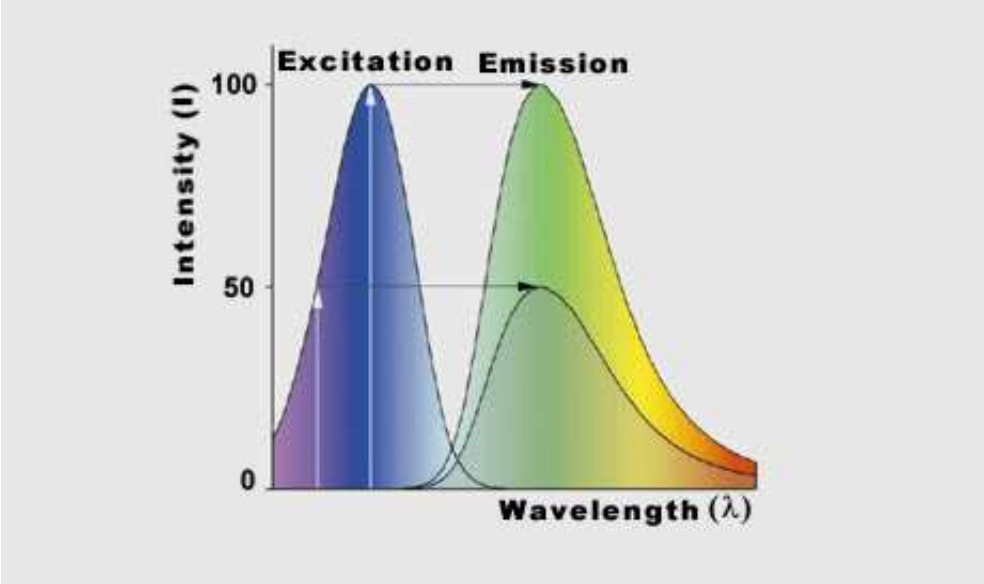

FIGURE A.0.1. Excitation efficiency of two photon fluorescence[**55**]

APPENDIX B

Second Harmonics Generation in a Crystal

Second harmonic generation was first observed in crystals which were piezoelectric [**37**]. This implies that the primary nonlinear effect is a polarization of second order in the electric field

$$\vec{P} = d \cdot \vec{E}\vec{E} \tag{B.0.33}$$

where $\vec{E}\vec{E}$ represents the 6 components $E_i E_j$ of the electric field, $\vec{P}$ is the dielectric polarization and d is a tensor which we shall call the *third - order polarization tensor*. It follows that the selection rules imposed by crystal symmetry on d are the same as for the piezoelectric tensor. d will be also a function of the frequency.

It was recognized that a "coherence volume" exists for second harmonics generation within which the second harmonic wave can remain in phase with the polarization producing it. Nonlinear interaction can mix two light beams. If the beams are plane waves with wave vectors $\vec{K_1}$ and $\vec{K_2}$ the polarization at the sum frequency has the wave vector $\vec{K} = \vec{K_1} + \vec{K_2}$. The case that $\vec{K_1} = \vec{K_2}$ and therefore $\vec{K} = 2\vec{K_1}$ or $\vec{K} = 2\vec{K_2}$ is also possible. In any case $\vec{K}$ can be written as

$$\vec{K} = \left(\frac{\omega}{c}\right) n^{'} \vec{s}_k \tag{B.0.34}$$

where ω is either the sum or the second harmonic frequency, $\vec{s}_k$ is a unit vector in the direction of $\vec{K}$ and $n^{'}$ is an effective refractive index. In general $n^{'}$ will not equal the refractive index n for a wave freely propagating in the medium in the direction $\vec{s}_k$ with the frequency ω. The effect of normal dispersion is to make $n^{'}$ less than n. In the case of mixing the wave vectors $\vec{K_1}$ and $\vec{K_2}$at a non vanishing angle $n^{'}$is further reduced. The coherence volume may be defined as the cross - sectional area of the beam multiplied by a coherence length

$$l_{coh} = \lambda \left[\left(\frac{n^{'}}{n}\right) - 1\right]^{-1} \tag{B.0.35}$$

where $\lambda = \left(\frac{2\pi c}{\omega n}\right)$ is the wave length in the medium of the second harmonic wave. To obtain a formal solution to the problem of the radiation produced by a plane polarization wave

$$\vec{P}\left(\vec{r}, t\right) = \vec{P} e^{i\left(\vec{K}\cdot\vec{r} - \omega t\right)} \tag{B.0.36}$$

the wave vector $\vec{K}$ may be written in terms of $n^{'}$ and $\vec{s}_k$ as in equation B.0.34 and ω is twice the angular frequency of the fundamental wave or the sum of frequencies of two mixed waves. The direction and magnitude of $\vec{P}$ are determined by the tensor d and the electric fields of the fundamental or mixed waves. Given $\vec{P}$ and $\vec{K}$ we must determine the second harmonic electric field from the inhomogeneous vector equation

$$\nabla \times \nabla \times \vec{E} - \left(\frac{\omega^2}{c^2}\right) \varepsilon \cdot \vec{E} = \left(\frac{4\pi\omega^2}{c^2}\right) \vec{P} \cdot e^{i\vec{K}\cdot\vec{r}} \tag{B.0.37}$$

By assuming that the permeability is the same as in free space, the magnetic field can be neglected. A solution for the equation of the form

$$\vec{E}\left(\vec{r}\right) = \vec{E}^{'} \cdot e^{i\frac{\omega}{c}n^{'}\vec{s}_k\cdot\vec{r}} \tag{B.0.38}$$

has to be sought which can be obtained by substituting equation B.0.38 into equation B.0.37 which gives:

$$\alpha_k \cdot \vec{E}^{'} = 4\pi\vec{P} \tag{B.0.39}$$

where α_k is the dyadic

$$\alpha_k = n^{'2}\left(I - \vec{s}_k\vec{s}_k\right) - \varepsilon \tag{B.0.40}$$

If $n^{'} \neq n_k$, as is the general case, the inverse dyadic α_k^{-1} exits and the solution of equation B.0.39 is

$$\vec{E}^{'} = \alpha_k^{-1} \cdot 4\pi\vec{P} \tag{B.0.41}$$

The wave B.0.38 with $\vec{E}^{'}$ given by equation B.0.41 is a particular solution of the inhomogeneous wave equation B.0.37. The inverse α_k^{-1} may be constructed as follows: Define the eigenvalues $\lambda_k^{(j)}$ and eigenvectors $\vec{U}_k^{(j)}$ of α_k

$$\alpha_k \cdot \vec{U}_k^{(j)} = \lambda_k^{(j)} \cdot \vec{U}_k^{(j)} \quad (j = 1, 2, 3) \tag{B.0.42}$$

Since α_k is real and symmetric, the $\vec{U}_k^{(j)}$ are mutually orthogonal and may be normalized to unit length. If none of the $\lambda_k^{(j)}$ vanishes, the inverse is then

$$\alpha_k^{-1} = \sum_j \frac{1}{\lambda_k^{(j)}} \vec{U}_k^{(j)} \vec{U}_k^{(j)} \tag{B.0.43}$$

In the matching case $n^{'} = n_k$ $\lambda_k^{(1)} = 0$. From equation B.0.43 we see that there is no problem if $\vec{P}\vec{U}_k^{(1)} = 0$ otherwise if $\vec{P}\vec{U}_k^{(1)} \neq 0$ there is no wave in the form of a plane wave of constant amplitude. Therefore, we seek a solution in the form of a linearly growing wave. Let the field in the matching case be written

$$\vec{E}_M\left(\vec{r}\right) = \vec{E}_1\left(\vec{N}\cdot\vec{r}\right)e^{i\left(\frac{\omega}{c}\right)n_M\vec{s}_M\cdot\vec{r}} + \vec{E}_{2,3}e^{i\left(\frac{\omega}{c}\right)n_M\vec{s}_M\cdot\vec{r}} \tag{B.0.44}$$

where

$$\begin{aligned} \vec{E}_1 &= E_1\vec{U}_M^{(1)} \\ \vec{E}_{2,3} &= E_2\vec{U}_M^{(2)} + E_3\vec{U}_M^{(3)} \end{aligned} \tag{B.0.45}$$

The subscript k has been replaced by M to indicate the matching case, and n_M is the refractive index for $\vec{s}_M = \vec{s}_k$ in equation B.0.44. $\vec{N}$ is an arbitrary unit vector indicating the direction in which $\vec{E}_M\left(\vec{r}\right)$ grows. We will see later that $\vec{N}$ is the normal to the surface of the medium. Substituting equation B.0.44 in equation B.0.37 gives

(B.0.46)

$$i\left(\frac{\omega}{c}\right)n_M\left[\vec{s}_M\times\left(\vec{N}\times\vec{E}_1\right) + \vec{N}\times\left(\vec{s}_M\times\vec{E}_1\right)\right] + \left(\frac{\omega^2}{c^2}\right)\alpha_M\cdot\vec{E}_{2,3} = \left(\frac{4\pi\omega^2}{c^2}\right)\vec{P}$$

The solution of equation B.0.46 is readily found to be

$$\begin{aligned} E_1 &= -2\pi i \left(\frac{\omega}{c}\right) n_M^{-1} \times \\ &\left[\left(\vec{N}\cdot\vec{U}_M^{(1)}\right)\left(\vec{s}_M\cdot\vec{U}_M^{(1)}\right) - \vec{N}\cdot\vec{s}_M\right]^{-1} \vec{P}\cdot\vec{U}_M^{(1)} \end{aligned} \tag{B.0.47}$$

$$\begin{aligned} E_2 &= -\left(\frac{4\pi}{\lambda_M^{(2)}}\right)\vec{P}\cdot\vec{U}_M^{(2)} - i\left(\frac{\omega}{c}\right) n_M \cdot \\ &\left[\left(\vec{N}\cdot\vec{U}_M^{(2)}\right)\left(\vec{s}_M\cdot\vec{U}_M^{(1)}\right) + \left(\vec{N}\cdot\vec{U}_M^{(1)}\right)\left(\vec{s}_M\cdot\vec{U}_M^{(2)}\right)\right]\cdot \\ &\left(\frac{1}{\lambda_M^{(2)}}\right) E_1 \end{aligned} \tag{B.0.48}$$

$$\begin{aligned} E_3 &= -\left(\frac{4\pi}{\lambda_M^{(3)}}\right)\vec{P}\cdot\vec{U}_M^{(3)} - i\left(\frac{\omega}{c}\right) n_M \cdot \\ &\left[\left(\vec{N}\cdot\vec{U}_M^{(3)}\right)\left(\vec{s}_M\cdot\vec{U}_M^{(1)}\right) + \left(\vec{N}\cdot\vec{U}_M^{(1)}\right)\left(\vec{s}_M\cdot\vec{U}_M^{(3)}\right)\right]\cdot \\ &\left(\frac{1}{\lambda_M^{(3)}}\right) E_1 \end{aligned} \tag{B.0.49}$$

We can see that in the matching case the free wave which is matched becomes a linearly growing wave. In addition there is a non-growing wave with its electric field perpendicular to that of the free wave. The non-growing component is a slowly varying function of $\vec{s}_k$, but the growing wave is rapidly varying and the form found here is only valid for exact matching $\vec{s}_k = \vec{s}_M$.

The preceding formulation is deficient in the respect that it provides no convenient means for treating nearly matching cases. A laser beam has a finite angular spread, so all of the beam can never satisfy the matching condition exactly. A proper formulation requires that a wave be found which satisfies B.0.37 and reduces to B.0.44 in the limit as $n^{'}$, $\vec{s}_k$ approaches a matching condition. We imagine that $n^{'}$ is a function of $\vec{s}_k$, so that an *effective-index surface* can be constructed for the polarization waves. The simplest case is to consider SHG in which $\vec{P}(\vec{r},t)$ arises from a single plane wave from the laser in the direction $\vec{s}_k$. Then $n^{'}$ is a refractive index for $\vec{s}_k$ at the fundamental frequency $\frac{\omega}{2}$, and the effective-index surface is just one sheet of the index surface of the medium at frequency $\frac{\omega}{2}$. The matching directions which shall be denoted by $\vec{s}_M$ are determined by the intersection of the index surface and the effective-index surface

$$n^{'}(\vec{s}_M) = n(\vec{s}_M) \equiv n_M \tag{B.0.50}$$

As the matching condition is approached, $\vec{s}_k \to \vec{s}_M$ and also $\vec{s} \to \vec{s}_M$. It is clear that $n, \vec{s}$ must be added to equation B.0.38 in such a way that the singularity in $\vec{E}^{'}$ as $\lambda_k^{(1)} \to 0$ is removed. From equation B.0.39 and B.0.43 we find that the desired form is

$$\begin{aligned} \vec{E}_k(\vec{r}) &= \alpha_k^{-1}\cdot 4\pi\vec{P}e^{i\left(\frac{\omega}{c}\right)n^{'}\vec{s}_k\cdot\vec{r}} \\ &- \left(\frac{1}{\lambda_k^{(1)}}\right)\vec{U}_s^{(1)}\vec{U}_k^{(1)}\cdot 4\pi\vec{P}e^{i\left(\frac{\omega}{c}\right)n\vec{s}_k\cdot\vec{r}} \end{aligned} \tag{B.0.51}$$

From $n^{'}\vec{s}_k - n\vec{s} = \varphi\vec{N}$ (φ is a scalar function of $\vec{s}_k$, measuring how far $\vec{s}_k$ is from matching conditions) and equation B.0.43, this can be written

$$\begin{aligned}\vec{E}_k(\vec{r}) &= \left\{\sum_{j=2,3}\left(\frac{1}{\lambda_k^{(j)}}\right)\vec{U}_k^{(j)}\vec{U}_k^{(j)}\cdot 4\pi\vec{P}\right. \\ &\quad \left.+\left(\frac{1}{\lambda_k^{(1)}}\right)\left(\vec{U}_k^{(1)}-\vec{U}_s^{(1)}e^{-i\left(\frac{\omega}{c}\right)\varphi\vec{N}\cdot\vec{r}}\right)\vec{U}_k^{(1)}\cdot 4\pi\vec{P}\right\} \\ &\quad \times e^{i\left(\frac{\omega}{c}\right)n^{'}\vec{s}_k\cdot\vec{r}} \qquad \text{(B.0.52)}\end{aligned}$$

where the second term in brackets is seen to be finite as $\lambda_k^{(1)} \to 0$, $\varphi \to 0$, $\vec{U}_k^{(1)} \to \vec{U}_s^{(1)}$. Clearly the first term in B.0.52 is identical with the first term in B.0.48 representing the non-growing wave due to components of $\vec{P}$ which cannot produce a growing wave in matching limit. It can be shown that equation B.0.52 reduces indeed to equation B.0.44. It should also be noted that equation B.0.52 is exact. Let's introduce approximations appropriate to the nearly matching case. The second term of B.0.52 can be written in the form, leaving off the exponential factor,

$$\left(\frac{1}{\lambda_k^{(1)}}\right)\left[\left(\vec{U}_k^{(1)}-\vec{U}_s^{(1)}\right)+\vec{U}_s^{(1)}i\left(\frac{\omega}{c}\right)\varphi\vec{N}\cdot\vec{r}g\left(i\omega\varphi\vec{N}\cdot\frac{\vec{r}}{c}\right)\right]\cdot\left(\vec{U}_k^{(1)}\cdot 4\pi\vec{P}\right) \qquad \text{(B.0.53)}$$

where g is the function

$$g(z) = \frac{(1-e^{-z})}{z} \qquad \text{(B.0.54)}$$

If we now go to the matching limit $\vec{s}_k \to \vec{s}_M$ but retain g, we obtain

$$\vec{E}_k(\vec{r}) = \vec{E}_1\left(\vec{N}\cdot\vec{r}\right)g(2i\psi)\,e^{i\left(\frac{\omega}{c}\right)n_M\vec{s}_M\cdot\vec{r}} + \vec{E}_{2,3}e^{i\left(\frac{\omega}{c}\right)n_M\vec{s}_M\cdot\vec{r}} \qquad \text{(B.0.55)}$$

where $\vec{E}_1$, $\vec{E}_{2,3}$ are defined in equations B.0.45, B.0.47 and B.0.48, and

$$\psi = \left(\frac{\omega}{2c}\right)\varphi\vec{N}\cdot\vec{r} \qquad \text{(B.0.56)}$$

All the essential effects of small deviations from the matching condition are contained in $g(2i\psi)$. The linearly growing amplitude of the E_1 wave in the matching limit is due to interference between the wave $n^{'}$, $\vec{s}_k$ and the free wave n, $\vec{s}$. The distance over which this interference is effective is determined by φ defined by $n^{'}\vec{s}_k - n\vec{s} = \varphi\vec{N}$. The *coherence length for the wave* l_{coh} may be defined in terms of φ as follows: Let $g(2i\psi)$ vanish for $\vec{r} = \vec{s}l_{coh}$; then

$$l_{coh} = \left|\frac{2\pi c}{\omega\varphi}\right|\left(\vec{N}\cdot\vec{s}\right)^{-1} \qquad \text{(B.0.57)}$$

This definition is equivalent to that given in equation B.0.35.

Consider the index surface and the effective-index surface in the region of their intersection. It is assumed that such an intersection exists and that the polarization $\vec{P}(\vec{r},t)$ is a narrow pencil of waves $n^{'}$, $\vec{s}_k$ which includes part of the intersection. Let unit normal vectors be constructed to the two surfaces, $\vec{N}_s$ for the index surface and $\vec{N}_k$ for the effective-index surface. Then the vector $\vec{N}_k \times \vec{N}_s$ lies along the intersection, which, if the pencil is narrow, may be considered a straight line. Furthermore, let

$$\vec{\delta} = \vec{s}_k - \vec{s}_0\ , \quad |\delta| \ll 1 \qquad \text{(B.0.58)}$$

where $\vec{s}_0$ is the central wave of the pencil, and let $\vec{s}_0$ be a matching direction $\vec{s}_M$. Then it can be shown that φ may be written

(B.0.59)
$$\varphi = n_0 \left(\vec{N}\cdot\vec{N}_s\right)^{-1}\left(\vec{s}_0\cdot\vec{N}_k\right)^{-1}\times\left[\left(\vec{s}_0\cdot\vec{N}_k\right)\left(\vec{\delta}\cdot\vec{N}_s\right)-\left(\vec{s}_0\cdot\vec{N}_s\right)\left(\vec{\delta}\cdot\vec{N}_k\right)\right]$$

where n_0 is the matching index at $\vec{s}_0$. It is evident that φ given by B.0.59 vanishes when $\vec{\delta}$ lies along $\vec{N}_k\times\vec{N}_s$. Clearly $\vec{\delta}$ is perpendicular to $\vec{s}_0$ and therefore may be expressed in terms of a pair of polar coordinates. Let $\delta = \left|\vec{\delta}\right|$and let θ be the angle $\vec{\delta}$ makes with the matching line $\vec{N}_k\times\vec{N}_s$ projected onto a plane normal to $\vec{s}_0$. Then it can be shown that φ is given by

$$\varphi = n_0\left(\vec{N}\cdot\vec{N}_s\right)^{-1}\left(1-2R\vec{N}_k\cdot\vec{N}_s+R^2\right)^{\frac{1}{2}}\delta\sin\theta \tag{B.0.60}$$

where

$$R=\frac{\left(\vec{s}_0\cdot\vec{N}_s\right)}{\left(\vec{s}_0\cdot\vec{N}_k\right)} \tag{B.0.61}$$

If $\vec{N}_s$, $\vec{N}_k$, $\vec{s}_0$ lie in the same plane, as in uniaxial crystals,

$$\left(1-2R\vec{N}_k\cdot\vec{N}_s+R^2\right)^{\frac{1}{2}}=\left(\vec{s}_0\cdot\vec{N}_k\right)^{-1}\sin\rho \tag{B.0.62}$$

where ρ is the angle between $\vec{N}_k$ and $\vec{N}_s$. In many cases $\vec{N}_k$ and $\vec{N}_s$ will be very nearly in the direction $\vec{s}_0$, and we can write

$$\begin{aligned}\vec{N}_s &= \left(1-\delta_s^2\right)^{\frac{1}{2}}\vec{s}_0+\vec{\delta}_s,\quad \vec{s}_0\cdot\vec{\delta}_s=0\\ \vec{N}_k &= \left(1-\delta_k^2\right)^{\frac{1}{2}}\vec{s}_0+\vec{\delta}_k,\quad \vec{s}_0\cdot\vec{\delta}_k=0\\ &\left|\delta_s\right|^2\ll 1,\quad \left|\delta_k\right|^2\ll 1\end{aligned} \tag{B.0.63}$$

Then we have

$$\left(1-2R\vec{N}_k\cdot\vec{N}_s+R^2\right)^{\frac{1}{2}}=\left|\vec{\delta}_k-\vec{\delta}_s\right| \tag{B.0.64}$$

We consider the energy flow in the wave B.0.55 with the aid of two reasonable assumptions which greatly simplify the discussion. We assume that the conditions are very close to matching, so that $\varphi\ll n_M$ and $l_{coh}\gg\lambda_M=\left(\frac{2\pi c}{n_M\omega}\right)$. Then the $\vec{E}_1$ wave can be very large compared to the $\vec{E}_{2,3}$ wave; except near the zeros of $g\left(2i\psi\right)$we have

$$E_1 lg\gg E_2, E_3$$

where $l=\vec{N}\cdot\vec{r}$. The second assumption is that the medium is not exceptionally anisotropic. The treatment up to this point has been completely general in regard to anisotropy. It is well known that in an anisotropic medium the flow of energy is not in general along $\vec{s}$. The component of the time average Poynting vector along $\vec{s}$ is

$$S=\left(\frac{nc}{8\pi}\right)\left|E_t\right|^2 \tag{B.0.65}$$

where E_t is the transverse component of the amplitude of the electric field. Since the anisotropies of most crystals are quite small, of the order of a few percent, we shall assume that $\vec{E}_1$ is nearly transverse, and that S in B.0.65 is essentially the total energy flow. Thus we write

$$S=\left(\frac{nc}{8\pi}\right)\left|E_1\right|^2 l^2\left|g\left(2i\psi\right)\right|^2 \tag{B.0.66}$$

From equation B.0.54 it follows that

$$|g\,(2i\psi)|^2 = \frac{\left(\sin^2\psi\right)}{\psi^2} \tag{B.0.67}$$

It is clear that S varies over the narrow pencil of waves comprising the laser beam. An individual wave in this pencil is described by the coordinates δ, θ in terms of which ψ may be calculated from equations B.0.56 and B.0.60. Thus S may be averaged over the pencil to give the mean Poynting vector

$$\langle S\rangle = \left(\frac{n_0 c}{8\pi}\right)|E_1|^2\, l^2 \left\langle \frac{\left(\sin^2\psi\right)}{\psi^2} \right\rangle \tag{B.0.68}$$

The total SHG is the area of the laser beam multiplied by $\langle S\rangle$. This includes all the contributions due to mixing of slightly divergent waves in the pencil.

We may define the average B.0.68 as a function

$$F\,(\beta l \Delta) = \left\langle \frac{\left(\sin^2\psi\right)}{\psi^2} \right\rangle \tag{B.0.69}$$

where Δ is a measure of the spread of the beam, and from B.0.60 and B.0.56

$$\beta = n_0 \left(\frac{\omega}{2c}\right)\left(\vec{N}\cdot\vec{N}_s\right)^{-1}\left(1 - 2R\vec{N}_k\cdot\vec{N}_s + R^2\right)^{\frac{1}{2}} \tag{B.0.70}$$

The form of F will depend upon the distribution of directions δ, θ in the beam. The simplest assumption is that the distribution is independent of θ and constant for δ in the range $0 \le \delta \le \Delta$ and vanishes for $\delta > \Delta$. It is convenient to define a *coherence length for the pencil*

$$l'_{coh} = \frac{2}{\beta\Delta} \tag{B.0.71}$$

This should not be confused with l_{coh} in B.0.57, the coherence length for the wave. The pencil contains many waves with widely varying l_{coh}; l'_{coh} is a suitable average over the distribution of l_{coh} in the pencil.

APPENDIX C

Plasma Physics

According to the theory of plasma physics [**5, 26**] the absorption coefficient α_p of a plasma for electro-magnetic radiation is given by

$$\alpha_p = \frac{\omega_p^2}{\omega^2} nct_0 \tag{C.0.72}$$

with ω_p = the plasma frequency, ω = frequency of the laser radiation, n = refractive index, c = speed of light and t_0 = mean electron-ion collision time. The plasma frequency is defined by

$$\omega_p = \sqrt{\frac{N_e e^2}{m\epsilon_0}} \tag{C.0.73}$$

with N_e = free electron density, e = electron charge, m = electron mass and ϵ_0 = dielectric constant. The mean free path of an electron is given by

$$\lambda = vt_0 = \frac{1}{N_e \sigma} \tag{C.0.74}$$

with v = average speed of a plasma electron and σ = cross section of a collision. Hence

$$t_0 \sim \frac{1}{N_e} \tag{C.0.75}$$

Using equations C.0.73 and C.0.75 in equation C.0.72 one obtains

$$\alpha_p \sim N_e^2 \sim E^2 \tag{C.0.76}$$

with E = energy of the radiation, since on the average the same amount of energy (same number of photons) will be absorbed by each electron that is dissociated when assuming a multiphoton process. The absorption of the incident radiation is governed by Lambert-Beer's law, which is

$$\frac{\delta E}{\delta z} = -\alpha_p E\,(z) \tag{C.0.77}$$

where z is depth into the tissue. Combining equations C.0.76 and C.0.77 yields the new relation

$$\frac{\delta E}{\delta z} \sim E^3\,(z) \tag{C.0.78}$$

A pressure, p, is generated given by the absorbed energy per unit volume, which is

$$p = -\frac{\delta E}{\delta V} = -\frac{1}{4}\pi z^2 \frac{\delta E}{\delta z} \sim \frac{E^3}{z^2} \tag{C.0.79}$$

Ablation takes place until a certain minimum pressure p_0 is reached. This threshold is given by

$$\frac{E^3}{d^2} = p_0 = \text{const.} \tag{C.0.80}$$

where d is the ablation depth. Hence

$$d \sim E^{1.5} \tag{C.0.81}$$

This relationship is in very good agreement with the experimental results from Niemz et al. [**45**] and with other experiments performed by Stern et al. [**56**].

APPENDIX D

Recipes for PBS, PFA and Glutaraldehyde

The following values are calculated for $1000\,ml$ $100\,mM$ **phosphate buffered saline solution.**

$10.647\,g$ di-Sodiumhydrogenphosphate (molecular weight: $141.96\,u$) and $3.402\,g$ Potassium-di-hydrogenphosphate (molecular weight: $136.09\,u$) are dissolved in about $800\,ml$ distilled water. Then the pH value is determined and if need be adjusted to a pH value between 7.2 and 7.4. This solution is then filled to $1000\,ml$ with distilled water.

The following values are calculated for $1000\,ml$ **4% para-Formaldehyde solution in PBS.**

$40\,g$ para-Formaldehyde are given to about $950\,ml$ PBS. To get the para-Formaldehyde solved the solution has to be heated carefully to $59°C$ under constant stirring. (The fumes are hazardous so use the fume hood; do not heat higher than $59°C$ or decomposition occurs) Some added drops of concentrated Sodiumhydroxyde solution will clear the solution. After cooling down to room temperature the pH value has to be readjusted to 7.4 by using $0.1\,M$ Hydrochloric acid or $0.1\,M$ Sodiumhydroxyde solution. The so obtained solution has to be filled to $1000\,ml$ with PBS.

The following values are calculated for $100\,ml$ **5% Glutaraldehyde solution in PBS.**

$20\,ml$ Glutardialdehyde solution (25%) are mixed with $80\,ml$ PBS.

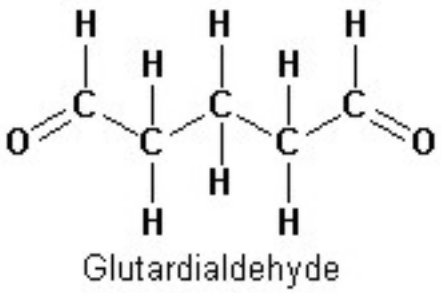

Figure D.0.2. Chemical structure of glutardialdehyde

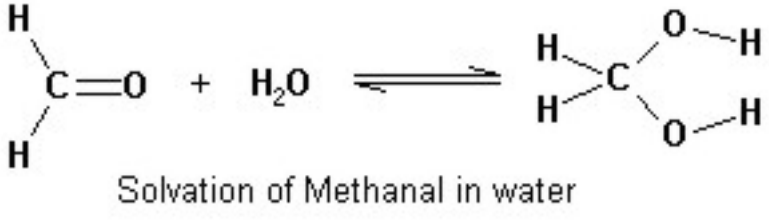

Figure D.0.1. Chemical structure of formaldehyde

Acknowledgement

My thanks go to Prof. Dr. J. Bille for the interesting theme of this work. I also want to thank him for his help during the work by having time for my problems. I want to thank Dr. Meng Han for his help during the experimental phase and his ideas concerning the layout of the work. Mr. Leander Zickler I have to thank for his critics at some phases of the experiments and his data concerning the LSM. I also want to thank A. Schweizer who helped me correcting some of my typing errors and gave me tips for the layout. And I thank all of the people of the Kirchhoff Institute who helped with their knoweldge and who gave me the feeling that I was one of them.

My thanks go also to Dr. G. Giese and Prof. Dr. W. Denk from the Max - Planck - Institute of medical research in Heidelberg for the possibility to use their microscopic facilities and their invaluable help with the Zeiss LSM. And also many thanks go to Mr. H. Horstmann for his help in providing the cornea cryoslices.

I also thank the people of 2010 Perfect Vision for the possibility to use their laser for the treatment of the eyes.

Dr. D. Neff of Veeco metrology system I thank for his introduction into the technics concerning the AFM.

And last but not least I thank Prof. Dr. G. Cox from the University of Sydney and Dr. E. Lesniewska from the University of Bourgogne for their help in obtaining information about respectivly the usage of second harmonics in imaging collagen and the usage of the AFM for imaging the cornea after laser treatment.